Anisotropic and non-linear optical properties of self-assembled colloidal metasurfaces

Dissertation

zur Erlangung des akademischen Grades eines

Doctor rerum naturalium

(Dr. rer. nat.)

vorgelegt dem Bereich Mathematik und Naturwissenschaften

der Technischen Universität Dresden

TECHNISCHE UNIVERSITÄT DRESDEN

Von

M.Sc. Olha Aftenieva

Geboren am 17.01.1996 in Odesa, Ukraine

Eingereicht am:	22.06.2022
Verteidigt am:	19.07.2022
Gutachter:	PD Dr. Tobias A. F. König
	Prof. Dr. Alexander Eychmüller

Angefertigt von November 2018 bis Juni 2022 unter der Betreuung von PD Dr. Tobias A. F. König am Leibniz-Institut für Polymerforschung Dresden e.V.

Contents

Abstract

Photonic metasurfaces obtain their unique optical properties from the periodic arrangement of sub-wavelength building blocks and can manipulate light in ways that differ significantly from bulk materials. Until recently, metasurfaces have been fabricated using top-down methods on a limited surface area. With the development of directed self-assembly methods and utilization of nanoscale colloids, metasurfaces can be fabricated on a larger scale and with reasonable efforts. In particular, soft nanoimprint lithography, based on the controlled drying of the colloidal solution within a structured template, allows for the precise placement of versatile colloidal building blocks on a substrate of choice. In this dissertation, the material and optical properties of self-assembled plasmonic and photoluminescent nanoparticles are systematically studied in terms of their short- and long-range interactions. It is shown that 1D plasmonic lattices exploit the intrinsic anisotropy and substrate-dependent collective resonant coupling. Likewise, semiconductor nanoparticles organized into linear gratings, result in light-emitting metasurfaces, featuring geometry-dependent amplification of the photoluminescence that can be further promoted to a non-linear amplification regime. Moreover, on flexible substrates, these self-assembled light-emitting metasurfaces can be stacked and twisted, inducing remarkably strong chiral effects and subsequently used for directional light sources, nanolasers, sensing, and labeling applications. Supported by theoretical modeling, this work provides a novel approach to realize anisotropic and non-linear optical properties on centimeter-scaled surface area using soft-lithography and directed self-assembly methods. It bridges the gap between nanoscale colloids and optoelectronics while advancing the integration of metasurfaces into functional devices.

Kurzfassung

Photonische Metaoberflächen erhalten ihre einzigartigen optischen Eigenschaften durch die periodische Anordnung von Bauelementen im Sub-Wellenlängenbereich und können Licht auf eine Weise manipulieren, die sich deutlich von Ausgangsmaterialien unterscheidet. Bis vor kurzem wurden Metaoberflächen mit Top-Down-Methoden auf einer begrenzten Oberfläche hergestellt. Mit der Entwicklung von Methoden der gerichteten Selbstorganisation und der Nutzung von Kolloiden im Nanomaßstab können Metaoberflächen in größerem Maßstab und mit angemessenem Aufwand hergestellt werden. Insbesondere die Soft-Nanoimprint-Lithographie, die auf der kontrollierten Trocknung der kolloidalen Lösung innerhalb einer strukturierten Template basiert, ermöglicht die präzise Platzierung vielseitiger kolloidaler Bauelemente auf einem Substrat der Wahl. In dieser Dissertation werden die materiellen und optischen Eigenschaften selbstorganisierter plasmonischer und photolumineszenter Nanopartikel im Hinblick auf ihre Kurz- und Langstreckenwechselwirkungen systematisch untersucht. Es wird gezeigt, dass plasmonische 1D-Gitter die intrinsische Anisotropie und die substratabhängige kollektive Resonanzkopplung ausnutzen. Ebenso führen Halbleiter-Nanopartikel, die in linearen Gittern organisiert sind, zu lichtemittierenden Metaoberflächen, welche eine geometrieabhängige Verstärkung der Photolumineszenz aufweisen, die bis zu einem nichtlinearen Verstärkungsregime weitergeführt werden kann. Außerdem können diese selbstorganisierten, lichtemittierenden Metaoberflächen auf flexiblen Substraten gestapelt und verdreht werden, was zu bemerkenswert starken chiralen Effekten führt und anschließend für gerichtete Lichtquellen, Nanolaser, Sensor- und Beschriftungsanwendungen genutzt werden kann. Unterstützt durch theoretische Modellierung bietet diese Arbeit einen neuartigen Ansatz zur Realisierung anisotroper und nichtlinearer optischer Eigenschaften auf zentimetergroßen Oberflächen unter Verwendung von Softlithographie und Methoden der gerichteten Selbstmontage. Sie überbrückt die Lücke zwischen Kolloiden im Nanomaßstab und der Optoelektronik und treibt gleichzeitig die Integration von Metaoberflächen in funktionale Geräte voran.

List of Abbreviations

1D – one-dimensional

2.5D – two-and-half-dimensional

2D – two-dimensional

ACS – American Chemical Society

AFM – atomic force microscopy

AgInS/ZnS – silver indium sulfide and zinc sulfide

ASE – amplified spontaneous emission

AuNP – gold nanoparticle

CAPA – capillary-assisted self-assembly

CD – circular dichroism

CdSe/ZnCdS – cadmium selenide and zinc cadmium sulfide

CFM – confocal fluorescence microscopy

CMF – color matching functions

$CsPbI_3$ – cesium lead triiodide

cw – constant wave

DFB – distributed feedback

DNA – deoxyribonucleic acid

EBL – electron-beam lithography

FDTD – finite-difference time-domain

FIB – focused ion beam

FWHM – full width of half-maximum

GMR – guided mode resonance

IRF – instrument response function

LbL – layer-by-layer

LCP – left circularly polarized

LED – light emitting diode

LIL – laser interference lithography

LSPR – localized surface plasmon resonance

MSE – mean square error

NA – numerical aperture

NIL – nanoimprint lithography

NP – nanoparticle

NPL – nanoplatelet

OA – oleic acid

OLA – oleylamine

PDMS – polydimethylsiloxane

PEG – polyethylene glycol

PL – photoluminescence

PLQY – photoluminescence quantum yield

PMMA – polymethyl methacrylate

Q – quality (factor)

QD – quantum dot

QWP – quarter waveplate

RA – Rayleigh anomaly

RCP – right circularly polarized

RGB – red, green and blue (color coding)

RMS – root mean square

SEM – scanning electron microscopy

SiO_2 – silicone dioxide

SLR – surface lattice resonance

TASA – template-assisted self-assembly

TE/TM – transverse electric and transverse magnetic (wave)

TEM – transmission electron microscopy

TGA – thioglycolic acid

TiO_2 – Titanium dioxide

UV – ultraviolet (light)

In this dissertation, the acronyms are introduced at first mention in each of the Chapters 1–6 for clarity.

1. Introduction

1.1. Optical properties of single nanoscale objects

Until now, a great variety of nano-objects was manufactured, studied, and exploited for numerous applications in industrial and biomedical applications and basic scientific research.[1–3] The key feature of such abundance is the unique physicochemical properties of the nanoscale objects, originating from the electronic structure of the material.[1,4] Let us first consider the case of metal nanoparticles (NPs) in more detail. The free electrons of the conduction band in metal experience collective oscillations upon the external electromagnetic excitation. Those oscillations are confined to the surface of the NP and, accordingly, are termed localized surface plasmon resonance (LSPR).[5,6] Due to LSPR, the scattering and absorption that when added up constitute extinction behavior of NPs differs from the one in bulk metals, which is reflected in their perceived color.[7] For instance, medium-sized gold nanoparticles (AuNPs) of a few tens of nanometers, dispersed in water, appear ruby red, when the observer looks through the flask with colloidal solution, scattering a 'green' portion of the incident spectrum, and absorbing in the 'blue-green' region.[8] Such an intuitive perception, together with a relative easiness of the synthetic approach, arguably made AuNPs a standard model for the development of educational material for students in nanoscience.[9] Besides, the recent advances in chemical synthesis[10] allowed not only for the creation of nearly ideal, monocrystalline spheres,[11–14] but also exploring composite configurations[15,16] and asymmetric shapes[17–19] with anisotropic optical properties, revealed in polarization-dependent scattering and absorption of light.

By considering semiconductor materials and diminishing the size of NPs down to a few nanometers in all principle dimensions, the concept of colloids can be extended to the so-called quantum dots (QDs). The term is linked to the quantum confinement effects that arise upon size-reduction[20] and alter the electronic structure, shifting and quantizing the energies of the conduction and valence bands of a semiconductor.[21–23] The bound electronic states can then be compared to the highest occupied and lowest unoccupied molecular orbitals.[24] When the electron is promoted to an excited state, it leaves a 'hole' and, as a result, a bound electron-hole pair or exciton is created. Thus, the separation between the energy levels of the excited and ground states of a QD constitutes the bandgap, inherently present in bulk semiconductors, and size-

dependent exciton confinement and electrostatic energies. After the exciton recombination (spontaneous or stimulated), the corresponding energy is released in the form of emission of photons and the number of emitted photons per number of absorbed photons represents the photoluminescence (PL) quantum yield (PLQY).[25] In such a way, by combining various semiconductor materials, creating core-shell structures, and varying the shape and size of nanocrystals, one can precisely tune the absorption and emission properties of QDs.[1,26] The manufacturing processes range from substrate-dependent lithography and epitaxial growth to colloidal chemistry.[27] The wet chemical synthesis allowed for tailoring the surface chemistry and obtaining morphologically uniform free-standing QDs in a colloidal solution and made them accessible for industrial applications.[3,28,29] In principle, QDs can be produced from any semiconductor, however, cadmium (Cd)-based QDs appear as the most robust colloidal gain material, featuring well-established synthesis routes, and, therefore, presenting themselves as an ideal test system for device manufacturing.[30,31] More recently, the range of compound materials was extended to noble metal, transition, and post-transition metal alloys,[32,33] or lead (Pb)-based perovskites, featuring remarkably high PLQY.[34] The latter is generally important for the light-emitting diodes (LEDs) and optically pumped lasers, where the initial strong luminescence in solution has to be still maintained within dried crystalline films, where the energy transfer between the neighboring QDs takes place.[35] For device applications, the photostability of QDs also plays a decisive role. Besides the inherent instability due to the size, shape, and material composition,[36,37] prolonged exposure to the harsh oxidative environment or light irradiation may be detrimental to the internal crystalline structure of QDs.[38] To provide efficient isolation of individual QDs, the core-shell configuration can be implemented,[39] whereas inorganic composition ensures the thermal stability during the charge injection or processing, superior to the organic light-emitting materials.[40] Additionally, the external encapsulation of the QDs, readily integrated into a device, offers prolonged stability in the ambient conditions.[41,42]

1.2. Collective anisotropic and non-linear optical behavior

The optical properties of nano-objects directly depend on their surrounding.[43] Thus, when NPs of any kind are brought into the vicinity of each other or arranged into certain patterns, their optical responses change accordingly.[44] The collective emerging

effects include dramatic color changes,[45,46] strong local electromagnetic field enhancement in between the particles[47] or mode hybridization.[48] Such arrangements of NPs into ordered arrays that control the propagation of light in ways that are otherwise unattainable with natural materials are known as colloidal metasurfaces.[49,50] Using colloids brings up the advantage of integrating monodisperse and easily tunable building blocks into scalable and low-cost manufacturing processes,[51] and, by controlling the short- and long-range coupling behavior, inducing novel optical effects that go beyond the conventional performance of single NPs. The coupling strength has a near-exponential dependence on the separation between the nanoscale objects, being related via the near-field decay as the inverse of the distance to the power of three and the interparticle restoring potential, proportional to the particle volume.[52] In a dense packing of metal NPs, individual plasmonic modes hybridize similarly to the energy states in the molecular orbital theory, resulting in significant spectral shifts and splitting of the LSPR peaks.[48,53–55] When the distance between the particles becomes larger than their diameter, the LSPRs can couple through scattered radiation fields.[56,57] In a periodic arrangement, where the distance between the unit cells is comparable to the wavelength of the incident light, the LSPRs can interact with the so-called Rayleigh anomalies (RAs) - photonic modes that originate from the periodic arrangement itself, when the Bragg condition is satisfied and a diffracted wave arises and propagates tangentially to the surface of the grating.[58] Such coupled modes are termed surface lattice resonances (SLRs).[59–61] In contrast to the LSPRs that suffer from the radiative damping and, therefore, feature rather broad bandwidths and low-quality factors,[62] SLRs demonstrate significantly narrower peaks.[63,64] This can be attributed to a Fano interference of discrete RAs with the continuum of a broadband LSPR.[65] Since the 'photonic' part of SLR is defined by the geometry of the arrangement, a strong anisotropy towards the polarization and angle of incidence of the excitation wavevector $k_0 = {}^w/_c$ is observed (here w is incident wave frequency and c denotes the speed of light). This can be best illustrated through the dispersion diagrams, featuring the wavelength-dependency of SLR. Such diagrams can be obtained by plotting the extinction (or transmission) as a function of the angle of incidence θ (or the in-plane component of the incident wavevector $k_\parallel = k_0 \sin\theta$) and photon wavelength (or energy).[44] The geometry of the grating defines the appearance of SLRs on the dispersion diagrams and was already explored within 1D grating lines,[58] 2D square and rectangular lattices,[66] as well as hexagonal and Moiré arrangements.[67–69] The simple periodic 1D gratings are, however, of particular interest

since they readily provide polarization-related anisotropy owing to the lower symmetry of the lattice and offer an opportunity for generating a chiral optical response. Simple stacking and twisting of two layers of planar metasurfaces with the subwavelength distances in between, induced bianisotropic absorption of circularly polarized light that was utilized for broadband circular polarizers[70,71] and as highly sensitive biosensors for chiral molecules.[72]

Furthermore, the concept of SLR can be extended to hybrid metasurfaces, where several photonic and plasmonic resonant features are interacting. For instance, by incorporating thin-film layers, guided mode resonant (GMR) modes can be coupled with the LSPR or SLR modes. The GMR itself occurs, when two photonic components are combined, namely, a diffraction grating and a slab waveguide.[73] A thin film with a high refractive index, surrounded by a lower refractive index environment, represents a typical slab waveguide structure, where the electromagnetic wave can propagate along its longitudinal direction, representing the guided mode with a characteristic effective refractive index n_{eff}.[74] When the propagating angle of the guided mode matches the diffraction angle at a certain wavelength, it can be then outcoupled through the periodic gratings to the far-field.[75] The hybridization of such photonic features with plasmonic resonances also features Fano-type interaction and, has already been successfully demonstrated for various applications, such as strong coupling,[76] fluorescence enhancement[77,78] and optical filtering.[79] The manufacturing process of such metasurfaces with hybrid modes relied mostly on top-down lithography methods that are difficult to realize on a large scale in a cost-efficient way. On the other hand, such metasurfaces, fabricated with the colloidal approach, have not yet fully revealed their potential in terms of realization and possible applications.[73]

Similar to the periodic arrangements of plasmonic metal NPs, the PL from semiconductor QDs can interact with the diffractive modes. This interaction becomes increasingly important in the light of the recent technological developments: thin films of QDs were already used in displays[80,81] and light-emitting diodes (LEDs).[82–84] Even though now the PLQY of various colloidal QDs reach remarkably high values,[85,86] the output luminescence from QDs, closely packed in a thin film, decreases significantly. Due to the elemental composition of QDs, such layers have high refractive indexes and the emitted light stays trapped within the film.[87] One of the solutions includes individual overcoating or collective embedding of QDs into stable oxide phases.[88] Another approach that does not require the complication of the chemical synthesis

procedure and allows for using all variety of the QDs available, implies the presence of a light-outcoupler, such as an optical wire,[89] photonic crystal,[90,91] or through structuring the QD-based thin films directly into the so-called distributed feedback (DFB) configurations that support GMRs.[87] A representative effect of a light-outcoupler is illustrated in a Figure 1 below.
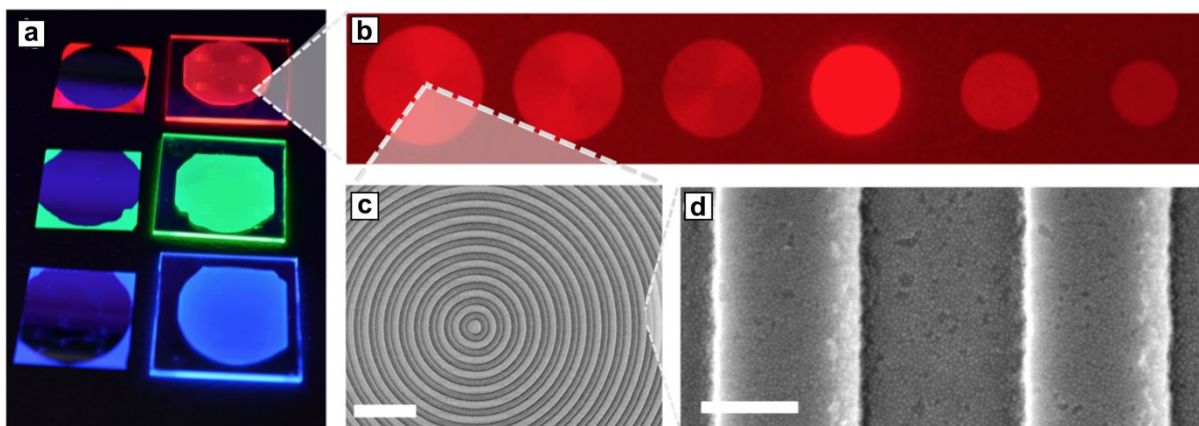

Figure 1: (a) Photograph of ultraviolet (UV)-illuminated patterned films of red, green, and blue-emitting QDs. (b) Fluorescence microscopy image of an array of bull's-eye gratings of 300 concentric circles each on a red-emitting QD-based film. The periodicity of these gratings p varied from 550 to 300 nm with 50 nm decrements. (c,d) scanning electron microscopy (SEM) micrographs at different magnifications of a concentric grating with 550 nm periodicity. Scale bars are 2 μm and 200 nm, respectively. Reprinted and adapted with permission from *Nano Lett.* 2017, 17, 3, 1319–1325. Copyright 2017 American Chemical Society. Further permissions related to the material excerpted should be directed to the ACS.

Here, the DFB configuration featured an isotropic concentric grating, residing on a waveguide-like thin film, comprised solely of highly luminescent QDs (Figure 1d). The 1st diffraction order efficiently scattered the guided light in the direction, normal to the surface of the grating, only when the emission wavelength λ_{em} satisfied the condition: $\lambda_{em} = p \cdot n_{eff}$, where p is the periodicity of the grating and n_{eff} denotes the effective refractive index of the guided modes. In this case, a distinctive amplification of PL from the center of the structure was observed (Figure 1b).

Furthermore, promoting the light amplification and controlling the direction of the out-coupled PL, under certain conditions leads to non-linear effects, i.e. lasing.[92] In this regard, it is important to differentiate between spontaneous emission, which takes place without interaction with an external radiation field, so that the direction of the emitted photons and phase are random, and stimulated emission, where the electrons in the excited state transit to the ground state under the influence of the external photons, preserving their direction, phase, and energy. The amplification rate is the highest when the frequency of the external field matches the resonance of the active

medium.[93] Then, the population of the ground and excited states must be inverted, so that the stimulated emission becomes the dominant process and the energy, provided to the active medium, is transformed into a highly directional and coherent light.[94] The lasing itself has a characteristic behavior expressed via the clear threshold in both the output power and bandwidth of the emitted light.[95] The key to an efficient lasing system lies in the careful design of the geometry of the feedback system,[96] which can be performed via the numerical simulations, and the choice of the optical gain.[97] In this regard, inorganic semiconductor QDs surpass the organic medium, offering delocalized excited states and avoiding long-living triplets that are often the cause of the suppressed emission in organic lasers.[98,99] Moreover, Cd-based QDs in particular demonstrate enhanced thermal stability, guaranteeing the long-term QD integrity needed to achieve the population inversion that is usually accompanied by pumping at a very high power level and, therefore, excessive local heat.[100]

1.3. Colloidal approach for nanoparticle arrays

The imminent advantage of colloidal assembly lies in the parallel placement of particles that in contrast to EBL can be realized cost-efficiently and over large areas.[101] Generally, colloidal NPs can be arranged into ordered structures via conventional and directed self-assembly.[102] The first method implies spontaneous or triggered by external stimuli agglomeration of NPs through molecular recognition and association,[103] allowing for highly specific and controllable assembly. One of the most robust systems is offered by DNA hybridization, where the end-to-end or side-to-side interactions can be pre-designed by adjusting the nucleic acid sequences of the corresponding parts.[104] Nevertheless, such a technique is very susceptible to the environmental conditions of the system (pH, temperature, etc.), which limits its robustness.

An alternative to conventional self-organization is realized through directing the NPs by external stimuli: the entropy reduction at the interface, electromagnetic or hydrodynamic fields, or with a help of a structured template.[102,105] The directed assembly on the air-liquid interface, also termed as Langmuir-Blodgett technique, relies on the ability of mobile colloidal NPs to adsorb to the interface boundaries and arrange into structures with minimal free energy.[106] This technique was already applied for the assembly of metal NPs into hexagonal and 2D lattices and, by overlaying, into the Moiré arrangements:[67–69,107] as well as for the semiconductor

nanocrystals,[108–110] which is demonstrated in Figure 2 below. In this particular example, nanocrystals, capped with an appropriate ligand that prevents the aggregation within a colloidal solution and controls the interparticle distances in a close packing of a dried-state, were assembled on a sub-phase of an organic solvent. The drop-casting of the silicon oil caused the compression of the nanocrystals at the interface into a crystalline film that was then transferred to a solid substrate by draining the solvent.
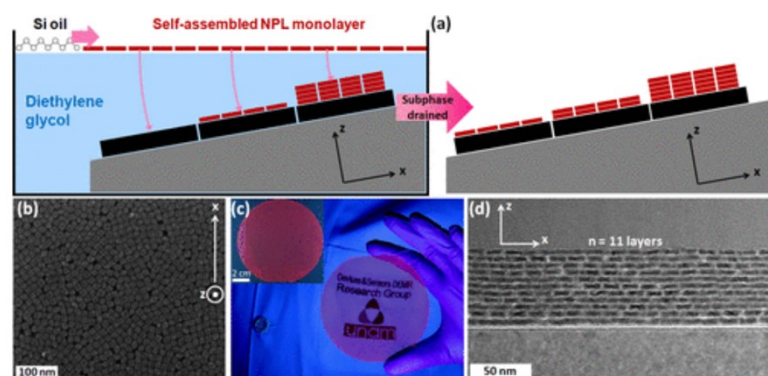

Figure 2: (a) Schematic demonstration of liquid−air interface self-assembly of the semiconductor nanoplatelets (NPLs). (b) SEM micrograph of one monolayer of NPLs. (c) Photograph of one monolayer of NPLs deposited onto fused silica illuminated under UV light. (d) Cross-sectional transmission electron microscopy (TEM) image of the 11 NPL monolayers sequentially deposited onto silicon. All the NPL layers are distinctly visible, separated by their surface ligands. Reprinted with permission from *Nano Lett.* 2020, 20, 9, 6459–6465. Copyright 2020 American Chemical Society.

Such a technique allows for creating closely packed nanocrystalline films over large areas and with relative ease, but is not suitable for more complex structures with defined geometry and anisotropy. Several issues arise also for the assembly via external fields. The exemplary ensembles of polymer-grafted metal-oxide NPs,[111] semiconductor nanocrystals,[112] carbon-based nanocomposites[113] and ferromagnetic NPs,[114] created via electromagnetic fields, were hindered by the dielectric instability of polymers and constrained to particular material composition. The assembly by hydrodynamic flow fields that, in principle, can be generated by a variety of underlying processes,[115] such as shear,[116] evaporation,[117] gradients in temperature[118] or surface tension,[119] and capillary forces[120] is likewise limited in terms of the geometry and size of the pattern.[121]

To avoid the abovementioned obstacles and, at the same time, preserve the scalability and cost-efficiency of the assembly via external fields, a pre-structured template can be implemented.[122,123] Such a combination enables virtually any lattice symmetries, controlled local anisotropies, and interparticle distances.[124] Physically structured

templates have the advantage of being less susceptible to environmental conditions, in contrast to chemical patterning.[125] The microstructure of the template serves as a set of energetic minima, where the NPs are guided via the interplay of various attractive and repulsive forces. Thus, for successful template-assisted self-assembly (TASA), particular care must be taken of the surface properties of both: NPs and the template, to promote the desirable interactions and suppress the rest.[124] Via chemical modification one can control the surface free energy and, correspondingly, the wettability of the template with the respective solvent.[126] For colloids, the surface features are mostly defined by the ligands that surround a NP, whose primary function is to prevent the collapse of a colloidal suspension. The short-range attractive van-der-Waals forces, induced by the dipole interactions within constituent atoms and molecules of NPs, are opposed by the electrostatic repulsion of the similarly charged surfaces of colloids. In such a way, semiconductor QDs capped with long-chain organic acids, such as thioglycolic (TGA) or oleic acid (OA), experience repulsive interaction due to the partial deprotonation in respective solvents. Additionally, utilizing more than one capping agent, i.e. the mixture of OA and oleylamine (OLA) allows to maximize the PLQY and prevents oxidative degradation of perovskite nanocrystals.[127] When NPs approach other, long polymer chains provide additional steric stabilization via entropic forces and rise in osmotic pressure.[128] Similarly, for metal NPs, improved steric hindrance can be achieved by grafting polymer ligands, such as polyethylene glycol (PEG). Taking into account the great variability of the ligands, carved for specific purposes and functionalities, there is a clear need for a suitable assembly approach that can be easily adapted for various NPs. One of the simplest solutions is offered by the spin-coating technique (Figure 3a,b). In this way, metal NPs were assembled within a periodic template over macroscopic areas into closely packed lines, demonstrating plasmonic coupling effects.[129] Similarly, semiconductor nanocrystals were deposited over corrugated substrates and photonic crystals.[130–132] The simplicity of this approach is marked, however, by significant material waste during the spin-coating procedure and high concentrations of the colloidal solutions, required to fill in the patterns. A more elegant technique is based on the combination of meniscus pinning effects at the structural features of the template and convective hydrodynamic flows (Figure 3c,d).[133] Termed as capillary-assisted-particle-assembly (CAPA) it demonstrated its potential for assembly of NPs of virtually any shape and functionality, namely: spheres,[66,134–136] nanorods[120,137] or polygons,[138,139] as well as for sequential assembly of composite clusters.[140,141] The utilization of this technique is limited,

however, to the geometrical size of the NPs: for smaller particles, the diffusive effects become more significant than the capillary forces.[142] Thus, CAPA remains inapplicable for typical semiconductor QDs with sizes below 10 nm, however, it has been recently demonstrated for fluorescent nanodiamonds of 50 nm in diameter[143] and since it is mostly performed in aqueous solution, cannot be employed for nanocrystals, susceptible to humidity.[144]
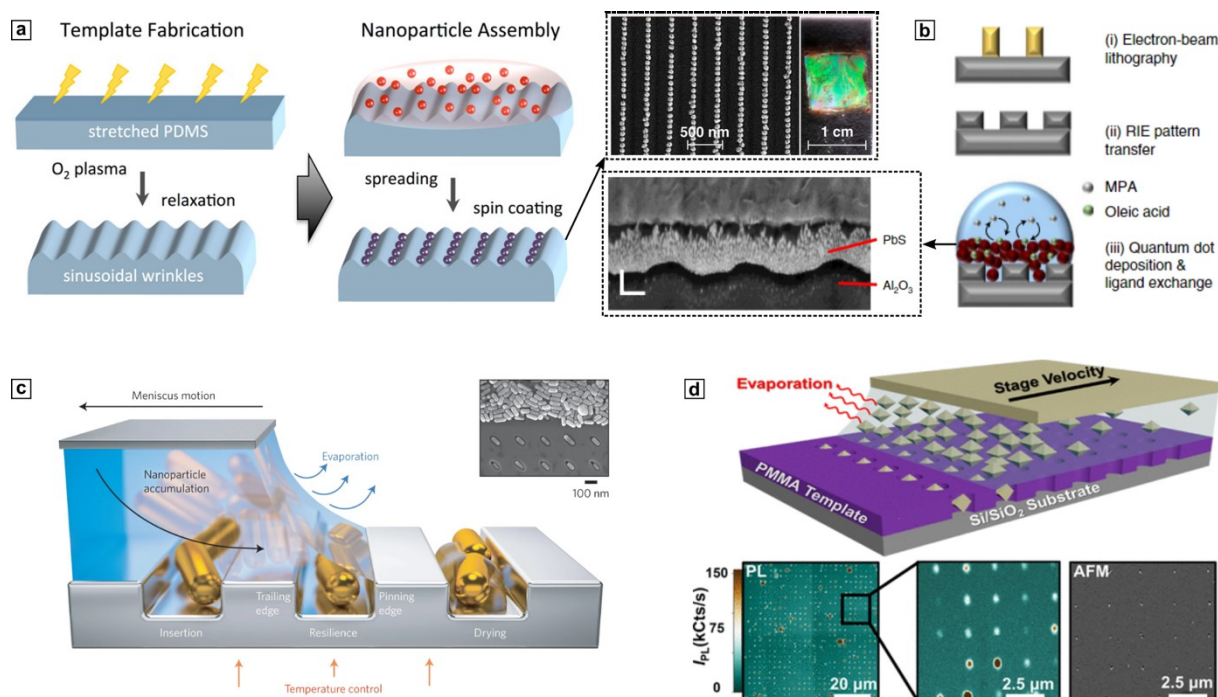

Figure 3: TASA on a structured substrate of (a) metal and semiconductor (b) nanoparticles. The insets in the middle demonstrate the SEM and focused ion beam (FIB) micrographs of the corresponding structures. (a) Reprinted and adapted with permission from *Nano Lett.* 2014, 14, 12, 6863–6871. Copyright 2014 American Chemical Society. Further permissions related to the material excerpted should be directed to the ACS. (b) Adapted by permission from Nature Publishing Group: Springer Nature, *NaturePhotonics*, Solution-processed PbS quantum dot infrared laser with room-temperature tunable emission in the optical telecommunications window, G. L. Whitworth et al, Copyright (2021) Nature Publishing Group. Representative CAPA of metal nanorods (c) and (d) fluorescent nanodiamonds. (c) Adapted by permission from Nature Publishing Group: Springer Nature, *Nature Nanotech* Nanoscale topographical control of capillary assembly of nanoparticles, Valentin Flauraud et al, Copyright (2016) Nature Publishing Group. (d) Reprinted with permission from *ACS Nano* 2022, 16, 2, 1847–1856. Copyright 2022 American Chemical Society.

Another template-assisted approach – the so-called nanoimprint lithography (NIL) - is based on drop-casting and confinement of the colloidal solution in between the structured template (mold) and the flat surface. The NPs are then driven by the external pressure of the template and the capillary action, given sufficient wettability of the template. For a successful filling of the gap, the rate of capillary rise must exceed the evaporation.[145] With such a relatively simple working principle, various structures

were already successfully realized: metal NPs were arranged into pyramidal,[146,147] linear,[148] circular[149] and multi-junction structures[150], similarly to the assemblies of QDs represented by 1D-linear,[151] 2D-square[145] and circular[152] lattices. Depending on the material of the stamp, one can distinguish between hard and soft nanoimprint lithography. The usual silicon or fused silica templates quite often suffer from the irreversible contamination of the mold by the colloidal solution, inherent brittleness under long-range deformations and insufficient vapor permeability that is needed for efficient solvent evaporation.[153] On the contrary, polymer-based soft molds tackle the abovementioned problems, being able to deform according to the features of the substrate and low cost in manufacturing. The molds are usually prepared by casting the polydimethylsiloxane (PDMS) into a pre-designed master template, where the desired features are replicated as relief patterns.[154] The polymer itself is highly permeable to the vapors of various solvents that creates beneficial conditions for the capillary forces, driving the assembly.[155] At the same time, its geometrical design is of vital importance[156] and is directly related to the master template manufacturing. The typical strategies for the latter include EBL or mask-assisted photolithography.[124] Whereas they allow for producing fine structures with a high lateral resolution of the geometrical features, including these techniques in experimental procedures diminishes the benefit of cost-efficiency of nanoimprint lithography. An alternative solution is offered by mask-less laser interference lithography (LIL) – a patterning method, where the pattern is recorded into a photosensitive medium through exposure to the interfering coherent beams of light.[157] Thus, the LIL-based NIL offers a universal and low-cost approach for directed TASA of colloidal NPs.

1.4. Scope of the thesis

This work focuses on colloidal metasurfaces, built out of metal and semiconductor colloids using LIL based TASA technique over large areas, and studies the emerging anisotropic and non-linear optical effects. Figure 4 below illustrates the scope of the thesis. To understand the complex collective optical behavior of colloidal metasurfaces, single colloidal building blocks are considered at first. Gold nanospheres that give rise to LSPR are used as a model example to illustrate the strong size-dependency of the optical properties (see **Chapter 2**). The characteristic optical responses, being the signature of the LSPR for nanoparticles of various sizes, are correlated with the corresponding perceived colors, by developing an open-source

spectrum-to-color converting algorithm, based on Mie theory and colorimetry. With this, one brings up the basic concepts of colloidal building blocks in a conceptual way.
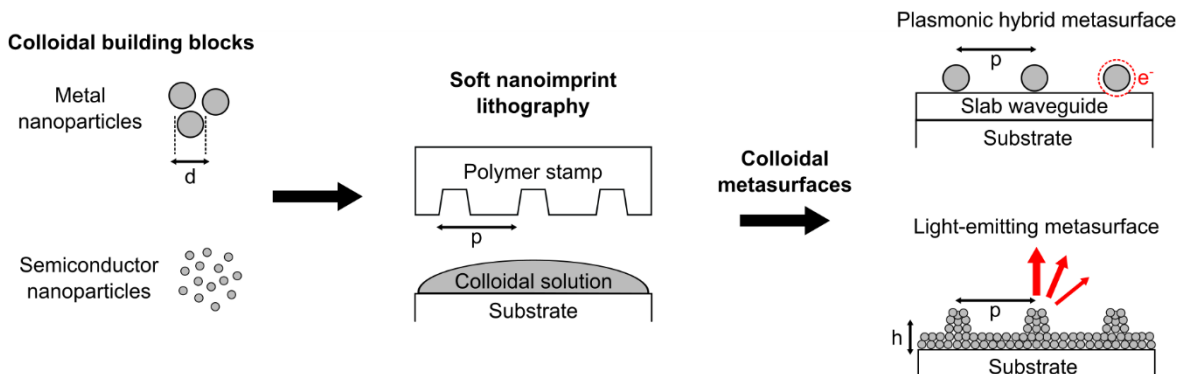

Figure 4: Schematic representation of the scope of this work, where self-assembly methods (LIL based TASA) are used to create emergent optical properties with colloidal building blocks.

Then, collective optical effects are brought into focus. This concept has already been extensively explored by the means of top-down lithography, disregarding the complexity and high cost of the manufacturing procedure. Hence, this thesis aims at utilizing colloidal self-assembly to create large-area metasurfaces with tailored properties. In particular, soft NIL is chosen for its robustness and cost-efficiency. In contrast to other approaches, such as CAPA, it can be utilized for colloids of various sizes and materials, dispersed in aqueous as well as organic volatile solvents. In **Chapter 3**, the potential of combining NIL and LIL is demonstrated by creating periodic arrangements of colloidal metal nanoparticles on various target substrates with varied topography, conductivity, and surface chemistry. The manufactured metasurfaces feature optical anisotropy that arises from a 1D photonic crystal geometry, and, being printed on a waveguide-like layer, are employed to facilitate plasmon-induced charge transfer and photocatalysis.

The emission pattern of light-emitting, semiconductor colloids can be likewise controlled by arranging these building blocks into pre-designed patterns. Until now, it has been mostly realized through integrating semiconductor nanocrystals into existing photonic or plasmonic crystals, which demand increased production efforts and is limited to the geometry of the structured support. Therefore, in this work, the challenge of directly patterning semiconductor nanocrystals is addressed. **Chapter 4** describes in detail the transfer of the concept of laser-interference-lithography-based nanoimprint soft lithography to light-emitting metasurfaces. By arranging highly luminescent perovskite nanocrystals into periodic patterns, where the geometry, in particular – the periodicity (p) of the pattern, is controlled through the structured template, we achieve

control over the directionality and intensity of the output photoluminescence that until yet has been challenging to realize on a large scale and with a simple design. An in-depth study of the radiation patterns reveals superior anisotropic amplification of the photoluminescent signal that is demonstrated for the directly imprinted colloidal semiconductor nanocrystals in ambient conditions for the first time. Those results give an essential prerequisite for addressing the non-linear optical effects in **Chapter 5**. By employing a similar strategy to design a resonant structure and utilizing highly stable and robust quantum emitters, a nanolaser is developed. In contrast to conventional top-down electron-beam lithography methods, the lasing metasurface is created over a centimeter-scaled area preserving the nanometer-precision of the structural geometry. To manufacture such structures, the cost-efficient soft nanoimprint lithography is combined with the directed Langmuir-Blodgett assembly on the water-air interface to achieve nanometer control over the thickness (h) of the resonant structure. The final **Chapter 6** elaborates further on creating hybrid configurations, consisting of separately manufactured metasurfaces. In this part, the soft nanoimprint lithography is applied toward water-dispersed colloidal quantum emitters, assembling them into 1D sub-micrometer gratings on a flexible substrate. Combining such metasurfaces by simple stacking at various angles results in a tunable Moiré pattern and leads to a chiroptical effect with a remarkably high degree of polarization, without a need for an additional chiral template as an intermediary.

To summarize, this work takes the advantage of template-assisted self-assembly of plasmonic and light-emitting colloidal building blocks and explores the versatility of their collective optical responses toward functional metasurfaces.

2. Optical properties of single nanocrystals via color perception of colloidal gold

This section is based on the peer reviewed journal article. Reprinted with permission from *J. Chem. Educ.* **2021**, 98, 8, 2566–2573. Copyright 2021 American Chemical Society.

Olha Aftenieva,[1,#] Daniel Schletz,[1,6,#] Antonia Meyer,[2,3] Tino Kühne,[4] Sierk Schmalzriedt,[5] Manuela Niethammer,[4] Tobias A. F. König[1,6,*]

1. Leibniz-Institut für Polymerforschung Dresden e.V. (IPF), Hohe Str. 6, 01069 Dresden, Germany

2. Martin-Andersen-Nexö-Gymnasium, Haydnstraße 49, 01309 Dresden

3. Technische Universität Bergakademie Freiberg, Akademiestraße 6, 09599 Freiberg

4. Berufliche Fachrichtung Labor- und Prozesstechnik; Didaktik der Chemie, Technische Universität Dresden, Weberplatz 5, 01217 Dresden

5. Studio Fluffy – Gesellschaft für Kunst und angewandte Mathematik UG, Gottesauer Straße 33a, 76131 Karlsruhe

6. Center for Advancing Electronics Dresden (cfaed), Technische Universität Dresden, Helmholtzstr. 18, 01069 Dresden, Germany

*Corresponding author: koenig@ipfdd.de

#Equal contribution: O.A., D.S.

Author contribution statement

O.A. and D.S. contributed equally to the preparation of the manuscript. **O.A.** performed the numerical calculations and developed the color conversion concept. D.S. performed synthesis of gold nanoparticles and transmission electron microscopy imaging. A.M. assisted in the concept development and nanoparticle synthesis. T.K.

and M.N. contributed to the development of the didactic concept. S.S. created and implemented the interactive digital platform NZONE. T.A.F.K., **O.A.** and D.S. supported the manuscript writing process and were involved in the scientific discussions. T.A.F.K. supervised the project, contributing in developing both scientific and didactic concepts.

Introduction

In contrast to a macroscopic solid, the color and spectroscopic properties of gold nanoparticles (AuNPs) change with size. The interaction of visible light with nanoscopic metallic particles induces resonant oscillation of free electrons within the metal. Such oscillations, confined to a particle surface, are termed as localized surface plasmon resonance (LSPR), and the particles, correspondingly, plasmonic NPs.[43] This nanoscale effect results in distinctive scattering and absorption properties that, in their turn, affect the perceived color. One of the most illustrious examples of this is the Lycurgus cup, a Roman glass vessel from the 4th-century, which contained metal NPs. The cup appears ruby red in transmitted light and is green in reflection.[158] Nowadays, researchers have a variety of elaborate synthesis methods at their disposal to reproduce such plasmonic NPs, several spectroscopic methods to quantify them, and simulation methods to describe the LSPR effect theoretically.[159] Characteristic optical and electronic properties of metal NPs allow for their abounded applications in information storage, nanophotonic devices, and sensors.[160,161] Thus, being one of the vastest research fields for the 21st-century, plasmonic nanotechnology must be established as one of the standards of science university education since its public perception is of great importance for social acceptance and further development. However, this aspiration comes with a great challenge of explaining the nature of the light-matter interaction that involves specialized physical concepts, as was recently reported by Markina's research group.[162] Standard models, required for the description of the complex theory of plasmons, are often far beyond the school education level. Thus, we propose to tackle this problem by creating a color-based perceptual connection to the field of plasmonic nanotechnology with the help of a learning platform and adapting it to the heterogeneity of the target group.

When describing the ruby color of plasmonic NPs, the conventional color formation theory has to be reconsidered. The apparent contradiction with the golden color of the bulk material is explained through the transition from macro- to the nanoscale, where

optical properties and, thus, perceived colors, are dictated by plasmonic effects, depending on the size, shape, and environment of NPs.[43] Lagorio's theoretical work describes this transition in color perception for students in advanced studies.[163] Although there is a wide range of established synthetic protocols for gold nanospheres of different sizes, achieving a colloidal size distribution narrow enough to match theoretically predicted plasmonic effects is challenging.[164,165] To avoid that and aim for a quasi-spherical shape of the gold NPs, a seed-mediated growth method has to be employed.[11] Although covering such theoretical details is crucial for the full understanding, to motivate the target group to explore the optical properties of plasmonic NPs, one has to develop learning approaches that go beyond a simple explanation of the phenomenon. For this, we combine a standard picture-text-based presentation of the research content with digital formats that complement the conventional approach, suggesting an alternative interactive learning pathway to the user. This allows for reaching a heterogeneous audience and enables incorporating the digital demonstrators into outreach activities or practical laboratory courses.

2.1. Color perception through scattering and absorption effects

The color perception of a colloidal gold solution is one of the most intuitive approaches to describe the physicochemical properties of plasmonic NPs.[7] For this, the notions of color in reflection or transmission have to be reconsidered with respect to the nanoscale effects. When an object has dimensions much smaller than the wavelength of impinging light, along with the mirror-like reflection from the surface, the light ray is also scattered in different directions. Besides scattering, when passing through the medium, partial absorption of light takes place. By definition, combined attenuation of the incident light through scattering and absorption is called extinction.[166] Thus, microscopic reflection is equivalent to scattering at the nanoscale, while transmitted light refers to the extinction effect. Figure 5a shows flasks with gold colloids synthesized by Richard Zsigmondy that exhibit various shades of red due to their different sizes, corresponding to their extinction under ambient room light.[167] Using a microscopy technique, known today as dark-field spectroscopy, Zsigmondy was able to separate the light, scattered by the NPs, and observe completely different colors (see Figure 5b). Since both scattering and absorption effects play a role in color perception, the first step in the development of a plasmonic learning platform is to

explain how the observed colors are governed by the particle sizes and the viewing position (see Figure 5c).

As mentioned earlier, the incident light, which resembles a combination of various wavelengths, induces the LSPR effect through the coherent oscillatory displacement of electrons within metal NPs (see the inset of Figure 5c). In their turn, they scatter and absorb only certain wavelengths, due to the size and material properties. The light that reaches the observer's eye after interacting with the NPs depends on the relative positioning of the light source and observer, which results in different color perception. Looking from the side, only scattered light reaches the eye, forming the color caused solely by scattering. On the other hand, the observer, positioned in line with the light source, receives the transmitted light, affected by both: absorption and scattering effects. Thus, the color of the colloidal NP solution, in this case, is caused by extinction.
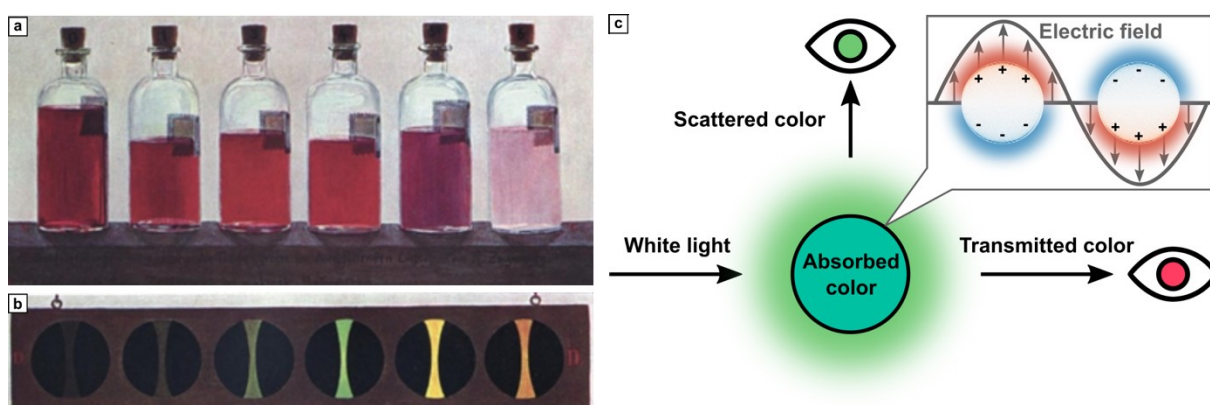

Figure 5: (a) The painted image from Richard Zsigmondy showing colloidal gold solutions of various sizes in a see-through fashion and (b) through a dark-field microscope.[8] (c) The concept of plasmonic color perception for the observer, positioned in line with the light source or off the direct light path. The color of the absorbed light, as well as the perceived colors, caused by scattering and extinction, were calculated using Mie theory and consequent spectrum-to-color conversion for a spherical particle with a diameter of 25 nm.

2.2. Spectrum-to-color conversion

To quantitatively attain the absorption, scattering, and extinction spectra of metallic NPs while utilizing minimal computational resources, the Mie theory is employed.[168] To get an intuitive representation of a particular spectrum, we developed a simple algorithm within the Python environment (see Figure 6). The usage of the algorithm requires minimal to zero programming knowledge since the user is only prompted to provide the input without any specific commands and the final result is displayed automatically on the screen after executing the code. First, the spectra of NPs with a certain size and in a certain environment, defined by a user, are presented. In its turn,

those spectra are then mapped with red $r(\lambda)$, green $g(\lambda)$, and blue $b(\lambda)$ color-matching functions (CMF).[169] This resembles an actual response of the human eye that possesses three types of cone cells, having different sensitivities for the short (blue), middle (green), and long (red) wavelengths of the visible spectrum and determining our color perception under the bright illumination.[170] Such mapping yields the so-called chromaticity values that undergo certain adjustments needed to make them reproducible by a computer monitor. As a final outcome, the user obtains the red (R), green (G), and blue (B) color-coding for the respective scattered, absorbed, and transmitted colors. The in-depth details of such spectrum-to-color conversion and exact requirements for running the code are given in the Appendix 8.1.
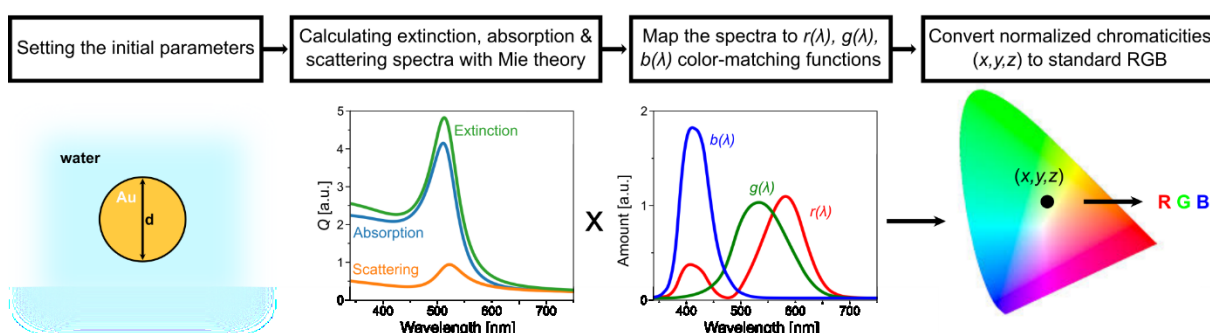

Figure 6: The descriptive flowchart demonstrating the spectrum-to-color conversion starting from defining the physical properties of a NPs and resulting in RGB-coded colors, caused by absorption, scattering and extinction effects.

In Figure 7, we selectively demonstrate scattering, absorption, and extinction spectra with the corresponding colors as a background for three different NPs diameters: 20 nm, 70 nm, and 130 nm that can be assigned as particles of small, medium, and large sizes. The extinction spectra feature a prominent resonant peak that indicates of the dipole-like oscillation of the electron density within the particle. However, for larger spheres, one can also identify modes of higher complexity at shorter wavelengths that appear as a shoulder on the left side of the main peak.[171] With the increase in size, the resonant frequency decreases, leading to a characteristic redshift of the dipolar LSPR peak. Another distinctive property related to the size is the prominent difference in scattering efficiency between small and large particles. The scattering efficiency Q_{sct} depends on the diameter d of the particle as $Q_{sct} \sim d^4$, whereas the absorption efficiency features a linear dependence.[172] Consequently, the color, caused by extinction, which one would see when looking through a flask containing a colloidal solution of the smallest particles is almost solely defined by absorption. Therefore, the solution appears pink-ruby, which is the complementary color to the blue-green colors that are

absorbed. The scattering efficiency is close to zero, so it does not contribute to the extinction. Scattering effects become noticeable for middle-sized particles and dominate in the extinction for large particles. This increased contribution from scattering to the overall extinction leads to a significant color change to Aegean blue.
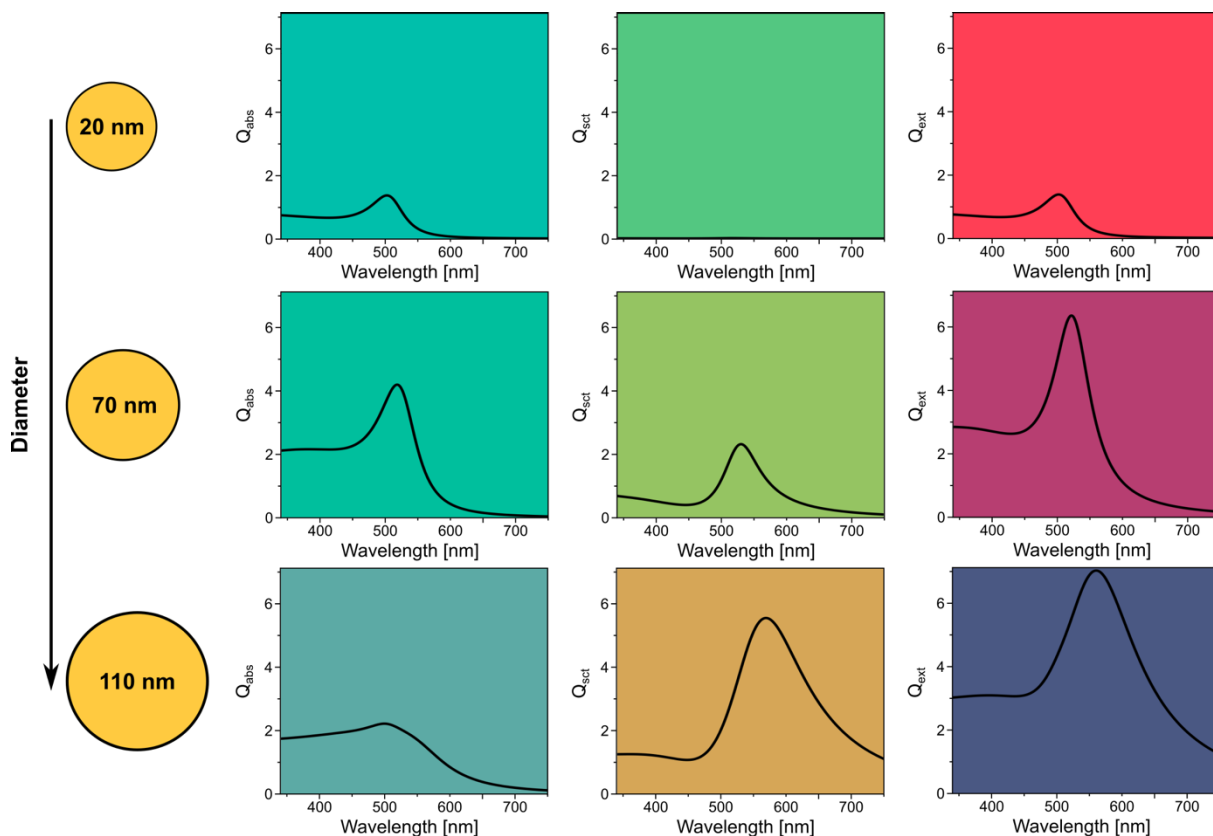
Figure 7: Scattering, absorption and extinction efficiencies are presented for gold NPs of three different sizes: 20 nm, 70 nm and 110 nm. The background color of the graph corresponds to the corresponding converted colors.

To support the applicability of the suggested spectrum-to-color conversion algorithm, the NPs library of spheres with various diameters was synthesized. For this purpose, the seed-mediated growth method was employed since it results in particles with almost perfect roundness, which eliminates the discrepancies during the color matching. A similar approach was used in a recently published laboratory experiment by Vinnacombe-Willson et al., where spherical and star-shaped particles were synthesized via seed-mediated growth by high school students.[173] The following synthesis was accomplished in a practical internship with high school students and, therefore, is described in a detailed manner.

2.3. Color validation

The precise control over size and shape, verified by transmission electron microscopy (TEM), is of paramount importance to enable a valid comparison to the theoretical model. The spherical shape of the synthesized particles allows for an unconstrained usage of the spectra, calculated by Mie theory, for the further spectrum-to-color conversion procedure. Figure 8 compares the theoretical and experimental results, where a clear match can be observed. When the observer (or the camera objective) is in line with the light source, the solution appears in different shades of ruby red to blue color that corresponds to the see-through color, caused by extinction, where part of the incident spectrum was attenuated by absorption and scattering effects. When the photo is taken from the side, avoiding the direct incident illumination, the scattered color, ranging from green to light-brown, can be distinguished. For the smallest particles, it appears, however, transparent. This can be attributed to a negligible contribution of scattering in comparison to absorption (1% to 99%). Green color becomes intense enough starting from the 70 nm sized particles, where scattering effects are comparable to absorption (37% to 63%). For the biggest particles with the size of 130 nm, scattering dominates the absorption (88% to 12%) and the scattered light-brown color is clearly visible.

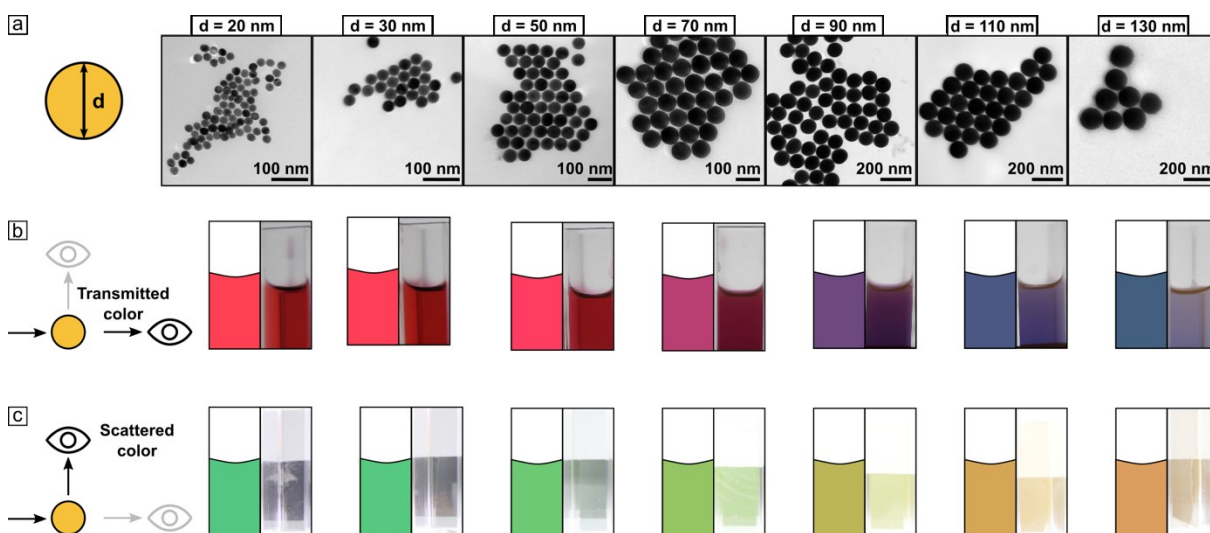Figure 8: (a) TEM micrographs of the Au NPs with the sizes 20, 30, 50, 70, 90, 110 and 130 nm. (b) transmitted and (c) scattered colors of the corresponding colloidal solutions photographed by a digital camera and calculated with the help of a spectrum-to-color conversion script. For capturing the scattered colors, the solution was diluted, the lighting adjusted and the flashlight of the camera was used.

Such a good agreement between the real-world colors with the calculated ones suggests a possible reverse prediction of the particle size based on the observed color.

Conclusion

In this study, we demonstrated how the difficulty of bringing up the complex concepts of nanotechnology could be overcome by using an interactive learning platform and exploiting the perceptual example of the color formation at the nanoscale. Without reducing the theoretical background, such visually intuitive explanation can benefit the scientific communication activities or practical courses at the high school or university. Moreover, the applied didactic approach, featuring the combination of research and teaching, allowed for creating an efficient approach to motivate the cognitive involvement of the students to the research-related topics. The created virtual platform serves as an instrument for further investigation of the learning pathways, exploring the question of how the learners can be prompted and encouraged to engage themselves with a complex scientific topic, such as plasmonics, and how to support their interest.

In the current state, the learning platform offers the potential for further development and content enrichment from optics, chemistry, didactics, and multimedia communication. The already existing chemical synthesis protocols, well-adapted for the high school and university students, can be complemented by the suggested platform to illustrate and predict the absorption and scattering effects caused by using different materials or producing particles not only in spherical but also in more complex, for instance, star-like shapes.[11,162,174,175] The platform also has the potential to interpret the concepts of the current research in a game-like format: e.g. through arranging several NPs into chains and introducing the plasmonic coupling.[50,176] Finally, the concept of this plasmonic teaching platform can be extended to other nanotechnology topics and promote the awareness of this promptly developing field.

3. Template-assisted self-assembly of plasmonic nanoparticles for enhanced photoconductivity and photocatalysis

Vaibhav Gupta,[1,2,#] Swagato Sarkar,[1,3,#] Olha Aftenieva,[1] Takuya Tsuda,[1] Labeesh Kumar,[1] Daniel Schletz,[1] Johannes Schultz,[4] Anton Kiriy,[1] Andreas Fery,[1,5] Nicolas Vogel,[2] Tobias A. F. König[1,6,*]

1. Leibniz-Institut für Polymerforschung Dresden e.V. (IPF), Institute for Physical Chemistry and Polymer Physics, Hohe Str. 6, 01069 Dresden, Germany

2. Institute of Particle Technology, Friedrich-Alexander University Erlangen-Nürnberg, Cauerstrasse 4, 91058 Erlangen, Germany

3. Department of Physics, Indian Institute of Technology Delhi, New Delhi, 110016, India

4. Leibniz-Institut für Festkörper- und Werkstoffforschung, Institute for Solid State Research Helmholtzstraße 20, 01069 Dresden, Germany

5. Physical Chemistry of Polymeric Materials, Technische Universität Dresden, Bergstraße 66, 01069 Dresden, Germany

6. Center for Advancing Electronics Dresden (cfaed), Technische Universität Dresden, 01062 Dresden, Germany

[#] These authors contributed equally

[*] Corresponding author koenig@ipfdd.de

Author contribution statement

V.G. and S.S. contributed equally to the manuscript. **O.A.** performed the laser interference lithography and PDMS mold fabrication. D.S. synthesized nanoparticles. V.G. and **O.A.** performed template-assisted lithography of AuNPs on various substrates. V.G. and S.S. performed the optical characterization. S.S. performed numerical simulations. T.T. performed the photocurrent measurements. L.K., V.G. and **O.A.** performed photocatalysis measurements. T.A.F.K., A.F. A.K. and N.V. supported the manuscript writing process, and were involved in the scientific discussions. T.A.F.K. and A.F. supervised the project, contributing to the concept development.

Introduction

Colloidal gold (Au) nanospheres render themselves as standard objects for observing nanoscopic light-matter interaction effects. They are superior to their counterparts, produced with standard top-down lithography methods, in terms of monodispersity, crystallinity, and possible surface functionalities.[177–179] Taking the advantage of the strong electromagnetic field confinement within a nanosphere in a form of localized surface plasmon resonances (LSPRs), their use was already successfully demonstrated in multiple applications, including the facilitation of photocatalysis through the generation of highly energetic charge carriers - the so-called 'hot electrons and holes',[180] strong coupling effects,[181] biosensing[182] and photovoltaics.[183,184] However, the inherent geometrical symmetry does not allow for expanding their use on anisotropic optical functionalities. To approach this issue, a great effort was made toward the chemical synthesis of anisotropic nanoparticle (NP) shapes.[13,185–188] At the same time, for on-chip device applications, the anisotropy has to be realized over macroscopic areas and on arbitrary substrates. In this regard, the assemblies of colloidal Au nanospheres can be deposited on a substrate of choice, serving as building blocks for the so-called plasmonic metasurfaces.[50] Controlling the internal structural organization of such assemblies not only opens new optical functionalities that are otherwise unattainable within single plasmonic nanospheres but also improves the quality of LSPRs, alleviating Ohmic losses via the scattered radiation fields.[44,189,190] However, it remains challenging to assemble colloidal building blocks on a large scale and in a cost-efficient way. Such techniques as DNA-mediated assembly,[191] dip-pen nanolithography[192] and electrostatic directed assembly[193] either lack in terms of scalability, insufficient resolution, or large interparticle spacing.

On the other hand, the combination of "top-down" and "bottom-up" methods, as in capillary assisted particle-assembly (CAPA),[106,120] transfer printing[135,194] or directed electrophoretic assembly[195] has great potential, demonstrating high positional control of colloidal NPs over macroscopic areas. However, these methods still constrain complete access to the colloid surface due to their residing in the template trenches, and operate with a limited selection of colloids and target substrates. To alleviate these limitations, nanoimprint lithography (NIL) can be employed. This simple yet powerful technique utilizes a pre-structured elastomeric stamp in the desired dimension for pattern transfer on a target substrate. It has already demonstrated its uses for surface-enhanced Raman spectroscopy[196–198] and nanoscale electronics.[199] The detailed optimization strategies were also discussed elsewhere, lacking, however, on the application aspects.[150]

Therefore, this particular work aims to bring forward the adaptability of the NIL technique, broadening the range of the device's applicability. In particular, the mask-free laser interference lithography (LIL) technique was combined with soft polymer molding to produce robust printing stamps for arranging high-quality colloidal Au nanospheres into plasmonic metasurfaces with 1D anisotropy on various target substrates. Periodically ordered, densely packed colloidal chains were printed on a transmission electron microscope (TEM) grid, glass, and silicon (Si) wafer substrate, Au and polymer films, as well as titanium dioxide (TiO_2) slab waveguide on a centimeter scale. To the best of our knowledge, such purely colloidal 1D lattice printed on TiO_2 thin films represents the first hybrid metasurface, produced via NIL on a centimeter scale. The possibility for the functional integration of such structures into optoelectronic devices was shown through hot electron injection through Au/TiO_2 heterojunction via selective excitation of the guided modes,[200,201] and facilitation of photocatalytic activity due to the angle-specific enhanced light absorption. Thus, the technique can be employed in various fundamental studies of charge transfer, nanochemistry, and solid-state device fabrication.

3.1. Fabrication of plasmonic metasurfaces via nanoimprint lithography

The nanoimprint lithography process starts with the fabrication of a soft elastomeric stamp (Figure 9a). First, a master template is prepared via LIL from photosensitive

material deposited on a glass substrate. In contrast to the master templates, manufactured with the help of electron-beam lithography (EBL), patterning of a surface area of ~1 cm^2 with LIL takes minutes, whereas covering the same area with EBL requires hours of uninterrupted writing, causing significantly higher production costs.[202] Next, the replica of the master template is created by casting polydimethylsiloxane (PDMS) elastomer onto the master template. After curing and peeling off, the soft polymer stamp with an inverse structure is revealed (Figure 9b). The atomic force microscopy (AFM) micrograph of the PDMS template and macroscopic intense diffraction color underlines the uniformity of 1D grating over centimeter-scaled areas. The utilization of such soft stamps plays a key role in the NIL process.[203] First of all, in comparison to brittle and costly hard stamps, PDMS is a robust and inert soft material that maintains its structure after peeling off and can be reused multiple times, after appropriate cleaning (for details see Experimental section).[150,204] Moreover, the flexibility of PDMS allows for conformal contact with the target substrate without applying any additional pressure, using just the weight of the stamp.[196]
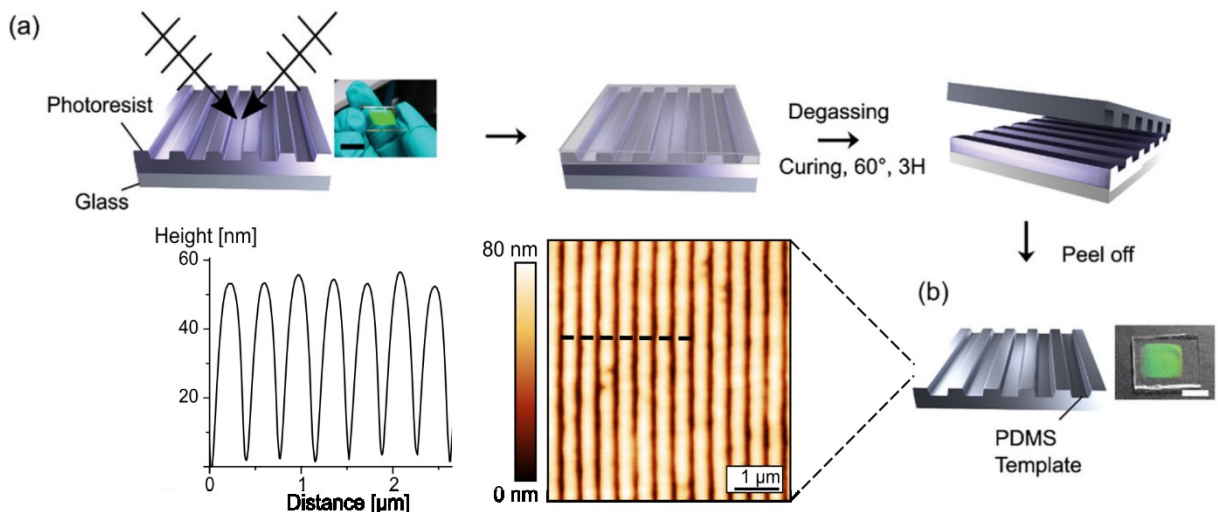
Figure 9: (a) Schematic representation of the preparation of the solid master template by LIL, followed by PDMS molding toward flexible inverse template formation. (b) Fabricated PDMS template together with the AFM micrograph and representative height profile along the selected direction, shown with black dotted lines. Scale bars in photographs correspond to 1 cm.

In this work, the printing process itself was demonstrated on conductive, dielectric, and organic-inorganic semiconductor substrates to showcase the versatility of the method. In all cases, the target substrate was rendered hydrophilic with oxygen plasma right before the assembly, ensuring a uniform wetting behavior over the entire substrate.

The drop-casting of the colloidal solution was followed by the accurate placement of the PDMS stamp, as shown in Figure 10a.

Figure 10: Arrangement of colloids in 1D-lines on substrates using the flexible PDMS mold. (b) Plasmonic metasurface, comprised of Au nanospheres (shown in the inset) covered with a polyethylene glycol (PEG) polymer shell that guarantees the colloidal stability in the solution. Scale bars in photographs correspond to 1 cm.

After the complete evaporation of water, which is possible due to the high permeability of PDMS to water vapor, and the removal of the stamp, the printed pattern was revealed, demonstrating the fidelity of the NIL over macroscopic areas (Figure 10b). The resu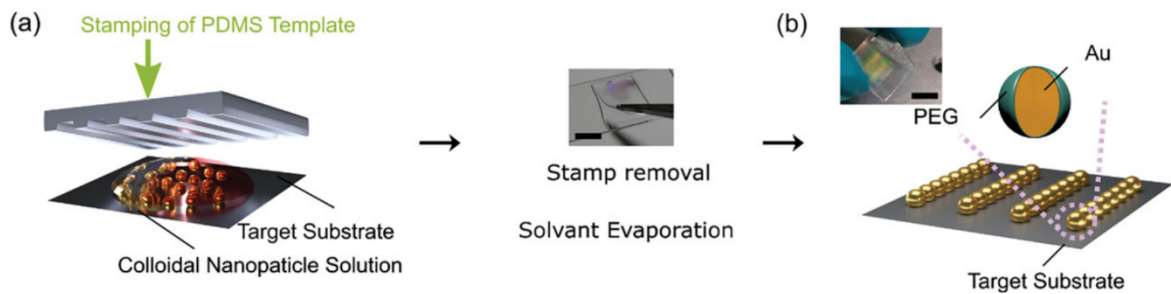lting structures represent 1D plasmonic metasurfaces, where the full surface of colloidal nanospheres, except a minimal area at the contact point of the particle and a substrate, is accessible to the surrounding medium.

3.2. Hybrid metasurfaces for optoelectronic applications

The described NIL technique was then applied for creating plasmonic metasurfaces on substrates with different functionalities (see Figure 11): TEM grid, microscope glass, Au, polymer, and TiO_2 (not shown) thin films, and Si wafer with a native silicon dioxide (SiO_2) layer. Figure 11a depicts the macroscopic photographs, confirming the fidelity of the assembly, together with the schematic representations of various configurations. The anisotropy of the created metasurfaces was then confirmed via optical microscopy under polarized illumination. The micrographs in Figure 11b demonstrate different colorations of the metasurface, depending on the relative orientation of the colloidal chains and the electric field of the incident light. The top row of images depicts the parallel configuration, where the vector of the electric field is aligned with particle lines, whereas in the bottom row the electric field is perpendicular to the lines. The drastic difference in the perceived colors originates from the characteristic scattering and

absorption effects in two different regimes of transversal (perpendicular) and longitudinal (parallel) coupling.[129]

Figure 11c shows scanning electron microscopy (SEM) and TEM images of the fabricated nanopatterns on various target substrates.
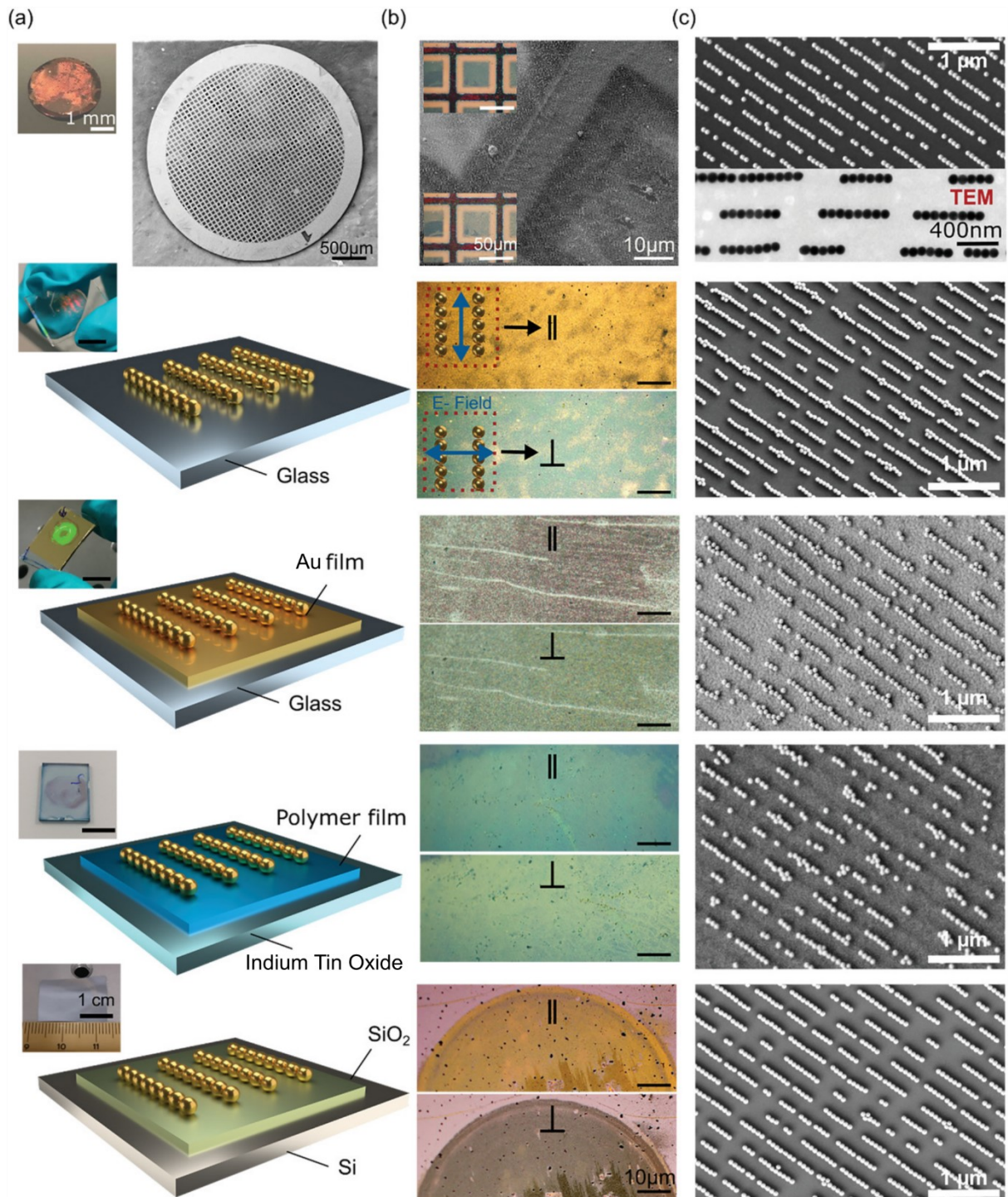
Figure 11: (a) Schematic of the plasmonic metasurfaces on various substrates. Inset shows photographs of actual fabricated samples. (b) Optical micrographs of the assemblies with polarized light illumination parallel (denoted as ||) and perpendicular (denoted as ⊥) to particle chains respectively. The blue arrow denotes the electric field

(E-field) direction. (c) SEM and TEM images of the particle lines on the corresponding target substrate. The Scale bars in SEM images are 1 µm.

During the assembly process within a confined space between the stamp and the substrate, the evaporation of the solvent causes attractive capillary interaction between the adjacent particles and breaks up the infinite chains into NP oligomers. Moreover, slight shrinking of the originally hydrated ligand shell leads to further distance variations along the chains.[129] For a more detailed analysis of the quality of the assembly on various substrates image analysis was employed (Figure 12).[205]
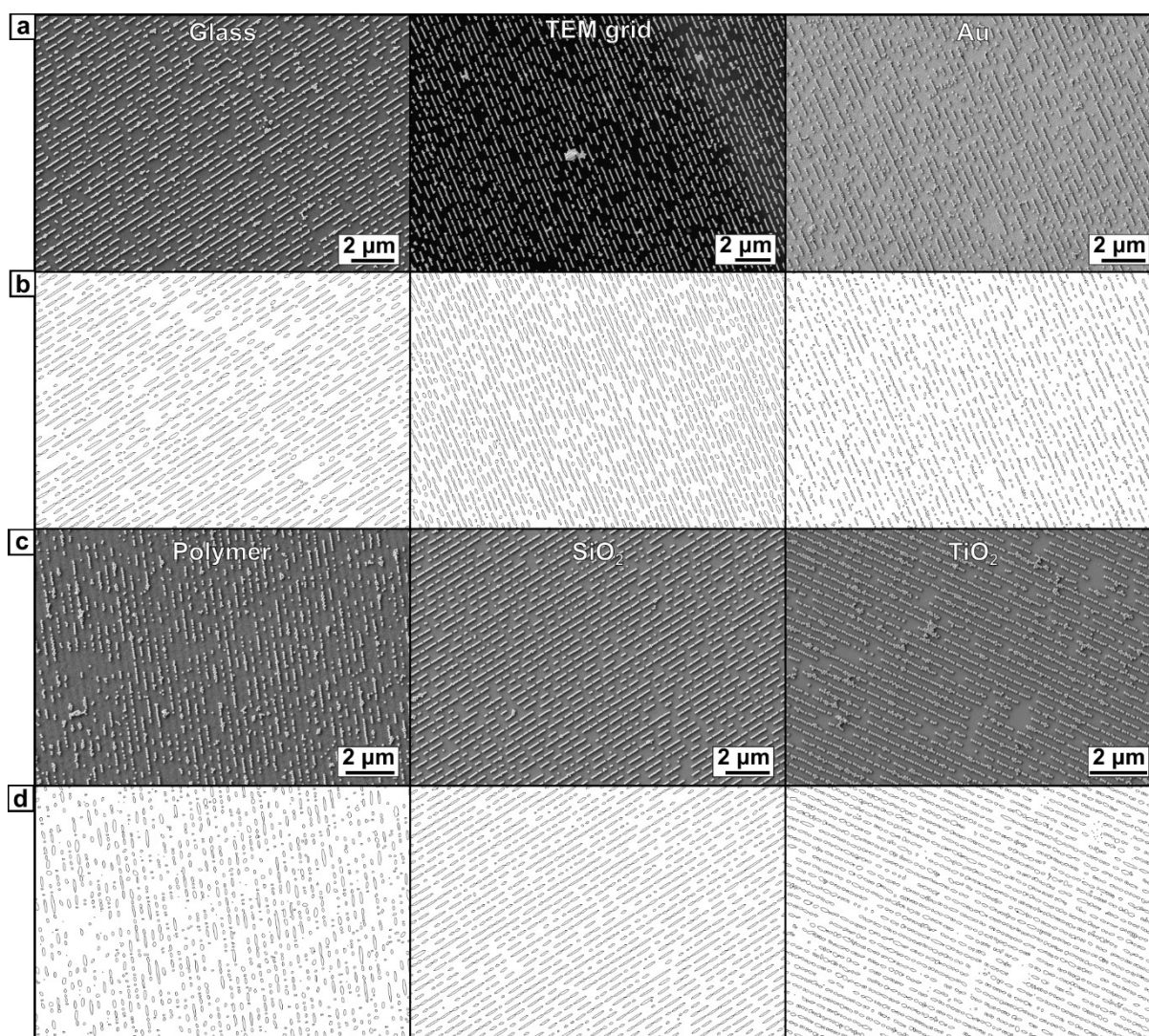
Figure 12: Image analysis of the (a, c) SEM micrographs of the plasmonic metasurfaces on various substrates. (b, d) Ellipses, fitted to the outlines of the NP chains.

First, the SEM micrographs were converted to binary images and analyzed by fitting the chain outlines with ellipsoidal shapes. For further analysis, only ellipses with a major axis more than the particle diameter, namely 75 nm, and a minor axis with dimensions between 75 and 150 nm, were considered. The average chain length was

calculated as the average of the ellipse's major axis values and comprised ~600 nm, which corresponds to ~8 particles per chain. The filling factor was calculated in the following way: SEM micrographs were converted to binary images, and the chain outlines were then fitted with ellipses, characterized by the major and minor axes parameters. The yield was calculated as the ratio of the sum of the major axis values to the total length of 'ideal' chains filled by 100%. Ellipses, where the minor axis was smaller than the particle size, or the major axis was not parallel to the direction of the particle lines, were excluded from consideration. In total, the analyzed area on various substrates constituted ~10 µm. The assembly yields were summarized in the Table 1 below:

Table 1: Assembly yields showing the fidelity of the NIL

Substrate	Glass	TEM grid	Au	Polymer	SiO$_2$	TiO$_2$
Yield	72.1%	74.0%	52.9%	59.5 %	75.4%	64.6%

As it follows from the image analysis, the assembly process is highly dependent on the roughness of the substrate. The yield of over 70% was achieved on commercial substrates such as silicon wafer, TEM grid, and microscope glass slide, in contrast to the electron-beam deposited materials such as TiO$_2$, Au, or spin-coated polymer film.

The overall purpose of extending the range of the target substrates was to make such NIL-made plasmonic metasurfaces suitable for various applications. For instance, the polymer film is comprised of naphthalene diimide-based pi-conjugated polycations that can be doped with electrons, representing a promising setup for an air-stable hot electron extraction system. Moreover, assembly of the 1D plasmonic lattice with the periodicity of 360 nm on a 200 nm-thick TiO$_2$ film allowed for generating hybrid guided modes under the polarized excitation, with the electric field vector, perpendicular to the direction of the lines. Due to the dispersive nature of guided modes, the coupling to the non-dispersive LSPRs under a certain angle of incidence of 15° resulted in a narrow-bandwidth Fano-like resonance with suppressed radiative losses.[73,206] The latter enabled the utilization of such hybrid plasmonic metasurfaces for hot electron generation[180] and photocatalytic activity, proven via the decomposition of an organic dye.

Conclusion

By combining laser interference and nanoimprint lithography techniques, plasmonic metasurfaces were created over macroscopic areas on various functional substrates in an easy, cost-efficient, and reproducible way. Non-destructive soft lithography approach allowed for retaining unique optical properties of colloidal building blocks and, together with the anisotropic coupling effects, stemming from the structural organization of the metasurface, deemed functional superiority of such hybrid structures in comparison to their counterparts, produced with pure top-down lithography methods.[207] The suggested approach can be integrated into the scalable roll-to-roll processes[208] and extended to more complex lattice geometries by employing multiple-beam laser interference.[209–211] Furthermore, to increase the optoelectronic potential, plasmonic building blocks can be coated with conductive polymers that retain the colloidal stability and enable higher photocurrents.[212] Altogether, the versatility and wide applicability of such hybrid metasurfaces pave a promising pathway for cost-efficient and large-scale optoelectronic device fabrication with the potential for scalability and commercialization.

Experimental section

Template Fabrication

To produce a structured polymer stamp, a soft lithography technique was employed. First, the master template was fabricated by the means of LIL on a glass substrate. For this, microscopy glass slides were divided into individual pieces (2 × 2 cm) and cleaned with isopropyl alcohol and ultrapure water in a 1:1 ratio by sonication for 20 min at 80 kHz. Positive photoresist (mr-P 1202LIL, micro resist technology GmbH, Germany), diluted with a thinner solution (ma-T 1050, micro resist technology GmbH, Germany) to a 1:1 ratio, was spin-coated onto the substrate. Optimized spin parameters of 3000 rpm, acceleration of 1000 rpm/s, and total spin time of 33 s produced a thin film of 80 nm thickness, as confirmed by spectroscopic ellipsometry (RC2-DI, J.A. Woollam Co., Inc.). The coated substrates were baked at 95°C for 60 s and further exposed to the 325 nm laser with a dose of 12 mJ/cm^2. The backside of the substrate was covered with black adhesive tape to avoid unnecessary reflections. To develop the exposed photoresist, the sample was submerged into the developer (mr-D 374/S, micro resist technology GmbH, Germany) for 40 s, rinsed with ultrapure

water, and dried under a stream of nitrogen. The total patterned area was in the shape of a circle with a diameter of 1.5 cm. The resulting periodic structure was modified via gas-phase deposition with trichloro(1H,1H,2H,2H-perfluorooctyl)silane (448931, Sigma Aldrich) at 60 °C for 3 h, and then molded with SYLGARD 184 Silicone Elastomer (The Dow Chemical Company, USA) in a 10:1 mixing ratio with the curing agent and cured for 3 h at 60 °C. After that, the PDMS stamp was peeled off from the master template and examined by the AFM technique, revealing a 1D grating with a periodicity of 360 nm and ~80 nm depth.

Soft nanoimprint lithography

The non-patterned region of the fabricated PDMS stamp was cut out before stamping to avoid wastage due to the formation of the particles on the target substrate outside the patterned area. Since no additional pressure was applied, the overall weight of the PDMS stamp was kept constant at 2.74 g. Then, 5 μL of the colloidal solution with an optimized concentration of 5 mg/mL was drop-casted on a pre-activated surface of a target substrate. The PDMS mold was immediately placed on the colloidal dispersion. The assembly was dried overnight at room temperature and relative humidity of 32%. The stamp was then removed by peeling off. Excess Au nanospheres, stuck in or onto the stamp, can be brought back to the solvent by ultrasonication, enabling re-usage of the stamp.

Surface characterization

Produced line structures were imaged with AFM. The scanning was performed in the tapping mode with silicon nitride probes (typical resonant frequency in the air: 296 kHz). Amplitude set-point was adjusted within the range of 100-200 mV at the scanning frequency of 0.5-1 Hz. For SEM, NEON 40 FIB-SEM workstation (Carl Zeiss Microscopy GmbH, Oberkochen, Germany), operating at accelerating voltage (electron high tension) of 1 kV was used.

4. Directional amplified photoluminescence in large-area perovskite-based metasurfaces

This chapter contains unpublished work, contributions to each part are to the date of the submission of the thesis.

Olha Aftenieva,[1] Julius Brunner,[2] Mohammad Adnan,[1,3] Swagato Sarkar,[1] Andreas Fery,[1,4] Yana Vaynzhof,[2,5,*] and Tobias A.F. König[1,5,*]

1. Leibniz-Institut für Polymerforschung e.V., Hohe Straße 6, 01069 Dresden, Germany

2. Integrated Centre for Applied Physics and Photonic Materials and Centre for Advancing Electronics Dresden (cfaed), Technical University of Dresden, Nöthnitzer Straße 61, 01187 Dresden, Germany

3. Physikalisches Institut, WWU Münster, Wilhelm-Klemm-Straße 10, 48149 Münster, Germany

4. Technische Universität Dresden, Helmholtzstraße 10, 01062 Dresden, Germany

5. Center for Advancing Electronics Dresden (cfaed), Technische Universität Dresden, 01062 Dresden, Germany

* Corresponding authors: yana.vaynzof@tu-dresden.de, koenig@ipfdd.de

Author contribution statement

O.A. performed the template fabrication, nanoimprint soft-lithography, microscopic and spectroscopic characterization, and numerical simulations. J.B. synthesized perovskite nanocrystallls and performed the in-sol spectroscopic characterization and transmission electron microscopy imaging. M.A. and S.S. assisted in the concept development and spectroscopic characterization. T.A.F.K. and J.V. supported, supervised, and leaded the concept development, scientific discussions, and manuscript writing. All authors provided critical feedback and helped in the data analysis and writing manuscript.

Introduction

Recently, perovskite nanocrystals gained particular interest, due to their solution processability, broad bandgap tunability, strong photoluminescence (PL), and high refractive index values.[213–217] In particular, inorganic perovskites demonstrate high quantum yields,[218] are less prone to crystal phase instability,[219] and are less susceptible to degradation in the ambient conditions due to the absence of organic component.[220–222] Cesium lead triiodide (CsPbI$_3$) perovskites that were first discovered in 1958 are now considered a standard perovskite material and since then regained interest for photovoltaics and light-emitting applications.[223–228] Their synthesis reveals now a well-established, scalable procedure and yields nanocrystals with strong PL, which is most critical for constructing an efficient metasurface. To ensure the long-term phase stability and prevent the propagation of the defects in the crystal lattice, CsPbI$_3$ perovskites, capped with oleic acid (OA) and oleylamine (OLA), can be additionally encapsulated into a polymer matrix that not only protects from humidity,[229] but also creates a uniform refractive index environment that is favorable for the optical performance.[230] Altogether, this makes perovskites ideal building blocks for colloidal light-emitting metasurfaces – a new class of periodically ordered assemblies on planar surfaces.[50] The concept of shaping the wavefront of luminescent bulk material is based on controlling the building blocks of a metasurface at the nanoscale.[231] The inherent presence of a periodic arrangement on a metasurface implies the emerging diffractive effects. The classical diffraction theory does not consider the material of the grating itself, but rather operates with its geometry and the properties of the surrounding medium.[232] An extended theory requires, however, the consideration of the grating composition: such as in the well-known case of metallic corrugated surfaces, the diffuse diffraction anomalies originate from the excitation of surface plasmons polaritons.[233] Similarly, one could expect the interplay of the diffraction features with the PL, when the periodic structure comprises a light-emitting matter, and, therefore, acts by itself as a light source. This notion is supported by the fact that spontaneous emission is not an inherent property of the material, but rather arises from the interaction of the material with its local electromagnetic environment.[234] The concept of such light-emitting metasurface is depicted in Figure 13: by introducing rational design and matching photonic features through the periodicity p of the structured surface to the material properties of perovskites, i.e. material refractive index n and PL, one can attain a certain degree of spatial

coherence, even though the isolated components of a metasurface emit incoherently. As a result, radiation pattern of a metasurface demonstrates amplification of the PL and directionality – increased photon counts in certain diffraction-defined directions.[145,234,235]
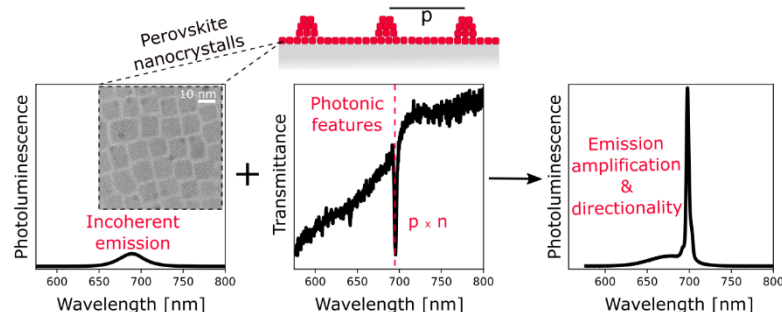

Figure 13: schematic representation of the light-emitting metasurface. The incoherent PL (left panel) of perovskite nanocrystals, shown in transmission electron microscopy (TEM) micrograph (inset, left panel). Exemplary transmittance spectrum under the normal incidence of a polarized broadband light source, showing the photonic features of the lattice, defined by the product of the periodicity – p, and refractive index of the environment – n (central panel). Resulting modified PL spectrum of a perovskite-based metasurface (right panel) with enhanced photon counts in the normal direction.

To introduce a periodic structural pattern into otherwise flat, continuous thin films of perovskites, the most straightforward method is through depositing colloidal nanocrystals on a pre-structured substrate. This approach was successfully applied for generating enhanced directional PL,[236,237] manufacturing nanolasers,[238–247] photodetectors[248] and solar cells.[249,250] However, such an indirect patterning method lacks the possibility of creating more complex, multi-component metasurfaces, provides sub-optimal electromagnetic energy confinement, and relies on an elaborated substrate preparation.[251] At the same time, direct patterning through ultraviolet (UV) or electron beam lithography (EBL) increases the risks of material degradation.[252–254] A more appealing, low-cost, and scalable approach implies direct patterning of perovskite thin films through nanoimprint lithography,[255] where the colloidal solution of perovskite nanocrystals (or their precursors that are further turned into a solid crystalline phase) is confined on the substrate by a structured stamp. As such, hard silicon (Si) stamps or glass-like molds were successfully employed to create structured metasurfaces with improved crystallinity[256,257] for modifying the emission properties[245,247,258–261] and for photovoltaic applications.[262–266] However, the usage of hard stamps requires additional surface modification and operation at high pressure and temperature. As an alternative, soft polymer stamps can be used, since they are low-cost in manufacturing and can be reused multiple times for pattern generation.[204,251] Until recently, such flexible molds, were mostly replicated from

compact or digital versatile disks, resulting in templates with only two fixed periodicities of 1.5 µm or ~750 nm, respectively,[151,266–269] or from masters, produced by cost-inefficient and poorly scalable EBL, reaching the periodicities of few hundred nanometers.[145,213,246,267,270,270–275] On the contrary, by employing laser interference lithography (LIL), one alleviates the abovementioned drawbacks and takes the advantage of submicron resolution and efficient large-area production.[210]

In this work, we employ the confinement self-assembly technique based on LIL and soft molding to create periodically patterned metasurfaces cost-efficiently and over centimeter-scaled areas. We provide a universal manufacturing procedure that implies its applicability to CsPbI$_3$ perovskite nanocrystals capped with a mixture of oleic acid and oleylamine as ligands and dispersed in organic solvents that, to the best of our knowledge, has not yet been studied in detail and optimized. The resulting metasurfaces feature periodicities ranging from a few hundred nanometers up to microns. We further provide a profound discussion on how the bulk PL of perovskites is altered by introducing the 1D periodic structuring, taking into account the angle- and polarization-dependent diffractive behavior of the created metasurfaces. With the help of angled-resolved spectroscopy, we demonstrate the directionality and multifold amplification of the PL. Here, we intentionally do not use the term 'amplified spontaneous emission (ASE) since the spectroscopic measurements were performed in a constant-wave (cw) mode, focusing rather on amplification factors and directionality, than on the input-output characteristics, typical for demonstrating ASE and lasing action. Moreover, we include the guided mode theory in the analysis that allows for in-depth structural and optical characterization of the metasurfaces and suggests strategies for their rational design for specific optoelectronic applications.

4.1. Concept of light amplification and directionality by metasurfaces, structured with 1D gratings

To understand the behavior of light-emitting nanostructures let us take a theoretical detour to the general theory of gratings. Already with the simplest configuration of a 1D periodic structure, a peculiar observation was made: when an incident light impinges on such a grating, a discontinuity in the spectrum occurs.[276] The geometry of the grating, namely, the periodicity, is directly related to the appearance of those anomalies, thereafter named Rayleigh anomalies (RAs). They appear in the spectrum

at a certain wavelength as abrupt changes in intensity.[232] Such an effect is explained by the propagation of the diffracted light of a certain order, tangential to the surface of the grating.[277] The position of the RAs in the spectrum is governed not only by the geometry of the grating but also by the refractive indexes of the surroundings, polarization, and the angle of incidence θ of the excitation light:

$$RA_{(0,\pm m)} = \frac{p}{m}\left(\mp \sin\theta + n_{sup/sub}\right) \tag{1}$$

$$RA_{(\pm m,0)} = \frac{p}{m}\sqrt{n_{sup/sub}^2 - sin\theta^2} \tag{2}$$

where p is the periodicity of the 1D grating, m is the corresponding diffraction order, and $n_{sup/sub}$ is the refractive index of the superstrate (medium above the grating) and the substrate (medium below the grating) respectively. The Equation 1 corresponds to transverse-magnetic (TM) polarization of the incident light, and Equation 2 – to transverse-electric (TE).[278]

The concept of how the PL behavior of bulk perovskites is altered by the presence of 1D gratings and, therefore, the corresponding RAs, is schematically depicted in Figure 14 and Appendix 8.2.1. The PL spectrum, ranging from 640 to 740 nm for the considered CsPbI$_3$ perovskites, can be approximated with a Gaussian function with a full width at half maximum (FWHM) from 670 nm to 708 nm and the peak maximum centered at 689 nm. The emitted light that is otherwise uniform for all angles of incidence and detection couples to the diffracted modes, where there is a wavelength overlap of the PL spectrum and the position of the RA. Hence, the coupling effect features the dependence on the periodicity of the grating, the angle of incidence of the excitation light source, and its polarization.
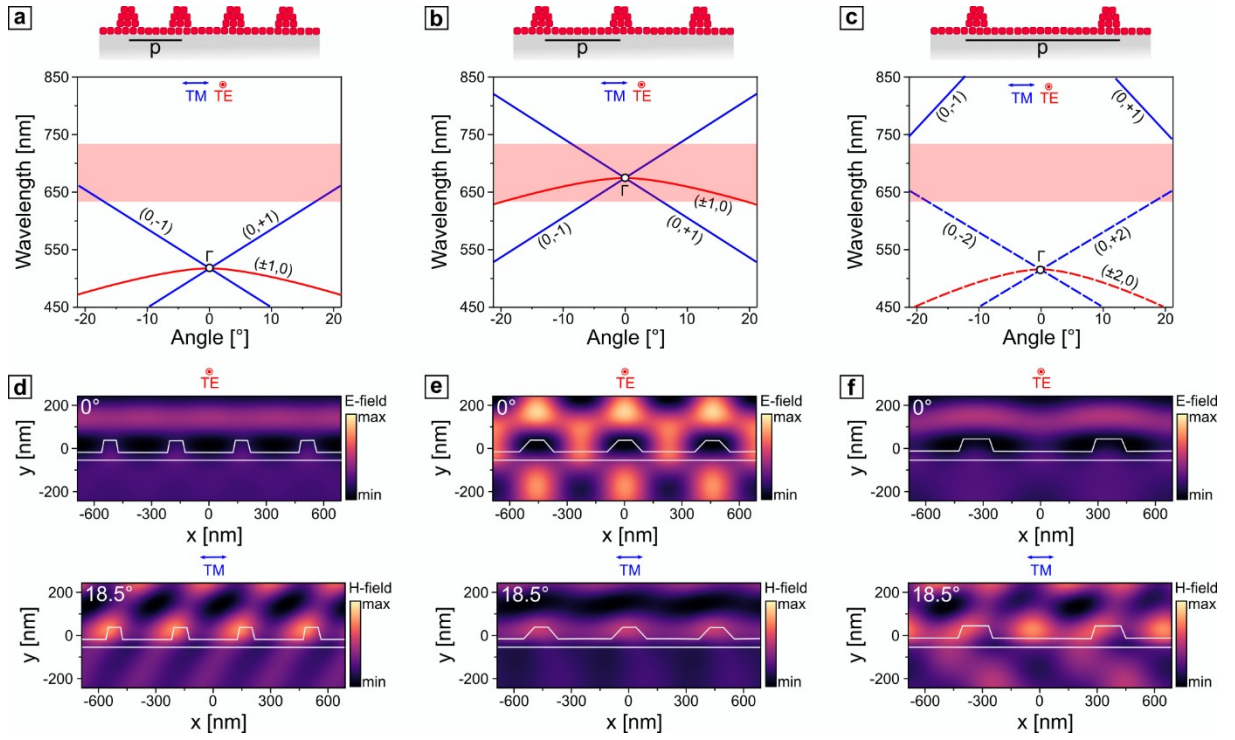
Figure 14: (a-c) Schematic representation of gratings of various periodicities and corresponding dispersion diagrams. The positions of Γ-point, 1st, and 2nd RAs are marked accordingly to the polarization of the excitation light. The exemplary emission band of the CsPbI3, spanning from 640 to 740 nm, is shown in light-red color. (d-f) Electric E-field (top row) and magnetic H-field (bottom row) distribution in three representative periodic structures under normal TE-polarized and angled TM-polarized incidence of a plane-wave light source, centered at the emission maximum. Material properties of perovskites were for the numerical simulations were determined via spectroscopic ellipsometry, described in details in Appendix 8.2.2.

When the parameters are chosen in such a way that the high-symmetry Γ-point overlaps with the emission, as shown in Figure 14b, a resonant interaction is expected due to the convergence of the diffraction modes for both TE- and TM-polarizations. For the TE mode, the electromagnetic field enhancement is most efficient for a range of angles near-normal incidence (Figure 14e, top row), contributing to the amplification and out-coupling of the emitted light. At the same time, TM-polarized modes are highly dispersive and overlap with the emission only at specific angles (Figure 14d,f, bottom rows). Following a particular diffraction order, they demonstrate stronger angle dependency than TE-modes. When the periodicity of the 1D grating is such that Γ-point does not match with the emission band, RAs at higher angles (18.5° in this particular example) of only TM-polarized modes interact with the emitted light. This induces the near-field enhancement under a particular angle that is reflected by an oblique magnetic field pattern as shown in the bottom row of Figure 14d,f. On the other hand, for the cases, where is no overlap of the emission band and RAs, no field enhancement is expected (bottom row of Figure 14e and top row of Figure 14d,f. In

such a way, by adjusting the parameters of the system, one can tune the position of the Γ-point and, either induce the outcoupling of the light in normal and near-normal directions with the TE-polarized modes or exploit the mismatch between the Γ-point and emission band for guiding the TM-polarized light at a specific angle.

4.2. Fabrication of light-emitting metasurfaces by soft nanoimprint lithography

To demonstrate both strong light amplification and directionality, we generated a set of metasurfaces, patterned with 1D gratings, with specified periodicities, pre-designed with the respect to the emission properties of $CsPbI_3$. Confinement self-assembly has been established as a versatile method to reliably arrange nanocrystals into nanostructures over a large area.[279,280] The details of the fabrication procedure can be found in the Experimental Section. Briefly, the colloidal solution of perovskite nanocrystals was confined between the substrate and a polydimethylsiloxane (PDMS) mold that acted as a structuring stamp. After evaporation of the solvent through the stamp, the revealed structure represents a reciprocal imprint of the template. Such a technique allows for scalable, single-step production of periodic structures over centimeter-scale areas, as shown in Figure 15a. Generally, the organic solvents that are common for dispersing perovskite nanocrystals are poorly compatible with PDMS. Less polar solvents, such as chloroform, hexane, or toluene, easily penetrate through the porous polymer mesh of PDMS, causing significant swelling, which, in its turn, leads to pattern distortions during the assembly.[281] The integrity of the pattern, however, is extremely important, since its geometry directly affects the diffractive behavior.[282] To prevent this, one can reinforce the PDMS stamp by changing the ratio of the prepolymer to the curing agent and subsequent thermal treatment.[283] Another challenge that arises during the assembly is the fast evaporation of the solvent. To minimize the latter, one should aim for the solvents with the lowest evaporation rate (lowest saturated vapor pressure). To estimate the effect of the solvent on the assembly quality, the perovskite nanocrystals were suspended in four different organic solvents, ranging in evaporation rate: chloroform, hexane, toluene, and octane (Figure 15b).[284] The quality of the assembly was then quantitatively accessed through the contrast measurements with the help of confocal fluorescence microscopy (CFM) imaging. For the contrast image analysis, the average contrast is defined as the average deviation of all points of the intensity profile from a mean line over the

evaluation length. The 1D gratings, assembled from colloidal solutions of the above-mentioned four different solvents are shown in Figure 15c. By comparing the intensity cross-section profiles across the CFM images perpendicular to the grating lines, one expectedly observes the lowest average contrast for the structure assembled using chloroform, where the fast drying of the solvent after the drop-casting results in a patchy pattern. Consequently, assembly with octane that has the lowest saturated vapor pressure, yielded higher contrast, implicating a more defined grating structure. However, the most pronounced contrast, and, thus, the best assembly quality was attributed to toluene. Although it has a slightly higher evaporation rate than octane, it also features four times higher polarity, which promoted the spreading of the colloidal solution over the intrinsically hydrophilic surface of the glass substrate.
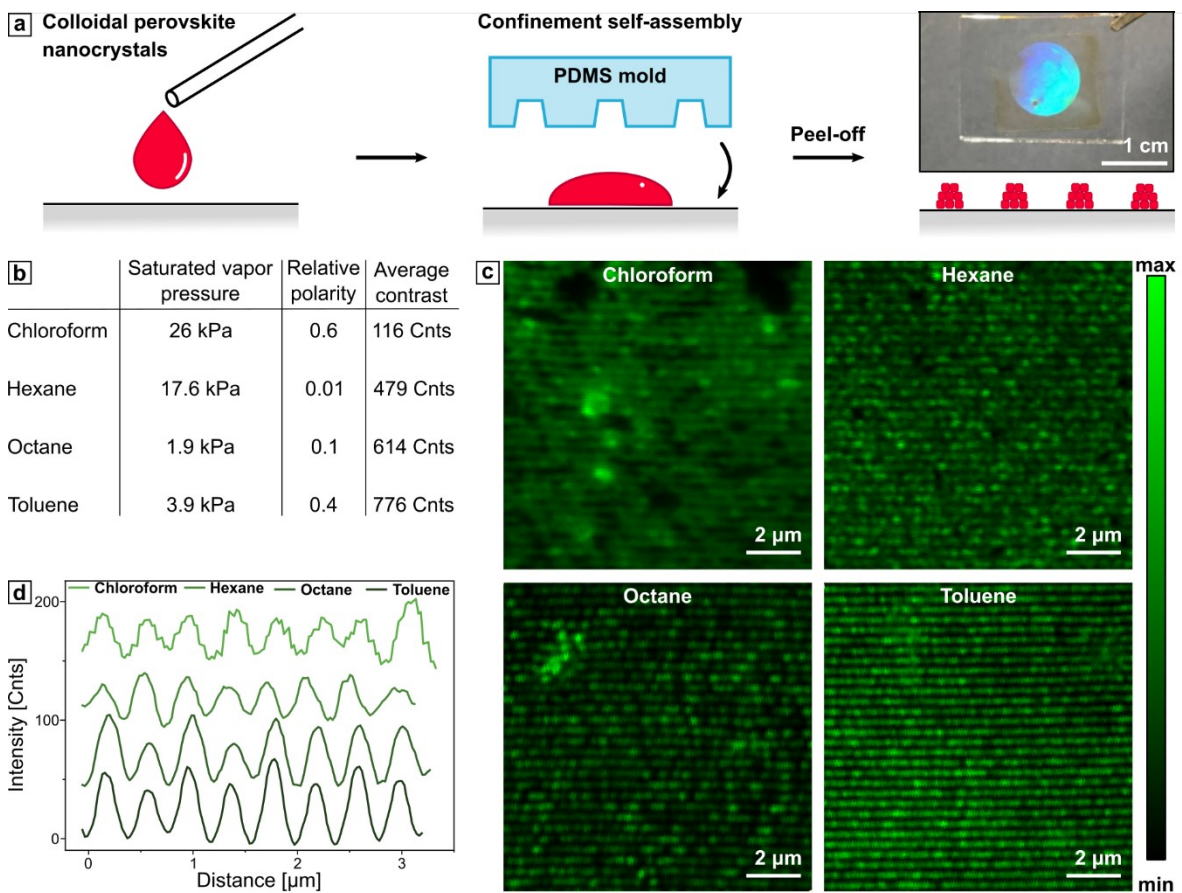
Figure 15: (a) Schematic representation of the assembly process together with a photograph of the large-scale assembly of the colloidal dispersion on the glass substrate under white light illumination. (b) Physical properties, affecting the assembly, for various solvents and the respective average contrast values. (c) CFM images of 1D gratings assembled from 5 mg/mL $CsPbI_3$ perovskites in corresponding solvents. (d) Intensity profiles from the CFM images shifted by 20 counts relatively to each other.

Besides the solvent itself, the concentration of the colloidal nanocrystals plays a significant role in the assembly process. Here we used solutions at relatively low

concentration (~5 mg/mL) that allowed for the assembly of only 1D grating lines, avoiding the accumulation of nanocrystals under the grating structure upon drying. However, by increasing the concentration of the colloidal solution, one can favor the formation of such layers that can be further exploited for waveguiding purposes (more details can be found in Appendix 8.2.3 and in the following chapters). In such a way, the confinement self-assembly of perovskite nanocrystals, suspended in toluene at low concentrations, yields well-defined 1D gratings, the periodicity of which can be easily pre-designed by choosing the PDMS molds of appropriate geometries.

4.3. Directional emission study by dispersion diagrams

In Figure 16, we fabricated 1D gratings with periodicities from 300 up to 1000 nm and performed the angle-resolved spectroscopy analysis to study the interaction of the omnidirectional emission of bulk perovskites with the diffractive behavior of the imprinted gratings. As well here, we used solutions at relatively low concentrations (~5 mg/mL) to minimize the accumulation of nanocrystals under the grating structure upon drying. After assessing the surface profiles of the metasurfaces, the samples were sealed with another glass slide, resulting in a uniform refractive index environment with $n_{sup/sub} = 1.55$. The polarization of the excitation light that also influences the appearance of the RAs was kept constant to demonstrate the effect of the varied periodicity of the 1D gratings. A flat, unstructured thin film was utilized as a reference (Figure 16a). This spectrum demonstrates the omnidirectional emission, uniform for all detection angles with an intensity maximum at 689 nm. For the grating with a periodicity of 300 nm, the 1st order RAs cross the emission band at the angles that are out of the observation range; hence, the angle-resolved PL profile appears similar to the one without any pattern. The presence of the structured surface becomes noticeable from 400 nm periodicities onwards, where the 1st order RAs overlap with emission and induce the PL amplification at particular angles, reflected by a higher number of detected photons along this direction (Figure 16c). Upon increasing the periodicity, Γ-point experiences redshift, and starting from 700 nm-gratings, already the 2nd order RAs begin to interact with the emission spectrum. Since the higher-order RAs feature lower diffraction efficiency,[282] their interaction with the emission spectrum is marked by less pronounced PL amplification at the corresponding angles.
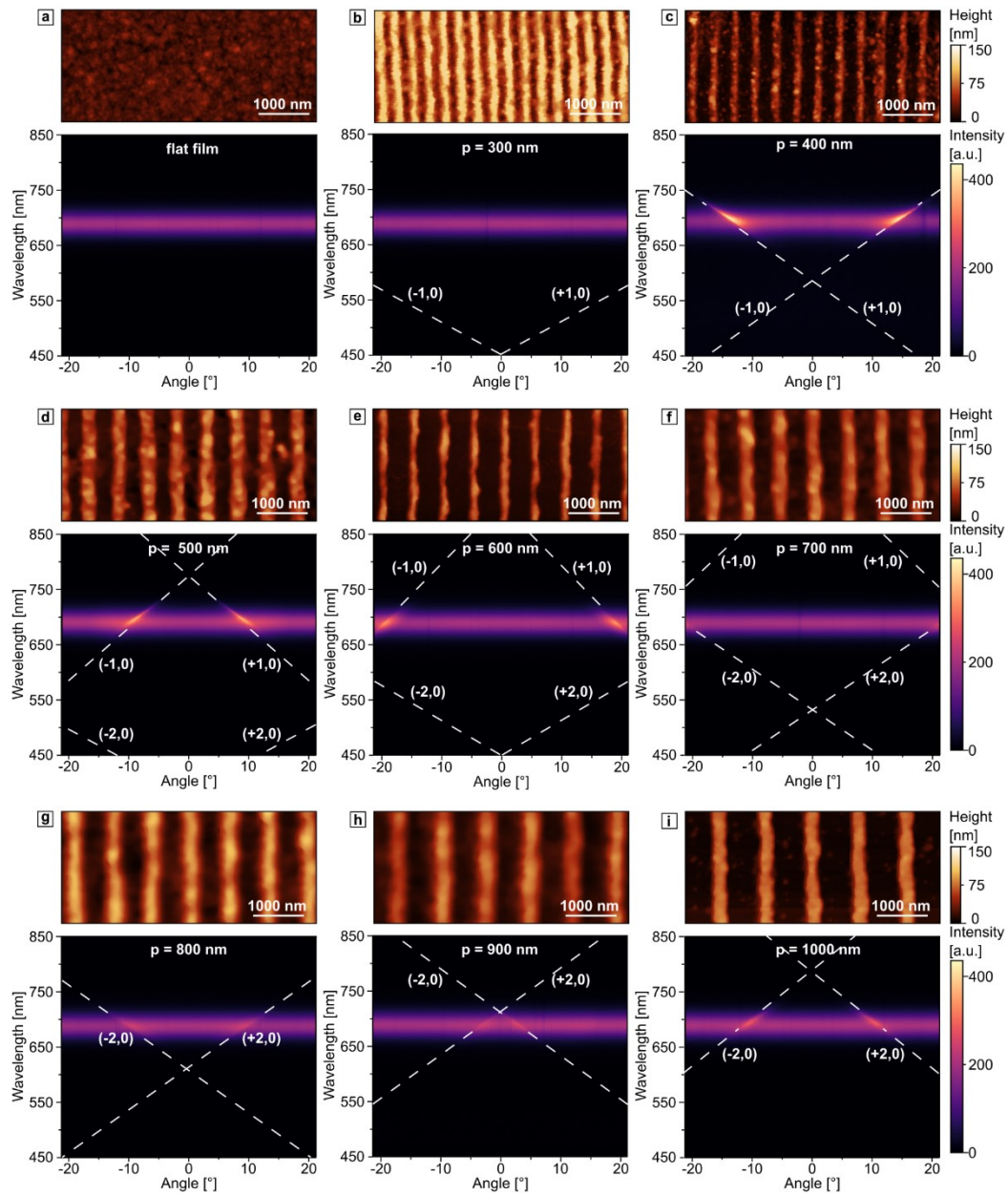
Figure 16: AFM micrographs (top) and dispersion diagrams (bottom) of the (a) flat film of perovskite nanocrystals and 1D gratings with periodicities 300-1000 nm (b-i) under 405 nm laser excitation. The RA of 1st and 2nd orders are marked with white dashed lines.

Thus, by adjusting the periodicity of the 1D grating, one can attain the amplification of the light, emitted by a patterned perovskite structure, at the angle of choice and promote the directionality of the otherwise omnidirectional PL.

4.4. Amplified photoluminescence at high symmetry point

Once the center of the Brillouin zone (high-symmetry Γ-point) coincides with the emission maximum, a strong spatial confinement creates a standing wave pattern (as shown in Figure 14e), perpendicular to the grating, and the emission is amplified (see Figure 17). To fabricate such matching metasurface, we applied the following procedure: first, we considered the wavelength span of 670 nm to 708 nm that corresponds to FWHM of bulk perovskites, second, the desired periodicity span was inferred: between 432 nm and 457 nm ($n_{sup/sub} = 1.55$). In contrast to previous chapter sections, this particular metasurface was manufactured from a colloidal solution with a concentration of ~50 mg/mL, creating a structure with a thin layer under the grating. Here, we take the advantage of the flexibility of our template-assisted self-assembly method and extend theoretical consideration to the guided-mode theory. The fabricated 1D grating featured a periodicity of 450 nm and its optical properties were accessed with the help of angle- and polarization-resolved PL spectroscopy. Under the TM- and TE-polarizations, characteristic 1st order RAs were observed (Figure 17a,b).
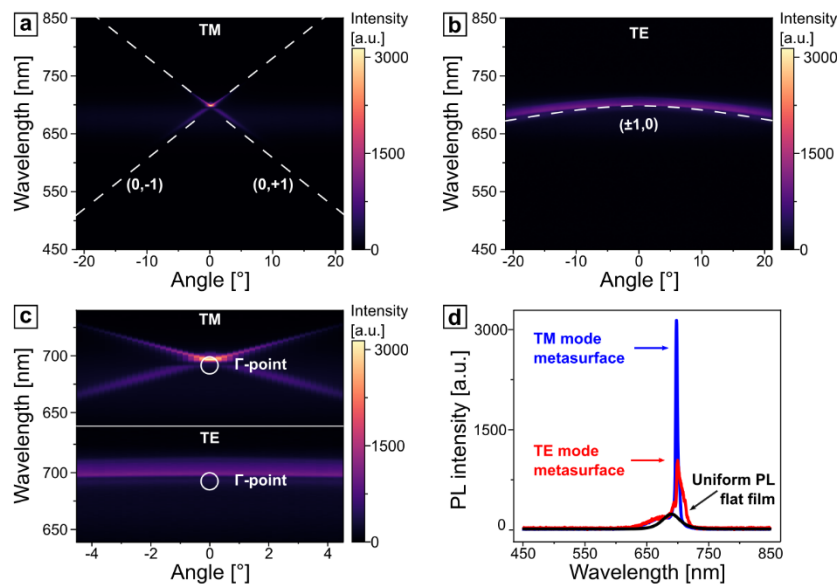
Figure 17: Dispersion diagrams of the structured film, imprinted from the colloidal perovskite solution, under (a) TM- and (b) TE-polarized excitation. The positions of RA for the 1st orders are marked with white dashed lines. (d) Selected PL spectra at 0° for a flat and structured film under TE and TM-polarized excitations.

As anticipated, the photon counts in the normal direction under both excitation polarizations exceeded by far the omnidirectional emission from a flat film (Figure 17c). The amplification of the emission is characterized by a decrease in spectral width

(FWHM) and an increase in photon counts. The quality factor (Q) is defined by the quotient of peak position and spectral width. Compared to a reference layer, we observe an increase of the Q factor by a factor of 10 and 3 for the TM and TE modes, respectively (see Table 2 and Appendix 8.2.4). The number of emitted photons also increased by a factor of 13 and 4, respectively, being, to the best of our knowledge, the highest amplification factor for the perovskite-based metasurfaces, imprinted on a large scale in the ambient conditions (a comparative summary can be found in the Appendix 8.2.5). The lower amplification factor of the TE-polarized mode is caused by its weaker spatial confinement, owing to a broad overlap of the mode with the emission band and not just at the Γ-point, as for the TM-polarized mode. As it has been already extensively discussed elsewhere, the origins of the overall multifold PL amplification are the increase in absorption, strong electromagnetic field confinement that enhances the rate of emission, and improved outcoupling from a structured surface.[145,285]

Table 2: Comparative spectral characterization of the amplification of the emission from the metasurface under TM- and TE-polarizations and PL of the flat film.

	TM-mode	TE-mode	Uniform PL
Peak position	698 nm	702 nm	689 nm
FWHM	4 nm	12 nm	38 nm
Q	175	59	18
Amplification factor	12.9	4.3	-

4.5. Influence and benefit of a waveguide-like layer for light amplification

Our soft lithographic self-assembly method enables producing defined thin layers below the grating that, depending on the thickness, can be exploited either as an additional photon source or as a waveguide under TE polarization, taking the advantage of a large angular overlap with the emission. Notably, the change in the thickness of the underlying film influences the effective refractive index of the surroundings and, therefore, the exact match of the high-symmetry point with the emission band. From the Figure 17d and detailed peak analysis in Table 2, a redshift

of the TE mode with respect to the TM mode could be observed, featuring also a broader, and a rather asymmetric peak shape, thereby indicating the presence of such a layer (a detailed peak fitting procedure, based on non-linear least-squares minimization is described in Appendix 8.2.5).

According to the guided-mode theory, the considered structure can be approximated with a 1D slab waveguide with the effective refractive index ranging from the refractive index of the superstrate $n_{sup} = 1.55$ and the refractive index of perovskites $n_{WG} = 2.04$ that constitute the waveguide-like layer.[286] Since the considered structure represents a typical 2nd order distributed feedback configuration, where the guided mode is scattered out in the direction perpendicular to the plane of the waveguide by the periodic corrugation of the 1D grating residing on top of it, the effective refractive index of the guiding medium n_{eff} can be approximated from the Bragg condition:

$$\lambda_{Bragg} = p \cdot n_{eff} \tag{3}$$

where λ_{Bragg} is the so-called Bragg wavelength and is determined from the RA peak in the emission spectrum, and p is the periodicity of the grating. Thus, for the particularly considered case, n_{eff} stands at 1.56.

Such guided modes are of particular interest for non-linear optical resonators and are extremely sensitive to the thickness of the waveguide layer. To illustrate this, the dispersion diagrams were recorded at various positions within the sample, where the thickness of the underlying layer was assumed to be different (Figure 18). By fitting the observed TE-modes to the RA of the 1st order, one can derive the n_{eff} for each particular case from the Bragg condition, and, consequently, estimate the thickness of the waveguide layer h as:

$$h = \lambda \frac{arctg\left[\kappa(\delta + \gamma) \Big/ \kappa^2 - \delta\gamma \right]}{2\pi\kappa} \tag{4}$$

where λ is the emission wavelength of bulk perovskites (689 nm), $\kappa = \sqrt{n_{wg}^2 - n_{eff}^2}$,

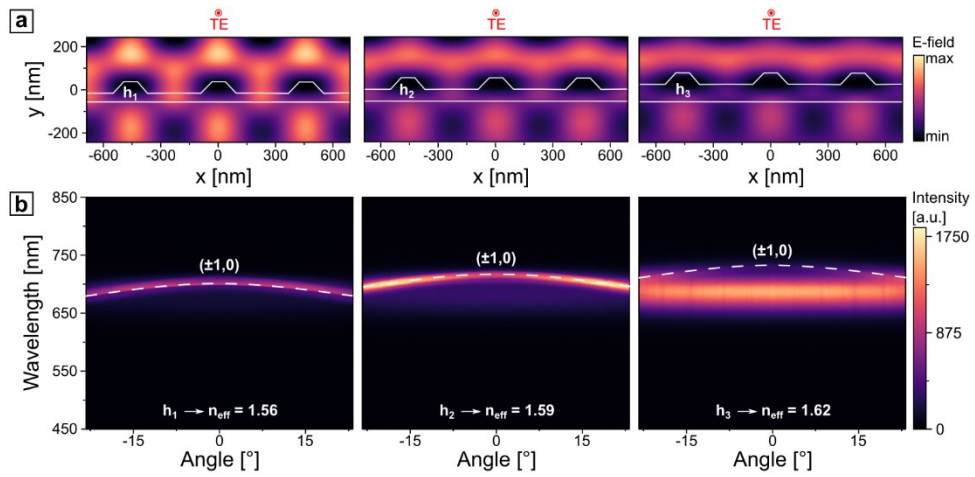$\delta = \sqrt{n_{eff}^2 - n_{sup}^2}$, and $\gamma = \sqrt{n_{eff}^2 - n_{sub}^2}$.[287]

Figure 18: (a) Electric E-field distribution in three metasurfaces ($p = 450\,nm$) with varied thickness of the waveguide-like layer under normal TE-polarized incidence of a plane-wave light source, centered at the RA peak in the emission spectrum. (b) Corresponding dispersion diagrams. The positions of RA for the 1st order corresponding to the different n_{eff} are marked with white dashed lines.

The increasing thickness led to higher values of the n_{eff} that caused a redshift of the TE-polarized guided mode. When it spectrally matched the emission, strong electromagnetic near-field enhancement (Figure 18a) promoted outcoupling in the normal direction, whereas the redshifted modes overlapped only at higher angles, which was also reflected by a less pronounced field enhancement at 0° for such structures (Figure 18b). On the contrary, the overall PL signal was higher due to the larger amount of bulk material. A systematic study at the cross-section of the angle-resolved diagrams at the Γ-point for three different waveguide thicknesses reveals a clear amplification effect for the matching thickness and a less pronounced peak for a mismatched case (Figure 19a). The peak at 689 nm, which corresponds to the bulk emission, appears more dominant for the structures with a thicker waveguide-like layer, as expected.
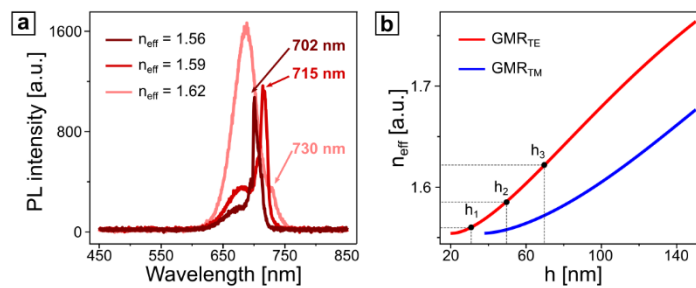

Figure 19: (a) PL intensity spectrum at the Γ-point of selected effective refractive indexes (TE mode). (b) Calculated n_{eff} for guided TE- and TM-modes.

For a continuous range of thickness values, one can calculate the exact n_{eff} for the guided mode resonances (GMR) of both polarizations, which, in turn, gives an insight into a rational reverse design procedure, where the exact parameters of the setup are tuned towards the emission maximum (Figure 19b). In the thinnest waveguide layer with the thickness h1, only TE-polarized guided mode can be excited, contemplating the results, presented in Figure 17, where for the TM-polarization, the bulk emission spectrum is altered only by the presence of RAs, whereas for the TE-polarization, in addition to RAs, guided modes also interacted with the PL of perovskites. The validity of such an approach was also confirmed by measuring the actual layer thicknesses with AFM and comparing them to the values, estimated by Equation 4 and summarized in Table 3 and in Appendix 8.2.6.

Table 3: Calculated n_{eff} for guided TE- and TM-modes. Comparison of the calculated thicknesses h of the waveguide layer with the results obtained from the AFM measurements at the corresponding positions within the sample.

n_{eff}	h	h_{AFM}
1.56	32.0 nm	30.4 nm
1.59	52.7 nm	54.8 nm
1.62	71.0 nm	71.1 nm

In such a way, by adjusting the n_{eff} of the guided modes to the spectral maximum of the emission, one can estimate the appropriate geometry of the waveguide, namely, the thickness of a thin film and periodicity of the grating above, realizing the reverse rational design, and fabricate the desired structure with the help of soft nanoimprint lithography, taking the advantage of its high accuracy and robustness.

Conclusion

In summary, a directional amplification of the photoluminescence from the perovskite-based metasurfaces was demonstrated, providing the important prerequisites for a spatially selective out-coupling of emission for light-emitting diodes, back-light displays, and nanometer-sized distributed feedback lasers. The proposed optimization of the soft nanoimprint lithography technique suggests a cost-efficient approach for manufacturing metasurfaces over large areas in ambient conditions, featuring

periodicities from hundreds of nanometers up to microns, and making it applicable for materials, emitting light in a wide spectral range: from blue to the near-infrared regions,[288,289] or utilizing environmentally friendly quantum dots.[290] Moreover, we implemented a profound polarization- and angle-resolved spectroscopic examination, supported by the numerical simulations, explaining the origins of the observed optical effects, and suggested a strategy for the rational design of the metasurfaces by maximizing the spectral overlap of the emission of perovskite nanocrystals with the diffracted and guided modes.

Experimental Section

Laser interference lithography

To produce a structured film on the glass substrate, LIL was employed. Right before use, microscopy glass slides were divided into individual pieces (2×2 cm) and cleaned with isopropyl alcohol and ultrapure water in a 1:1 ratio by sonication for 20 min at 80 kHz. Positive photoresist (mr-P 1202LIL, micro resist technology GmbH, Germany) diluted with the thinner solution (mat-1050, micro resist technology GmbH, Germany) was spin-coated onto the cleaned and dried under a stream of nitrogen substrate. Optimized spin parameters of 3000 rpm, acceleration of 1000 rpm/s, and total spin time of 33 s produced a thin film of 80 nm thickness, as confirmed by spectroscopic ellipsometry (RC2-DI, J.A. Woollam Co., Inc.) and AFM. The coated substrates were baked at 95 °C for 60 s and further exposed to the 325 nm laser with a dose of 12 mJ/cm^2. The backside of the substrate was covered with black adhesive tape to avoid unnecessary reflections. To develop the exposed photoresist, the sample was submerged into the developer (mr-D 374/S, micro resist technology GmbH, Germany) for 1 min, rinsed with ultrapure water, and dried under a stream of nitrogen.

Soft nanoimprint lithography

Produced by LIL, the structured film of a photoresist was replicated using an elastomeric silicone kit (Sylgard 184, Dow Chemicals, USA) with a ratio of prepolymer and catalyst of 5:1 to create PDMS mold. To further increase the rigidity of the stamp, it was subjected to thermal treatment in an oven at 180°C for 3 hours. Such a process allowed to reduce swelling of the PDMS mold by chloroform from 125% down to 30%. The resulting mold was trimmed and attached to the weight of 100 g. In the next step, 10 µL of the colloidal solution of CsPbI$_3$ perovskite nanocrystals was drop-casted on a cleaned microscopy glass substrate. The weight, together with attached to it PDMS

mold, was immediately placed on the colloidal dispersion to ensure close contact between the mold and the flat surface. The assembly was dried for 1 h at room temperature and relative humidity of 32%. The stamp was then removed by peeling off. For the CFM measurements and angled-resolved spectroscopy of the metasurfaces with varied periodicities, the stock colloidal solution was diluted down to 5 mg/mL with the corresponding solvents. To manufacture the metasurface with a waveguide-like layer, a 50 mg/mL octane-based colloidal solution was used.

Confocal fluorescence microscopy

CFM measurements were acquired with an inverted confocal scanning microscope (MicroTime 200, PicoQuant, Germany) with a 100X air objective (UPLFLN, numerical aperture (NA) 0.9, Olympus, Japan). For excitation, a picosecond pulsed TM-polarized laser diode source (LDH-D-C-405, PicoQuant, Germany) with a center wavelength of 405 nm and a pulse width of 110 ps, driven at a repetition rate of 0.5 MHz. For fluorescence collection, a dichroic mirror (ZT405-442/510rpc-UF3, Chroma, USA), a long pass filter with a cut-off below 425 nm (FF01-519/LP, Shamrock, USA), and a single photon counting module (SPCM-AQRH, Excelitas, USA) were used. For evaluation, SymphoTime 64 2.3 was used. The fluorescence image scans were recorded at 1 μW excitation power (before the objective) and a dwell time of 2 ms per pixel. The average contrast was calculated as the average deviation of all points of the contrast profile from a mean line over the evaluation length, similarly to the average surface roughness.[291]

Surface characterization

Produced line structures were imaged with AFM. The scanning was performed in the tapping mode with silicon nitride probes (typical resonant frequency in the air: 296 kHz). Amplitude set-point was adjusted within the range of 100-200 mV at the scanning frequency of 0.5-1 Hz.

Ellipsometry

To determine the refractive index of the thin crystalline films of perovskites, spectroscopic ellipsometry was performed in the wavelength range from 193 to 1690 nm (combined Deuterium/Quartz-Tungsten Halogen lamps) using a spectroscopic ellipsometer (RC2-DI, J.A. Woollam Co., Inc.). The data was acquired in a reflection mode at various angles of incidence ranging from 50° to 70° in five-degree steps. To model the refractive index of the substrate, Si with native oxide layer

material data was utilized. To determine the refractive index of $CsPbI_3$ a general oscillator layer model was implemented within the CompleteEASE (Version 5.19) software. All modeling approximation complied with Kramers–Kronig relations and showed a mean square error (MSE) below four.

Angled-resolved photoluminescence spectroscopy

The angle-resolved spectroscopy measurements were performed with a Fourier microscopy setup (NT&C, Germany). The sample is illuminated (illumination spot size ~100 µm) by a continuous-wave polarized laser diode source (LDH-D-C-405, PicoQuant, Germany) with a center wavelength of 405 nm through a bright-field condenser (LWD, NA 0.52, Nikon, Japan). The iris of the light source and aperture of the condenser are fully open to allow illumination at different angles. The back focal plane image (Fourier image) is guided inside the microscope objective (CFI S Plan Fluor ELWD 40X, NA 0.6, Nikon, Japan) into the entrance slit of the spectrometer (IsoPlane 160, Princeton Instruments, USA), opened up to 50 um. The PL spectrum was directly collected, after filtering the excitation signal with the long pass filter with a cut-off below 425 nm (FF01-519/LP, Shamrock, USA). The dispersion relation was acquired by collecting the in-plane component of the wave-vector $k = \frac{2\pi}{\lambda} \sin \theta$, where θ is the angle of incidence/detection and representing the data in a form of dispersion diagrams with the angular dependencies. The intensity of the isotropic part of the collected spectra (taken at the angles away from the RA) was adjusted to the omnidirectional PL from a flat film, manufactured via spin-coating (see Appendix 8.2.2) on a glass substrate.

Finite-difference time-domain simulations

A commercial-grade simulator based on the finite-difference time-domain (FDTD) method was used to perform the calculations (FDTD: 3D electromagnetic simulator).[292] To simulate the optical response, a plane-wave source was used, illuminating the structure at a normal incidence with a polarization angle of 90° or 0° for TE- and TM-polarized light, respectively. The excitation wavelength was selected according to the emission maximum with a pulse length of 25 ps. Perfectly matching layer boundary conditions were used in the Y-direction, and periodic boundary conditions were used along X-axis. The grating lines were represented by trapezoids resembling the experimentally measured grating profiles. To obtain the optical responses of the system, frequency-domain field monitors were used. The dielectric

properties of perovskite nanocrystals were imported from the experimentally measured optical constants. For the best simulation stability, the mesh area was set around the existing structure in all two principal directions with a mesh step size of 5 nm and the auto-shutoff level was set to 10^{-6}. The refractive index of the surrounding was set to 1.55.

5. Non-linear light amplification in quantum-dot-based metasurfaces

This chapter contains unpublished work, contributions to each part are to the date of the submission of the thesis.

Olha Aftenieva[1], Markas Sudzius[2], Anatol Prudnikau[3], Mohammad Adnan[1,4], Swagato Sarkar[1], Vladimir Lesnyak[3], Karl Leo[2,*], Andreas Fery[1,5,*], and Tobias A.F. König[1,6,*]

1. Leibniz-Institute of Polymer Research Dresden e. V., Hohe Straße 6, 01169 Dresden

2. Dresden Integrated Center for Applied Physics and Photonic Materials (IAPP), Technische Universität Dresden, 01069 Dresden, Germany.

3. Physical Chemistry, TU Dresden, Zellescher Weg 19, 01069 Dresden, Germany

4. Physikalisches Institut, WWU Münster, Wilhelm-Klemm-Straße 10, 48149 Münster, Germany

5. Chair for Physical Chemistry of Polymeric Materials, Technical University Dresden, Mommsenstr. 4, D-01062 Dresden, Germany

6. Center for Advancing Electronics Dresden (cfaed), Technische Universität Dresden, 01062 Dresden, Germany

* Corresponding authors: leo@iapp.de, fery@ipfdd.de, koenig@ipfdd.de

Author contribution statement

O.A. performed the template fabrication, nanoimprint soft-lithography, microscopic and spectroscopic characterization, and numerical simulations. A.P. and V.L. synthesized quantum dots, performed their in-sol spectroscopic characterization and transmission electron microscopy imaging. M.A. and S.S. assisted in the concept development and spectroscopic characterization. M.S. and **O.A.** performed the device characterization in the lasing mode. K.L., A.F., and T.A.F.K. supported, supervised, and leaded the concept development, scientific discussions, and manuscript writing. All authors provided critical feedback and helped in the data analysis and writing manuscript.

Introduction

The continuing miniaturization of the on-chip devices requires compact semiconductor light sources that are tunable and can operate at a minimal energy input.[293] Colloidal semiconductor quantum dots (QDs), where the bandgap can be easily adjusted within a broad energy range by changing their size, shape, and material composition, are therefore promising candidates as a gain component in such miniaturized devices.[294] Utilizing colloidal QDs allows for cost-efficient wet-chemical processing and is independent of the limitations of the substrate-preferential growth in conventional semiconductor lasers.[295–297] The high standards in the synthesis of colloidal QDs result in improved photostability and outstanding optical gain, bringing QDs-based lasers closer to practical applications and circuit integration.[298] Moreover, constructing heteronanocrystals and combining several semiconductive materials provides additional flexibility in engineering their physical and chemical properties.[299] In particular, core/shell nanocrystals, comprised of cadmium selenide and zinc cadmium sulfide (CdSe/ZnCdS), feature large exciton volumes and strong quantum confinement that significantly decrease the Auger recombination rate.[300,301] The presence of the ZnCdS shell passivates the surface of the CdSe core, increasing the photoluminescence (PL) quantum yields (PLQY) via suppressed nonradiative exciton recombination, and, at the same time, controls the energy transfer between closely packed QDs, improving the overall device performance.[302]

Up to date, optically pumped lasers, featuring semiconductor colloidal QDs were already successfully realized through various resonator configurations: in Fabry-Perot cavities,[303–305] through a whispering-gallery modes (WGM) in microrings,[306–309] microdisks[310–312] and microspheres,[313–316] in vertical external cavities,[317,318]

distributed feedback (DFB),[319] integrated in photonic crystals[130,320] or combined with plasmonic lattices.[240,321–323] Looking from the fabrication perspective, the earliest works already demonstrated lasing from the so-called 'coffee-rings' of QDs, formed after drop-casting and drying the colloidal solution on a substrate.[324] Such an approach, however, suffers from the size and shape limitations and provides poor positioning accuracy. Thus, high-precision micro- and nanofabrication techniques came into view in recent years. In this regard, the most robust and well-controllable configuration is a DFB resonator that consists of a two-dimensional (2D) planar thin-film waveguide combined with a diffractive structure.[325] The periodicity of the diffractive structure p must obey the Bragg condition: $m \cdot \lambda_{Bragg} = 2 \cdot p \cdot n_{eff}$, where m is the diffraction order, λ_{Bragg} is the so-called Bragg resonant wavelength, and n_{eff} is the effective refractive index of the propagating mode. For the DFB structures, based on the 1st order diffraction, where m is equal to 1, both the optical feedback and the output are provided by the 1st diffracted order, propagating in the plane of the waveguide layer. Even though it is preferable for integrated photonics applications, extracting light from such configurations remains challenging.[326] As an alternative, 2nd diffraction order can be exploited. While it propagates in-plane and provides the feedback, the 1st order propagates perpendicularly to the plane of the grating, enabling the light output. Such structures, even though being impaired by higher lasing thresholds compared to 1st-order gratings, create efficient surface-emitting lasers.[327–330] In this regard, careful design of the resonator geometry plays a crucial role. The effective refractive index n_{eff} depends on the mode profile of the propagating mode and is directly connected to the thickness of the thin-film waveguide under the grating.[287] Thus, to match the Bragg resonant wavelength to the PL of the QDs, the periodicity of grating has to be adjusted to the thickness of the waveguide-like layer and material properties of the QDs. The manufacturing strategies must provide, therefore, sufficient control over both geometrical parameters.

Up to now, most of the QDs-based DFB nanolasers were produced by depositing colloids onto a structured template.[331–343] Being rather straightforward, such an approach relies on elaborated substrate preparation and does not allow for creating multicomponent systems. To circumvent that, various direct micro- and nanopatterning techniques were introduced, such as template stripping,[87] electron-beam lithography (EBL),[344–347] laser ablation,[348] photolithography on the blends of QDs and photosensitive polymer[349,350] or nanoimprinting of the composites of QDs and high-refractive index-matrixes.[351] Still, most of these methods either rely on templates

produced with EBL that highly increase manufacturing costs or require the presence of bulk polymers, impeding the inter-particle coupling and reducing the mode confinement.[344] As an alternative, soft nanoimprint lithography (NIL) based on laser interference lithography (LIL) can be applied to arrange colloidal QDs with the help of structured molds. Such an approach was already successfully employed for perovskite nanocrystals, resulting in uniform metasurfaces over macroscopic areas with the nanometer-resolved diffractive features.[145] The presence of the sub-micron structuring itself induces the amplification of the emitted light, but only carefully matched with the guided modes in the layer underneath can induce lasing.[352,353] Thus, the nanometer-precise thickness of the waveguide layer under the grating requires additional effort. To achieve control down to a monolayer of closely packed colloidal QDs and, at the same time, achieve thickness values, enough to sustain guided modes, Langmuir-Blodget layer-by-layer (LbL) deposition can be applied.[110,354] Other thin film deposition techniques, such as drop-casting,[355] spin-coating,[356] jet spraying[357] or electrophoretic deposition[112] cannot provide sufficient control over the thickness and are accompanied by significant material waste.

In this work, we provide a rational design approach to develop self-assembled colloid-based laser structures, featuring 2nd order DFB resonator. Taking into account the material properties of the gain material, detailed numerical simulations were employed to find the optimal geometrical configuration of the DFB resonator, namely, the periodicity of the diffractive structure, and the thickness of the guided mode layer. The optimized metasurfaces were manufactured with the help of NIL, taking the advantage of submicron resolution for the grating component, and by combining NIL with the Langmuir-Blodgett deposition, achieving additional control over the thickness of the waveguide component. As a result, a non-linear effect of light amplification was observed and the lasing operation was confirmed with the threshold-like behavior of the input-output power characteristics. The suggested approach allows for manufacturing nanolasers in a controlled, cost-efficient way over centimeter-scaled areas bringing such colloidal light-emitting metasurfaces a step closer to integrated optoelectronic device applications.

5.1. Rational design of the colloidal nanolaser

The geometry optimization of the 2nd-order DFB configuration was performed with the help of finite difference time domain (FDTD) analysis. To create a realistic

representation of the gain medium, the dispersive material properties of the CdSe/ZnCdS QDs were implemented into the numerical simulations (Appendix 8.3.1). The Bragg condition was satisfied by tuning the geometrical parameters of the DFB structure, depicted in Figure 20a, namely, its periodicity - p and thickness of the waveguiding layer – h. In such a way, the highest spectral overlap of the guided mode and the PL spectrum of the gain medium was achieved, maintaining its high quality factor (Q ~ 300). Figure 20b shows a transmission spectrum (T) of an exemplary metasurface under the broadband polarized illumination with the electric (E) field vector parallel to the grating lines. It supports a narrow-bandwidth transverse electric (TE) mode, satisfying the Bragg condition and matching the PL maximum of a thin film of CdSe/ZnCdS QDs at 650 nm (Appendix 8.3.1). The necessity of a structured surface over a waveguiding layer is also illustrated through the E-field maps at a resonant wavelength: efficient energy confinement is reflected through the E-field nodes located at the positions of 1D grating lines (Figure 20c). First, a comprehensive parameter sweep was performed to determine the modes with the highest Q factors: in Figure 20d it corresponds to the brightest color. Then, by taking into account the mode wavelength, it was correlated with the emission spectrum, defining the region of interest for the considered geometrical parameters (Figure 20e). Finally, by superimposing the relative spectral position of the mode with its Q factor, the optimal geometrical parameters were identified: $p = 428 - 438 \, \text{nm}$ and $h = 140 \, \text{nm}$, accounting for both: the narrow bandwidth of the guided mode, and its spectral match to the PL spectrum.
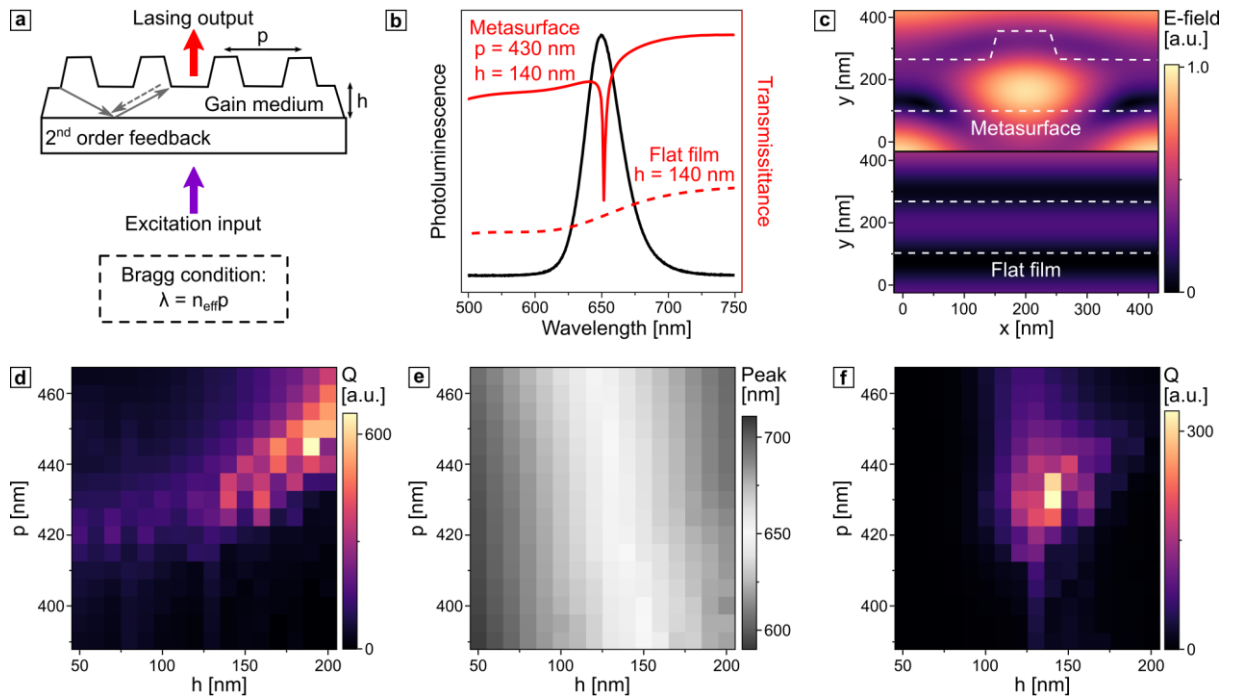
Figure 20: (a) Schematic representation of the resonant setup, fulfilling the 2nd order Bragg condition. (b) Simulated transmission spectra for the device geometry and a flat film with the same layer thickness under broadband TE-polarized excitation. The black line denotes CdSe/ZnCdS PL spectrum. (c) The corresponding E-field profiles under 650 nm TE-polarized resonance condition. (d) Simulated dependence of the Q factor of the guided mode and (e) its spectral position depending on the grating periodicity and the waveguide layer thickness. (f) Cross-correlated parameter sweep map. Parameter optimization aimed at maximized optical quality was performed by mapping the Q factors (d) to the peak position distribution (e), where the 650 nm was taken as a normalizing maximum value.

5.2. Fabrication via soft nanoimprint lithography and Langmuir-Blodgett layer-by-layer deposition

Periodicity and layer thickness are two critical geometrical parameters that determine the optical quality of the structure. The nanoimprint lithography by tailored PDMS molds allows for a robust and reproducible manufacturing of the grating structures with a fixed periodicity, whereas an exact adjustment of the layer thickness can only be obtained by sequential deposition of QD monolayers. Next, we will compare this sophisticated LbL fabrication method with a simple direct printing method. For the latter NIL approach, a highly concentrated (~110 mg/mL) colloidal solution of CdSe/ZnCdS QDs, capped with oleic acid (OA), was confined between the structured PDMS template and a glass substrate, and, upon drying, was assembled into a periodic 1D grating, residing on a waveguide-like layer depicted in Figure 21a. The structured layer was formed over centimeter-scaled areas, as demonstrated in Figure 21b. The surface characterization with scanning electron and atomic force microscopy (SEM and AFM)

techniques revealed a metasurface with a typical 2nd order DFB configuration. As was mentioned in **Chapter 4**, such a process, based on confinement self-assembly, performed in organic solvents and at high concentrations of the nanocrystals, turns out to be challenging in terms of controlling the thickness of the waveguide-like layer under the periodic pattern. Here, the average thickness within the area of interest reached a sub-optimal thickness of ~80 nm, being, nevertheless, still sufficient to sustain a guided mode.
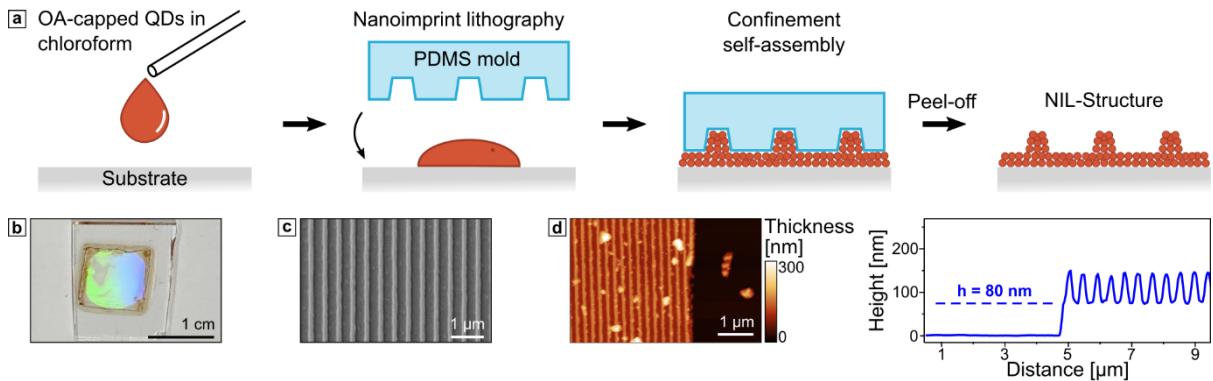

Figure 21: (a) Schematic representation of the NIL technique. (b) Photograph of an imprinted metasurface with the periodicity of the 1D pattern $p = 435\,\text{nm}$. (c) SEM and (d) AFM micrographs of the fabricated structure with the height profile taken across the grating lines.

To gain control over the thickness of the waveguide-like layer and aim for the design, optimized through the numerical simulations, an additional step was added to the fabrication procedure. The colloidal QDs, capped with 2-(2-methoxyethoxy) acetic acid (MEAA) and, therefore, soluble only in chloroform, were deposited with the help of an Langmuir-Blodgett method, depicted in Figure 22a. After transferring the film, formed through drop-casting the colloidal solution on the water-air interface, from water to a glass substrate, its thickness was measured with the help of AFM, revealing a ~7 nm-thick film (Appendix 8.3.1). This value, matching the average diameter of the CdSe/ZnCdS QDs of ~6.5 nm, indicated a single-particle monolayer formation. This procedure was therefore repeated 22 times until the desired thickness was reached. Then, the NIL was applied to the colloidal solution of QDs, capped with OA and dispersed in octane. Since octane is orthogonal to MEAA, the underlying layer of QDs remained intact. It has to be noted that for this NIL step, the colloidal solution was diluted down to 5 mg/mL to avoid residual thin film formation under the 1D grating pattern.
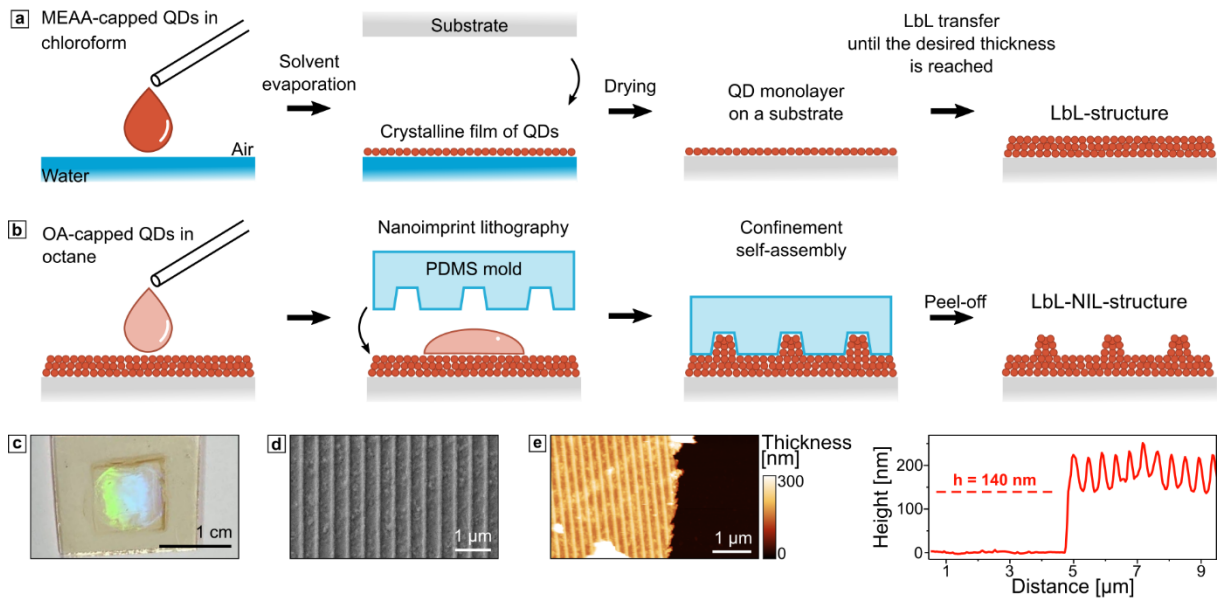
Figure 22: Schematic representation of the (a) LbL and (b) NIL method applied to 110 mg/mL of QDs in chloroform and 5 mg/mL of QDs in octane, respectively. (c) Photograph of an imprinted metasurface with the periodicity of the 1D pattern $p = 430\,\mathrm{nm}$. (d) SEM and (e) AFM micrographs of the fabricated structure with the height profile taken across the grating lines.

The detailed surface characterization of the produced structure (Figure 22d) revealed also more granular morphology of the waveguide layer in comparison to the one, produced in a one-step imprinting process. This can be associated to the LbL transfer process and the ruptures of the monolayer integrity upon drying (Appendix 8.3.1). However, since such additional surface roughness does not exceed the grating features and the periodic pattern remains clearly visible, it did not impede its optical performance.

5.3. Optical characterization and non-linear light amplification behavior

By utilizing the abovementioned techniques, we were able to produce a structure matching all calculated optical parameters and a structure that partially met the resonance conditions. The latter, featuring the 80 nm thickness of the waveguide, was produced by a simple one-step NIL process. Using a two-step procedure that included the LbL deposition based on a Langmuir-Blodgett method, revealed the optimal geometrical configuration with the 140-nm-thick waveguide. The transmission spectra of both structures showed a characteristic waveguiding behavior (Figure 23): under broad-wavelength, TE-polarized illumination clear, narrow-bandwidth dips in intensity at a resonant wavelength around ~650 nm were observed. Figure 23a also depicts the

simulated transmission spectra for both waveguiding structures, demonstrating the spectral match with the experimental data. The apparent discrepancies between simulated and experimental data in the mode bandwidth and the presence of the additional minima in the intensity can be explained by the imperfect positioning of the sample for the transmission spectroscopy measurements, so that the grating lines were not perfectly aligned with the polarization of the incident electromagnetic wave, causing the peak splitting. A more detailed peak analysis can be found in Appendix 8.3.2.

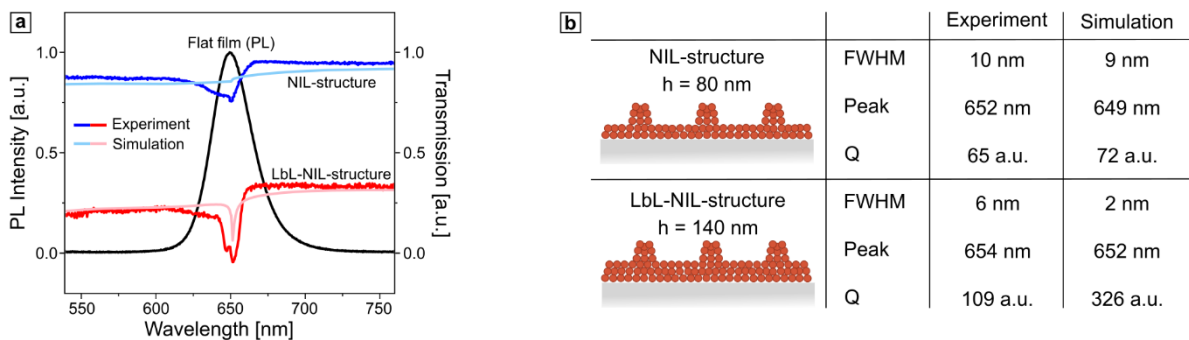| b			Experiment	Simulation
NIL-structure h = 80 nm		FWHM	10 nm	9 nm
		Peak	652 nm	649 nm
		Q	65 a.u.	72 a.u.
LbL-NIL-structure h = 140 nm		FWHM	6 nm	2 nm
		Peak	654 nm	652 nm
		Q	109 a.u.	326 a.u.

Figure 23: (a) Experimental and simulated transmission spectra of the structures with two different thicknesses of the waveguide layer: 80 nm (light blue and blue lines) and 140 nm (light red and red lines). The black line denotes CdSe/ZnCdS PL spectrum. (b) Comparative characteristic of the guided modes.

The presence of such high-quality guided modes allowed for observing the lasing effect. The emission spectra of both structures were recorded under the femtosecond excitation laser with an exponentially increasing input power at room temperature, in an ambient air environment. The 5 kHz pump beam was projected onto the sample with a spot size of 120 µm and the PL spectra were recorded, after filtering the excitation wavelengths. Figure 24a shows the PL spectra at low excitation power, featuring the clear presence of the waveguided modes that split uniform PL peak near the intensity maximum at 650 nm. In Figure 24b the PL spectra in the lasing mode are shown, with the typical linewidth below 1 nm. The input-output curves in Figure 24c demonstrate the characteristic s-shape of the transition from the spontaneous emission regime (left side of the curve) to the stimulated emission process (right side of the curve). The kink in the curve shape is associated with the lasing threshold, indicating the onset of lasing operation mode, and can be clearly identified at 0.6 and 5.5 mJ/cm^2 for both LbL-NIL- and NIL-structures, respectively. Expectedly, lower lasing thresholds feature a smoother transition between the non-lasing and lasing modes, being directly connected to higher spontaneous emission factors.[358] The LbL-NIL-structure, featuring the optimized geometry with a large Q factor of the resonant

mode, showed low threshold pump fluence, which is comparable to the existing 2nd order DFB lasers, with colloidal core/shell Cd-based QDs as a gain medium (for more details, see Appendix 8.3.3). The presence of coherence in the system is further confirmed by drastic spectral narrowing of the mode from 35 to 1 nm around the lasing threshold in the transitional region from spontaneous to stimulated light emission regime.
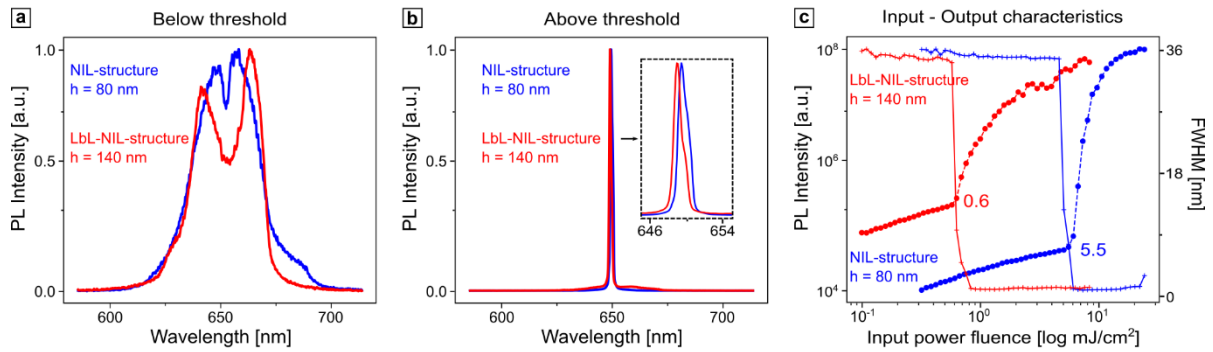

Figure 24: PL spectra of the structure produced via NIL (blue line) and LbL-NIL (red line) methods below (a) and above (b) the lasing threshold. (c) Input-output curve.

The demonstrated lasing behavior showed that by optimizing the geometrical parameters of the DFB resonators, a significant decrease in the lasing threshold can be achieved. Besides controlling the periodicity of the grating and the thickness of the layer under it, one can explore the effect of pitch width and the depth of the grating lines, including the additional degrees of freedom in the rational design. The combination of soft NIL and LbL deposition allows thereafter to manufacture the required structures in a fast and cost-efficient way, taking the advantage of tunability of the pattern geometry through LIL.[359] Utilization of the inorganic, core/shell QDs as building blocks brought an additional benefit to the laser operation in ambient conditions. In contrast to organic-inorganic perovskite-based nanolasers, the proposed configuration demonstrated low-threshold lasing without any need of encapsulation or extreme cooling.[271]

Conclusion

In this work, we showed the non-linear amplification of the emitted light from patterned metasurfaces, featuring the 2nd order DFB resonant structure. By employing the directed assembly approach, highly luminescent core/shell QD building blocks were arranged into 1D gratings residing on a waveguide layer. Soft NIL allowed for submicron resolution of the periodic lattice, while LbL deposition enabled thickness control of the waveguide down to the size of a single QD. The manufactured nanolaser

was realized on a centimeter-scale at a low cost and without any need for a separately manufactured resonant support substrate. Taking the advantage of the purely colloidal approach, we open a possibility for creating an electrically pumped light-emitting system by replacing the utilized gain medium with the suitable colloidal QDs,[97] and offering prospects for different applications in the fields of bioimaging, biomedical sensing, anti-counterfeit applications, or displays.

Experimental Section

Laser interference lithography

To produce a structured film on the glass substrate, LIL was employed. Right before use, microscopy glass slides were divided into individual pieces (2×2 cm) and cleaned with isopropyl alcohol and ultrapure water in a 1:1 ratio by sonication for 20 min at 80 kHz. Positive photoresist (mr-P 1202LIL, micro resist technology GmbH, Germany) diluted with the thinner solution (mat-1050, micro resist technology GmbH, Germany) was spin-coated onto the cleaned and dried under a stream of nitrogen substrate. Optimized spin parameters of 3000 rpm, acceleration of 1000 rpm/s, and total spin time of 33 s produced a thin film of 70 nm thickness, as confirmed by spectroscopic ellipsometry (RC2-DI, J.A. Woollam Co., Inc.). The coated substrates were baked at 95 °C for 60 s and further exposed to the 325 nm laser with a dose of 12 mJ/cm^2. The backside of the substrate was covered with black adhesive tape to avoid unnecessary reflections. To develop the exposed photoresist, the sample was submerged into the developer (mr-D 374/S, micro resist technology GmbH, Germany) for 2 min, rinsed with ultrapure water, and dried under a stream of nitrogen.

Layer-by-layer deposition

The stock solution of colloidal QD, dispersed in chloroform, were diluted down to ~4 mg/mL. A volume of ~10 uL was then drop-casted onto a liquid-air interface, where the 'liquid' phase comprised of 8.33 µM aqueous solution of sodium dodecyl sulfate (SDS). The presence of surfactant was used to confine the spread of the drop-casted QDs at the interface. The volumes and concentration values were optimized to achieve formation of a crystalline monolayer. After the evaporation of chloroform, the self-assembled monolayer war transferred to a solid support. For this, the substrate was rendered hydrophobic via gas-phase deposition of trichloro(1H,1H,2H,2H-perfluorooctyl)silane (448931, Sigma-Aldrich) at 60 °C for 3 h. The QDs were then

manually transferred onto the substrate via Langmuir-Blodgett method, by submerging it parallel to the liquid-air interface through the self-assembled layer. Due to the hydrophobic nature of the QDs, they were preferentially deposited from the aqueous environment to the hydrophobic support. For the subsequent layer transfers, the residual water drops were dried under the stream of nitrogen. After the first layer deposition, the surface was readily hydrophobic due to the presence of QDs and did not require any additional modification. The assembly was performed in a dark room under the UV-lamp illumination for a better visualization of the QD layer at the interface.

Soft nanoimprint lithography

Produced by LIL, the structured film of a photoresist was replicated using an elastomeric silicone kit (Sylgard 184, Dow Chemicals, USA) with a ratio of prepolymer and catalyst of 5:1 to create the PDMS mold. To further increase the rigidity of the stamp, it was subjected to thermal treatment in an oven at 180°C for 3 hours. Such a process allowed to reduce swelling of the PDMS mold by chloroform from 125% down to 30%. The resulting mold was trimmed and attached to the weight of 100 g. In the next step, 10 µL of the colloidal solution (CdSe/ZnCdS) was drop-casted on a substrate (cleaned microscopy glass or waveguide-like layer of QDs on glass, pre-assembled with the LbL deposition. The weight, together with attached to it PDMS mold, was placed on the quantum dot dispersion to ensure close contact between the mold and the flat surface. The assembly was dried for 1 hour at room temperature and relative humidity of 32%. The stamp was then removed by peeling off.

Surface characterization

Produced line structures were imaged with AFM. The scanning was performed in the tapping mode with silicon nitride probes (typical resonant frequency in the air: 296 kHz). Amplitude set-point was adjusted within the range of 100-200 mV at the scanning frequency of 0.5-1 Hz. For the SEM, NEON 40 FIB-SEM workstation (Carl Zeiss Microscopy GmbH, Oberkochen, Germany), operating at accelerating voltage (electron high tension) of 1 kV was used.

Ellipsometry

To determine the refractive index of the thin crystalline films of QDs, spectroscopic ellipsometry was performed in the wavelength range from 193 to 1690 nm (combined Deuterium/Quartz-Tungsten Halogen lamps) using a spectroscopic ellipsometer (RC2-DI, J.A. Woollam Co., Inc.). The data was acquired in a reflection mode at various

angles of incidence ranging from 45° to 75° in five-degree steps. To model the refractive index of the substrate, Si with native oxide layer material data was utilized. To determine the refractive index of CdSe/ZnCdS a general oscillator layer model was implemented within the CompleteEASE (Version 5.19) software. All modeling approximation complied with Kramers–Kronig relations and showed a mean square error (MSE) below four.

Finite-difference time-domain simulations

A commercial-grade simulator based on the FDTD method was used to perform the calculations (FDTD: 3D electromagnetic simulator).[292] To simulate the optical response, a plane-wave source was used, illuminating the structure at a normal incidence with a polarization angle of 90° representing the TE-polarized light (in-line with the grating lines). For collecting the transmission, the broadband illumination (400-900 nm) was used. For simulating the E-field distribution, the excitation wavelength was selected according to the emission maximum with a pulse length of 25 ps. Perfectly matching layer boundary conditions were used in the Y-direction, and periodic boundary conditions were used along X-axis. The grating lines were represented by trapezoids resembling the experimentally measured grating profiles. To obtain the optical responses of the system, frequency-domain field monitors were used. The dielectric properties of CdSe/ZnCdS were imported from the experimentally measured optical constants. For the best simulation stability, the mesh area was set around the existing structure in all two principal directions with a mesh step size of 5 nm and the auto-shutoff level was set to 10^{-6}. The refractive index substrate was set to 1.5, while the surrounding refractive index was set to 1.

Transmission spectroscopy

The transmission spectroscopy measurements were performed with a Fourier microscopy setup (NT&C, Germany). The sample was illuminated (illumination spot size ~100 μm) by a tungsten-halogen light source through a bright-field condenser (LWD, numerical aperture (NA) 0.52, Nikon, Japan), avoiding the ambient light. The back focal plane image (Fourier image) was guided inside the microscope objective (CFI S Plan Fluor ELWD 40X, NA 0.6, Nikon, Japan) into the entrance slit of the spectrometer (IsoPlane 160, Princeton Instruments, USA), opened up to 50 um. The transmission spectrum was directly collected at 0° angle of detection and corrected by subtracting the dark current at the detector and normalizing against the reference spectra collected from an empty glass substrate.

Lasing threshold and input-output curve measurement

The samples were excited optically to the absorption of CdSe/ZnCdS by femtosecond laser pulses with a duration of 100 fs and a repetition rate of 5 kHz. The pulses were produced with a Micra femtosecond oscillator and amplified with a regenerative amplifier Legend Elite Duo, both by Coherent. The second harmonic was generated at 400 nm from the output of the RA. The excitation beam was focused by a lens to a spot size of 120 μm in diameter. The emission was collected by a high NA objective lens at the opposite side from excitation and guided into a spectrometer equipped with a cooled charge-coupled device camera.

6. Tunable circular dichroism induced by self-assembled photoluminescent Moiré lattices

This section is based on the peer reviewed open access journal article *Advanced Optical Materials* **2020**, 2001280. This is an open access article published under a Creative Commons Attribution 4.0 International (CC BY 4.0) license, which permits use, distribution and reproduction in any medium, provided the original work is properly cited.

By Olha Aftenieva [1,#], Max Schnepf [1,#], Börge Mehlhorn [1] and Tobias A.F. König [1,2,*]

1. Leibniz-Institute for Polymer Research Dresden, Hohe Straße 6, 01169 Dresden

2. Center for Advancing Electronics Dresden (cfaed), Technische Universität Dresden, 01062 Dresden, Germany

[#]Equal contribution: O.A., M.S.

*Corresponding e-mail: könig@ipfdd.de

Author contribution statement

O.A. and M.S. contributed equally to the work. **O.A.** performed template fabrication and lift-off process. **O.A.**, M.S. and B.M. performed soft-lithography-based confinement self-assembly and confocal fluorescence microscopy imaging. **O.A.**

Introduction

A Moiré effect occurs when repetitive structures such as gratings are superimposed against each other with a relative difference in lattice constant or in-plane rotation angle.[360] By tuning these parameters, Moiré pattern can be accurately controlled and applied for measuring strain deformation,[361] precise alignment in optical security labels,[362] and biosensors.[363] In addition, configurations with the Moiré effect show more optical features than their primary components.[364] Formation of Moiré pattern can be realized through interference,[364,365] block copolymer,[366] nanosphere,[367] or imprinting lithography.[368] These approaches result in large-area quasicrystal patterns, being, however, permanently inscribed in the medium and, thus, hindering the tunability of optical properties. An alternative strategy implies separate manufacturing of periodic structural components and generating a Moiré interference by bringing them into close contact. The simplest periodic structures to consider are one-dimensional (1D) gratings that, when stacked at various angles, result in 2.5D chiral metasurface. Such structures demonstrate strong circular dichroism (CD). With crossed gold gratings, one could achieve CD, characterized through the degree of polarization, of 0.3.[70] When using aluminum helically stacked lattices, the abovementioned effect was 2.5 times stronger and observed over the entire visible and near-infrared wavelengths range.[71] By taking advantage of the surface lattice resonance from the metal nanoparticle arrangements, one can reach comparable effect strength.[66] Such metal-based chiral structures, however, suffer from the non-radiative Ohmic losses that limits their usage to the absorption-based applications.

To exploit the chiroptical effect for the light generation, one has to introduce a light-emitting component. Colloidal quantum dots (QDs) appear to be the optimal candidates, featuring broadband absorption, size- and material-controllable emission wavelength, high quantum yields, and photostability.[83,369] To directly induce the circularly polarized photoluminescence, two principal strategies have been suggested: through connecting chiral ligands to the QDs surface[370] or by combining achiral QDs with chiral plasmonic metasurfaces. The first approach resulted in relatively weak

induced chirality and required elaborate surface modifications. On the contrary, combination with chiral metal nanostructures enabled strong circularly polarized emission. For this, the CD response of the template should match either absorption[371] or emission bands of the QDs.[17]

The necessity to have a chiral plasmonic template with inherent energy losses and quenching effects hinders such light-emitting metasurfaces from practical applications. On the contrary, assembling emitters into chiral structures directly enables loss-free polarized photoluminescence. On this notion, special care must be taken about the optical performance. To avoid significant quenching of the photoluminescence for closely packed QDs [373], one can utilize the core-shell QDs, where the distance between the emitting centers is defined by the shell thickness.[374] Moreover, to match multiple virtual hybridization states created by the Moiré pattern and observe a chiral response over a large wavelength span, it might be beneficial to employ emitters with broadband absorption, as well as emission, spectra.[87,371]

Until now, production of periodic light-emitting structures with the features on the scale of the emitter wavelength remained to be challenging, and the direct arrangement of emitters into chiral structures providing a pure circular-polarized-light-emitting device has not been demonstrated. Template stripping [87,375] and electron beam lithography [345] techniques potentially allow for high-resolution patterning, being, however, cost-inefficient and not applicable for large-area manufacturing. To produce patterned emitter-based structures on a centimeter-scale area, simple casting, Langmuir–Blodgett deposition, dip coating, inkjet printing, or photopatterning could be applied. However, these methods mostly result in films without sufficient uniformity and control over the film thickness.[376–378] As an alternative, one can employ contact printing techniques[152,379–381] to create periodic micron-sized structures on a centimeter scale through the confinement self-assembly of nanocrystals just by using a structured stamp. However, due to the generally poor cohesion of quantum emitters and the strong influence of artifacts on the wetting behavior, it remains a difficult task to assemble quantum emitters into a sub-micron grating.

To overcome this challenge, one has to adjust the surface properties of the stamping template, and utilize particles with a size much smaller than the gap. The latter is easily fulfilled for the QDs that are few nanometers in diameter. To allow the water-based colloidal solution to fill the gaps in the structured template, the contact angle must be sufficiently decreased through the surface activation. The stability of colloidal QDs in

an aqueous solution is ensured, in this case, by thioglycolic acid (TGA) through the electrostatic repulsion of carboxylic groups,[382] that additionally promote stronger adhesion of QDs to the substrate than to the stamping template. Then, during drying, van-der-Waals forces cause a strong cohesion between the particles. Overall, the abovementioned printing technique creates emitter-based sub-micron metasurfaces that can be utilized for multiple photonic applications, including band edge and near-infrared lasing,[152,375] photodetection,[379,380] fabrication of LEDs,[383] security labels,[384] parity-time symmetric gain-loss systems, where the high contrast is required together with an ability to change the phase shift of the contributing components, or for generating a polarized light source.

In this work, the optical effects induced by superposition of two 1D gratings, comprised of photoluminescent semiconductor material or a metal, were explored. Their fabrication with a low-effort lithography-based approach gives a competitive advantage among other high-resolution techniques. Both gratings were produced on a centimeter-scale area: the metal component was introduced on a rigid substrate through the metal vapor deposition, and the emitter-based grating was printed by the soft-lithographic method on a flexible substrate, to ensure close contact between the structures. A simple stacking and relative in-plane twisting of those 1D grids enabled the robust appearance of fluorescent Moiré patterns that demonstrated chiral photoluminescence without any additional chiral building blocks. This suggests utilizing such structures as functional chiroptical sensors, or in optoelectronic devices, by creating a tunable optical bandgap.

6.1. Visual representation of the Moiré effect

A typical representation of the Moiré effect is illustrated in Figure 25. The supra-periodic pattern is formed by superimposing two 1D gratings (Grating 1 and 2) with the same lattice constant at various relative in-plane rotation angles. Its appearance is then solely defined by geometric parameters of the lattices and relative rotation and can be analytically predicted with high precision (see Appendix 8.4.1). In its turn, the visibility of the produced supra-periodic pattern depends on the amplitude of the lateral contrast, i.e. the difference between the maximum and minimum luminance of a selected profile. For a complete lateral characterization, one can measure the contrast amplitude along two principal directions: M-axis follows one of the gratings, crossing the Moiré pattern that appears as a set of interference lines, and R-axis that serves as

a reference and goes parallel to the lines of a Moiré pattern. Thus, contrast along M-axis C_M reflects a profile, governed by the Moiré pattern, while C_R shows the contrast profile, dictated by one of the gratings. The Moiré pattern itself is defined through the relative rotation of the two stacked lattices, thus, C_M can be laterally tuned across the large range of distances, since the positions of maximum and minimum intensities are shifted through the changing angle. At the same time, the contrast along the R-direction, being independent of the Moiré pattern, is fixed by the lattice constant.
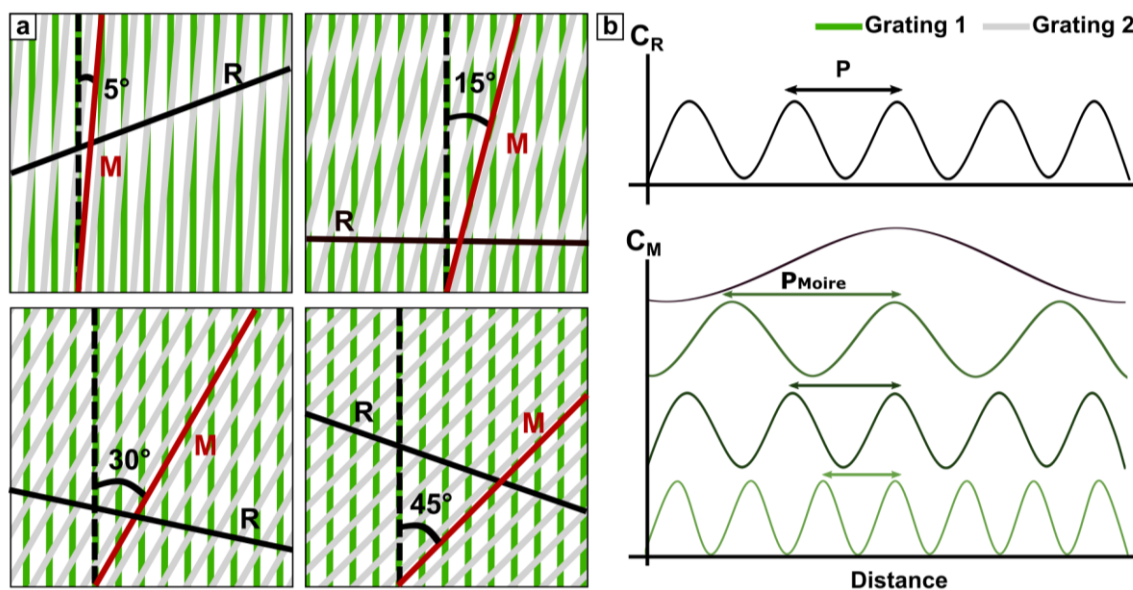

Figure 25: Exemplary interference patterns and their characterization. (a) Moiré patterns generated by two superimposed gratings (shown with green and grey lines) with equal periodicities at various orientation angles. (b) Contrast profile plots along principal directions (M - crossing the Moiré interference lines and R - parallel to them).

6.2. Fabrication via laser interference lithography and template-assisted self-assembly

In further experiments, Grating 1 and Grating 2, having the same lattice constant of ~800 nm, are systematically replaced by one of these materials: gold (Au) or emitting self-assembled semiconductor nanocrystals. To ensure the practical applicability of such gratings, one has to make sure that manufacturing includes low-cost and reproducible techniques. Therefore, laser interference lithography (LIL) and wet-chemical processing were employed. Au periodic structures were obtained after subsequent sputtering and in-solution lift-off process, as described in Figure 26a. Fabrication of the emitter gratings involved polydimethylsiloxane (PDMS) soft molding process, represented in Figure 26b. A defined volume of nanocrystals was then drop-casted on the flexible substrate, followed by applying the PDMS master template and

drying under pressure (flexibility of at least one of the substrates is required to bring the gratings in close contact with each other and ensure the near-field energy transfer). The periodic structure was exposed after peeling-off the PDMS master. Both gratings were characterized by atomic force microscopy (AFM), revealing periodic structures with uniform geometric parameters over a large scale (see Figure 26c).
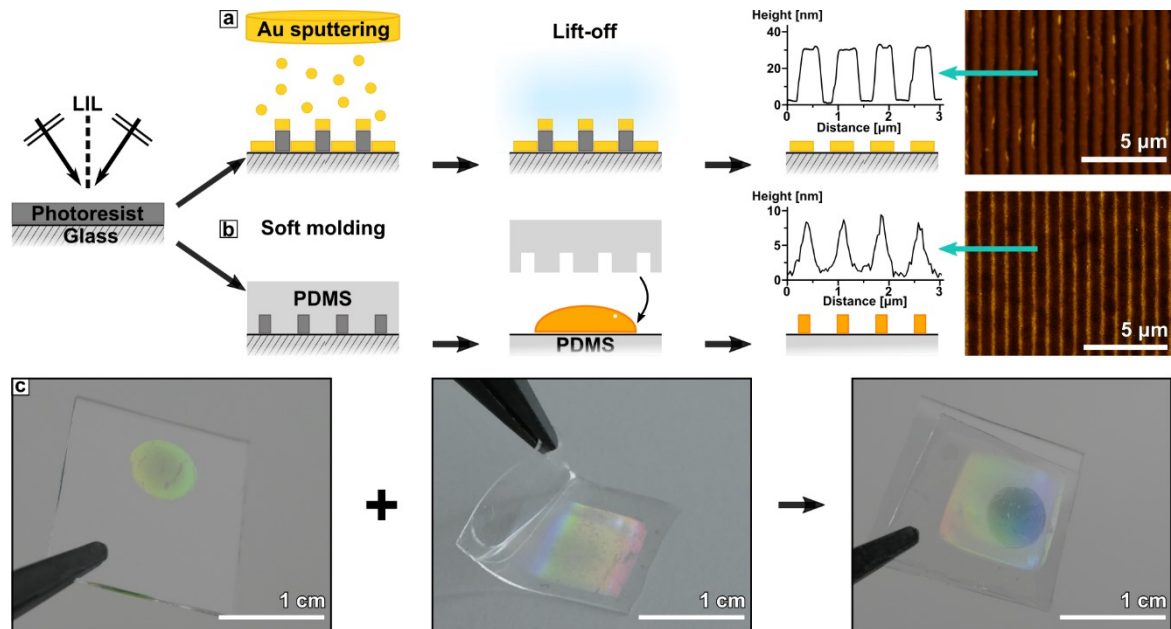

Figure 26: (a) Metal grating, fabricated by laser interference lithography (LIL), sputtering of Au, and lift-off process. (b) Emitter grating, produced by confinement self-assembly from core-shell quantum emitters with a soft polymer PDMS template. Geometric parameters, determined by AFM: (a) periodicity of 790 nm and height of 30 nm, (b) periodicity of 820 nm and height of 10 nm. (c) Photographs of the metal grating on the glass substrate, superimposed with emitter grating on flexible PDMS substrate.

6.3. High contrast and tunability of the Moiré patterns

Moiré interference effects were first compared between various combinations of periodic structures at the same angle (see Figure 27): emitter and emitter - E&E, metal and metal - M&M, and metal and emitter - M&E. A single, emitter-only grating was used as a reference. The photoluminescent signal was captured by confocal fluorescent microscopy (CFM) imaging under the excitation of 405 nm laser that selectively excited the quantum emitters. In such a configuration, metal grating appeared as dark background, since the reflected excitation light was filtered out and the fluorescence of bulk Au was not detected. To observe the interference of M&M structure, 640 nm laser was used, and the reflected light was collected by the CFM setup. According to the abovementioned formalism of principal axes, to characterize the lateral contrast in various grating combinations, the axes were assigned in the following way: M-axis

always followed the line of assembled QDs in E&E, M&E, and emitter-only gratings, or one of the Au lines in the M&M combination, while R-axis was parallel to the lines of the Moiré pattern. It is important to note that R and M are not perpendicular to each other and their orientation depends on the relative rotation of the gratings.
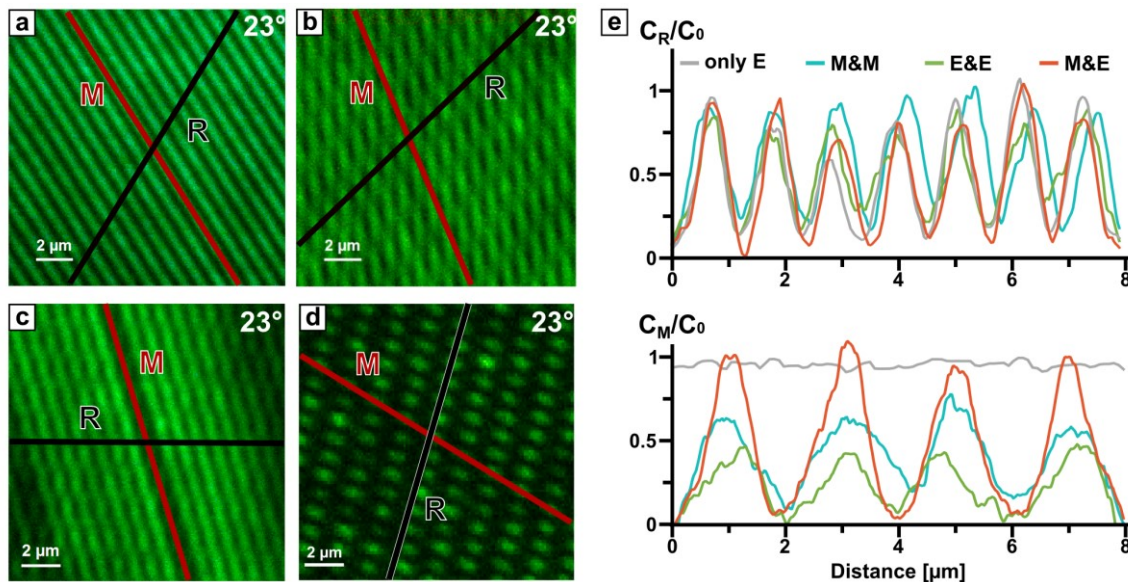

Figure 27: Various combinations of metal and emitter gratings with a fixed lattice constant (~800 nm) and relative rotation angle (~23°). (a) CFM images of an emitter grating only. The drawn R- and M-axes (shown in black and red lines) indicate principal directions to characterize the contrast amplitude. CFM images of superimposed metal (b), emitter (c) gratings as well as (d) a combination of both. (e) The intensity profiles along R and M directions for the various cases. The intensity was shifted to 0 for clarity and normalized to the reference value C_0- intensity signal, recorded from the emitter grating only.

To characterize the lateral contrast along R and M directions, the following notions were used: single emitter grating was considered as a contrast reference with a maximum intensity value C_0 measured along the M-axis and corrected to the background signal. The contrast C was calculated as the difference between the maximum and minimum value, normalized to C_0 for both directions. The contrast ratio C_M for the emitter grating only was then considered as an error rate of 11% for all the following measurements. Along the R-axis, parallel to the Moiré lines, the contrast was comparable within all 4 samples, resembling the contrast produced by one of the gratings. Following the intensity profile, produced by the Moiré interference, the contrast of ~70% can be achieved for combined identical gratings. However, when stacking absorbing and emitting counterparts, the contrast can be improved by 30% and is comparable to the contrast of only a single emitter grid (exact C_M and C_R values are given in Appendix 8.4.2). This combination allows for high-contrast patterns, where

the positions of high/low intensity are not strictly fixed and can be tuned through the in-plane twisting of the superimposed substrates, as demonstrated in Figure 28.
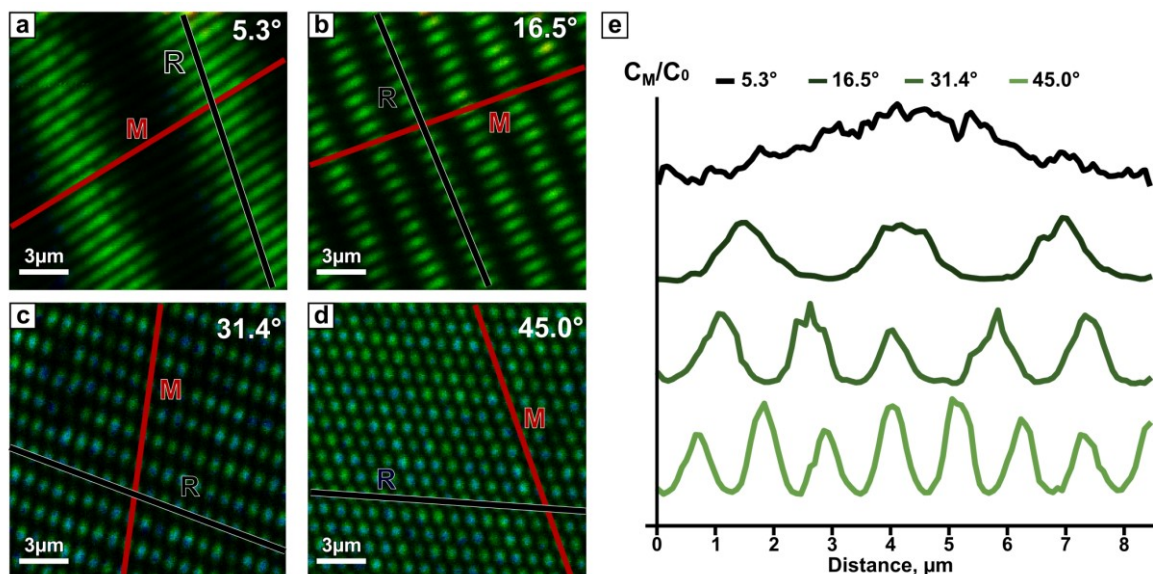

Figure 28: Interference pattern of a superimposed metal and emitter lattices at different angles of orientation. (a) CFM image at 3.2°, 16.5°, 31.4°, and 45.0° relative rotation angles as well as (b) the corresponding intensity profiles of the Moiré interference pattern.

Such a simple approach enables obtaining varied intensity profiles of different periodicities within one structure (as shown in Figure 28b). Those patterns are defined by the Moiré supra-periodicity and can be as twice as small, or far higher than the initial lattice constant (see Appendix 8.4.1), with the lateral resolution limit reaching $\frac{\lambda}{\pi NA} \sim 143$ nm, where $\lambda = 405\ nm$ − central wavelength of the laser and numerical aperture $NA = 0.9$.

Besides lateral contrast, one can consider it in a vertical direction by changing the spacing between metal and emitter gratings. For sensor applications these distance investigations are important, because the analyte layer can be placed at the most sensitive point between the grids. Thus, for a proof of concept, a transparent polymer film of polymethyl-methacrylate (PMMA) spacer was introduced in between the two gratings (Figure 29).
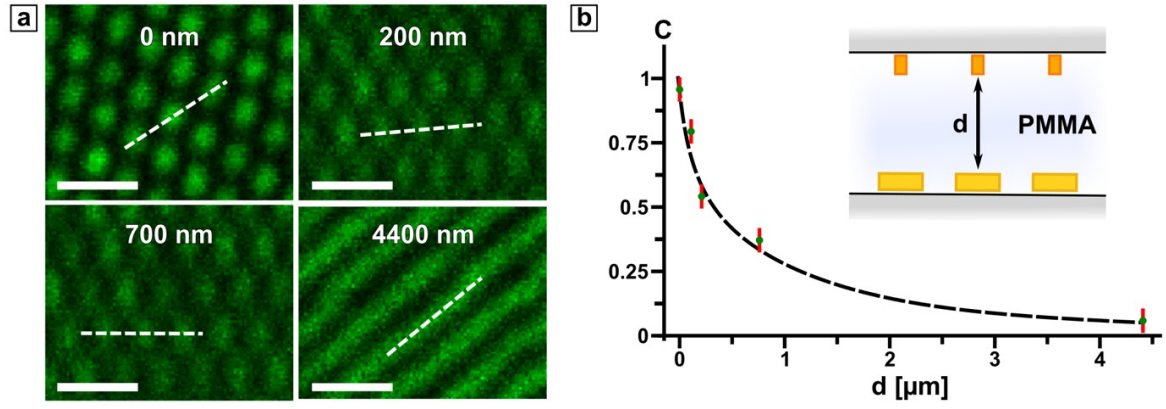
Figure 29: (a) Implementation of a PMMA spacer material to study the interaction depth between the metal and emitter lattice. The CFM images show the Moiré inference at spacer distances between 100 nm and 4.4 μm. The contrast C was measured along the white dotted line that follows one of the emitter lines and crosses the lines of the Moiré pattern, if visible. The scale bar is 2 μm. (b) The contrast with respect to the spacer thickness. The error is indicated by the red vertical line.

The contrast was maintained in the range of several hundreds of nanometers that is within at least half of the vertical resolution of the objective, estimated as $\frac{2n\lambda}{NA^2}{\sim}1490$ nm, with the refractive index n of PMMA being 1.49. It was sufficient to observe the Moiré pattern, even with more than a two-fold decrease in contrast. The change of contrast amplitude with the inter-lattice distance (shown in Figure 29b) features power-law decay and supports the near-field nature of the observed interaction. Moreover, the contrast quality was maintained even on the flexible substrate that was constantly prone to mechanical deformations over five months of sample utilization.

6.4. Circular dichroism in photoluminescence

The considered configuration of two 1D gratings with a possibility of an arbitrary in-plane rotation also suggests its benefit for creating an emitter-based circular polarizer, since superposition of similar, but only metal-based structures demonstrated strong CD effect.[71] In our case, however, it implies the transformation of linearly polarized excitation light to the circularly polarized emission. This chiroptical effect was measured and quantitatively evaluated as a degree of polarization at the maximum emission wavelength and calculated according to the following formula: $g_{PL} = \frac{2(I_{RCP}-I_{LCP})}{(I_{RCP}+I_{LCP})}$, where $I_{RCP/LCP}$ are the intensities of the detected right (RCP) or left circularly polarized (LCP) emission light respectively. Spectral analysis of the output light, presented in Appendix 8.4.3, revealed the absence of a spectral shift in the emission of stacked M&E and E&E which allowed to consider the intensity values at

the same wavelength of 608 nm. The experimental setup is shown in Figure 30a. The sample was excited at a normal incidence with a continuous TM-polarized laser at 405 nm and the photoluminescence signal was collected in the forward direction after passing through a zero-order quarter-wave plate and a linear polarizer to dissect right and left polarization. The RCP and LCP emission intensities of two types of hybrid structures: M&E and E&E were measured for several in-plane rotation angles, summarized in Figure 30b.
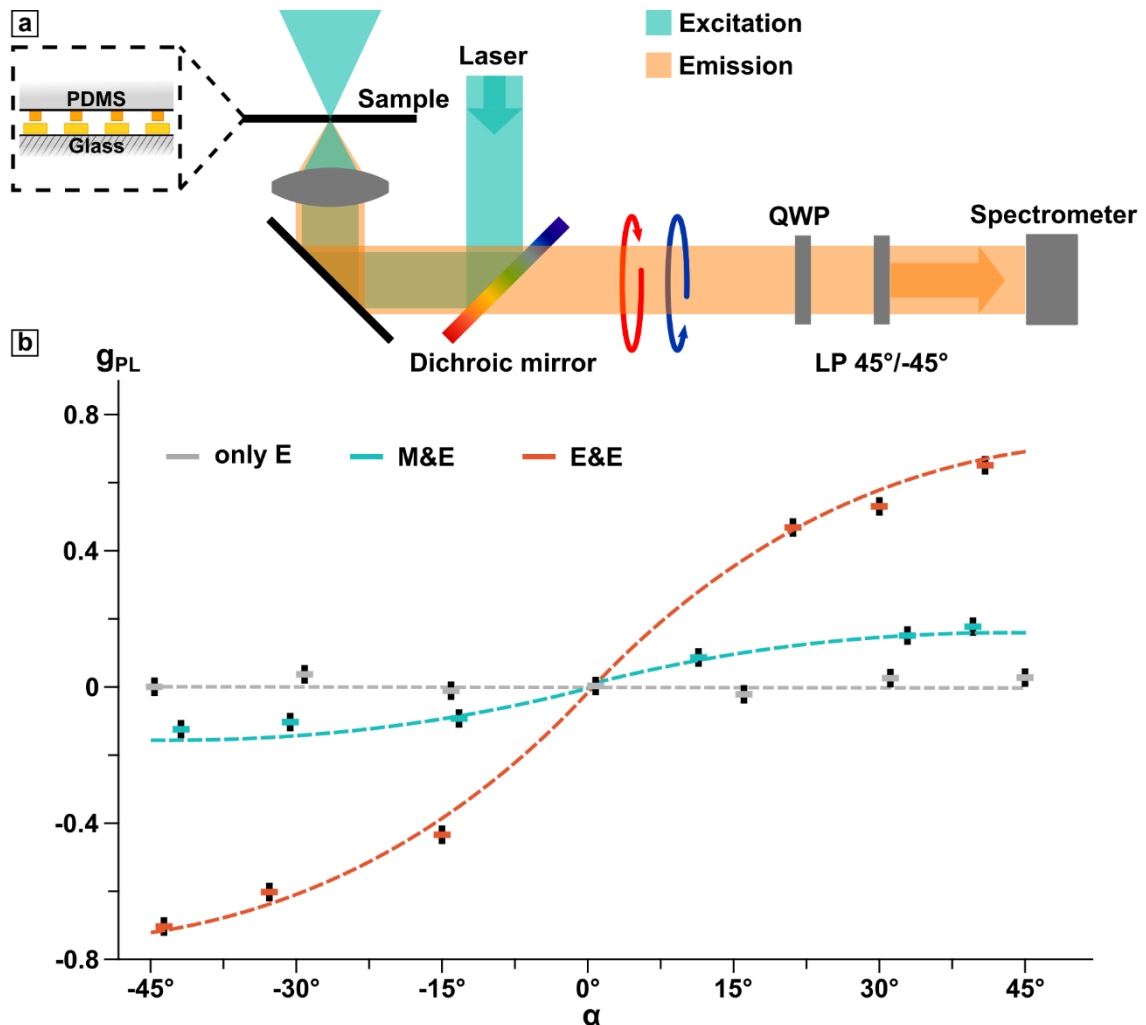

Figure 30: Measurement of polarized photoluminescence. a) Experimental setup shows the laser excitation (polarization of the beam is shown with a blue arrow, direction of propagation - with pink) and analysis of the reflected light using a $\lambda/4$ wave plate (QWP) and linear polarizer (LP) that is oriented at 45° or -45° to the fast axis of the QWP. b) The g_{PL}-factor at 608 nm with respect to various orientation angles for superimposed gratings. The error rate of 0.008, marked as a vertical black line, was measured as the degree of polarization of only the emitter grating.

When the emitter lines were combined with the metal grating, the maximum g_{PL} value of 0.19 was observed for 45° angle of relative rotation between the crossed lines, together with the comparable negative value -0.16 for -45°. Interestingly, the intrinsic

78

chirality of the structure, where two emitter gratings are superimposed, is not only able to give rise of circularly polarized emission but also demonstrates remarkably high g_{PL}-factors: 0.64 and -0.72 for the left and right rotation of the stacked gratings respectively. The absence of perfect symmetry for the opposite rotations was possibly caused by slightly mismatched angles and geometrical variations within the gratings. The obtained values are comparable with the ones reported so far in the literature, where achiral QDs were combined with the chiral metal template: 0.34 for the ion-beam patterned gold film [371] and 0.95 when less lossy silver nanoarcs were employed.[372] The suggested structure is, on the other hand, completely loss-free and features low-effort self-assembly of colloidal QDs that can be used as a compact circular polarizer for on-chip photonic circuits and benefit as a component for an optical isolator.

To get further insight into the origin of the chiral response for those stacked structures, finite-difference time-domain (FDTD) simulations were performed (described in detail in Appendix 8.4.4). In contrast to the experimental setup, where the structures were illuminated by the linearly polarized light and the chiral emission was detected, here both configurations were studied under the circularly polarized light, differentiating between the absorption ($A_{RCP/LCP}$) of RCP or LCP light. The degree of polarization was then estimated as $g_A = \frac{2(A_{RCP}-A_{LCP})}{(A_{RCP}+A_{LCP})}$.

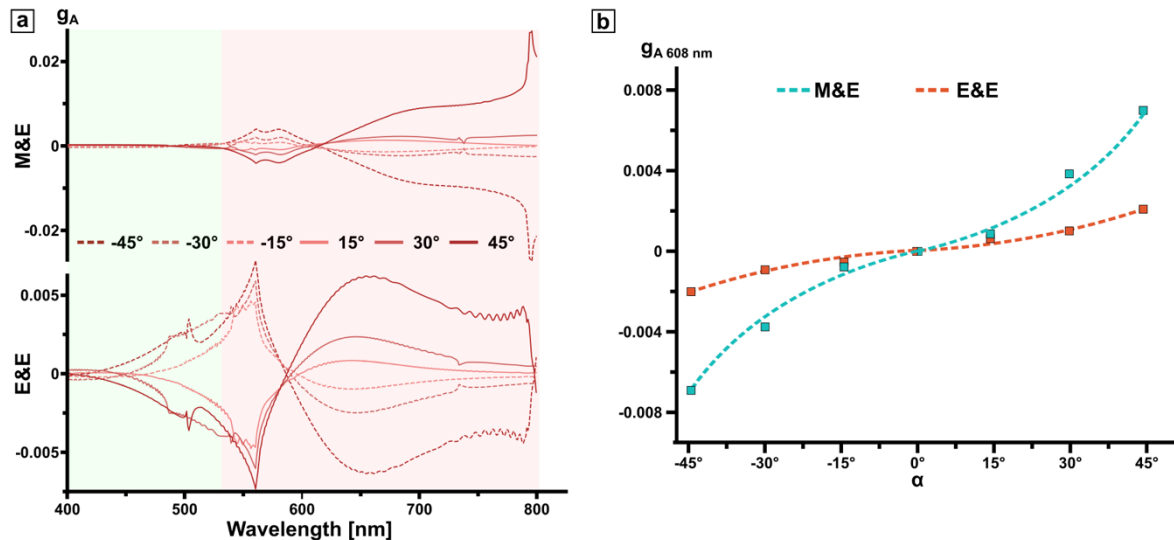Figure 31: Electromagnetic simulations of polarized photoluminescence. (a) The chiral response of stacked M&E and E&E at several complementary angles α between -45° and 45°. Absorption and emission bands of the QDs are shown in light green and red respectively. (b) The g_A-factor, measured at the maximum emission wavelength, with respect to various orientation angles for superimposed gratings.

The latter allows for uncovering the relation between the intrinsic circular dichroism of the crossed-bar-structures and the spectral properties of the emitter. As shown in Figure 31a, both stacked M&E and E&E structures demonstrate a mirror symmetry of the CD response for the opposite angles. Both combinations show a resonance near the maximum emission wavelength of the QDs that is characterized by crossing the zero g_A-value. The strongest CD signal corresponds the first and second diffraction orders at normal incidence (800 nm in air, and 560 nm in PDMS) that suggests the possible origin of chiral properties from the diffractive channels. Simulating CD effect in absorption gives further insight into the nature of the chiral emission: the strongest response matches the spectral region of photoluminescence that is in accordance with the results from one of the earlier reports.[372] Moreover, the broad emission spectrum of QDs allows for a broad wavelength range of the dichroic effect.

Conclusion

In conclusion, we propose a robust method for large-area manufacturing of light-emitting periodic 1D structures. When combined with a similar, but composed of light-absorbing gold, grating, the rising Moiré interference effect enables to achieve contrast values, significantly higher than when using material-wise identical gratings. The observed effect can be easily tuned over the micrometer-range distance and maintained for large inter-lattice separation that opens up a possibility to replace the spacer with various functional materials, such as photosensitive polymers,[385] activated at the QDs emission wavelength, or electrically conductive resins,[386] to extend the discussed concept to stimuli-responsive metasurfaces. Moreover, such spatially controllable, yet strong contrast can be further employed for security-labeling,[384] taking the advantage of the simplicity of mass-production and optical durability. On the other hand, Moiré's combination of two emitter gratings allows for a strong photoluminescent chiroptical effect. It demonstrates, for the first time, a reconfigurable chiral arrangement of semiconductor QDs without the need for supplementary chiral building blocks. To further increase the degree of polarization, one can benefit from the colloidal self-assembly approach and change the lattice geometry simply by designing a different stamp to introduce more hybridization states or implement additional emitter-based or plasmonic 1D gratings into the structure to obtain a more complex lattice overlay.[72,387] Moreover, one can confine the proposed chiral Moiré system within a nanocavity, taking the advantage of fluorescent enhancement.[388]

Experimental Section

Laser interference lithography

To produce a structured film on the glass substrate, LIL was employed. Right before use, microscopy glass slides were divided into individual pieces (2×2 cm) and cleaned with isopropyl alcohol and ultrapure water in a 1:1 ratio by sonication for 20 min at 37 kHz. Positive photoresist (mr-P 1202LIL, micro resist technology GmbH, Germany) was spin-coated onto the cleaned and dried under a stream of nitrogen substrate. Optimized spin parameters of 3000 rpm, acceleration of 1000 rpm s^{-1}, and total spin time of 33 s produced a thin film of 185 nm thickness, as confirmed by spectroscopic ellipsometry (RC2-DI, J.A. Woollam Co., Inc.). The coated substrates were baked at 95 °C for 60 s and further exposed to the 325 nm laser with a dose of 12 mJ/cm^2. The backside of the substrate was covered with black adhesive tape to avoid unnecessary reflections. To develop the exposed photoresist, the sample was submerged into the developer (mr-D 374/S, micro resist technology GmbH, Germany) for 2 min, rinsed with ultrapure water, and dried under a stream of nitrogen.

Fabrication of gold gratings

To fabricate a metal grating, a structured photoresist film was sputtered with gold at 20 rpm rotation speed with 0.1 nm/s until the thickness of 35-40 nm was achieved. The sacrificial photoresist was then dissolved with acetone and sonication at 45 °C, 37 kHz for 15 s.

Soft lithographic fabrication of QD grating

Produced by LIL, the structured film of a photoresist was replicated using an elastomeric silicone kit (Sylgard 184, Dow Chemicals, USA) with a ratio of prepolymer and catalyst of 10:1 to create the mold. The resulting mold was trimmed and fused by plasma treatment to an elastomeric silicone film in a petri dish. Right before use, the replica was immersed in 2 M hydrochloric acid for 30 min, rinsed with water, and dried under a stream of nitrogen to create a sufficiently hydrophilic surface. In the next step, 4 µL of a water-based dispersion of the colloidal solution (TGA-capped AgInS/ZnS QDs) was placed on a flat target substrate. The hydrophilized mold was placed on the quantum dot dispersion and 750 g of weights were placed on the petri dish to ensure close contact between the mold and the flat surface. The assembly was dried for eight hours at room temperature and relative humidity of 32%. The stamp was then removed

by peeling off. The quantum yield of the assembled structures was estimated up to 25% (see Appendix 8.4.5).[38]

Confocal fluorescence microscopy

CFM measurements were acquired with an inverted confocal scanning microscope (MicroTime 200, PicoQuant, Germany) with a 100X air objective (UPLFLN, NA 0.9, Olympus, Japan). For excitation, a picosecond pulsed transverse magnetic (TM)-polarized laser diode source (LDH-D-C-405, PicoQuant, Germany) with a center wavelength of 405 nm and a pulse width of 110 ps (full width at half maximum, FWHM), driven at a repetition rate of 0.5 MHz. For fluorescence collection, a dichroic mirror (ZT405-442/510rpc-UF3, Chroma, USA), a long pass filter with a cut-off below 425 nm (FF01-519/LP, Shamrock, USA) and a single photon counting module (SPCM-AQRH, Excelitas, USA) were used. For evaluation, SymphoTime 64 2.3 was used. For spectroscopy measurements, the sample was excited under a constant illumination at 405 nm and the signal was recorded by the spectrometer Newton 920 (Oxford Instruments, UK). For time-correlated single-photon counting (TCSPC), a single-photon counting module (SPCM-AQRH, Excelitas, USA) was used. The lifetime was then calculated by SymphoTime 64 2.3. Fluorescence life time images were recorded at 1 µW excitation power (before objective) and a dwell time of 2 ms per pixel.

Finite-Difference Time-Domain Simulations

A commercial-grade simulator based on the FDTD method is used to perform the calculations (FDTD: 3D Electromagnetic Simulator).[292] To simulate the optical response, two total-field scattered-field sources (λ = 400−800 nm) were used, illuminating the structure at a normal incidence with a relative phase shift of 90° or -90° for right- and left-circularly polarized light. We used perfectly matching the layer boundary conditions in Y-direction, and periodic boundary conditions along X- and Z-axes. The grating lines were represented by parallelepipeds with the dimensions, matching the ones, experimentally measured with atomic force microscopy. To obtain the optical responses of the system, frequency-domain field monitors were used. The frequency points were matching the wavelength span of the source. For the dielectric properties of gold, data from Johnson and Christy were fitted using six coefficients, with a root-mean-square (RMS) error of 0.25. For QDs, a Lorentz oscillator model was employed, with a resonance wavelength at the emission maximum of the QDs (608 nm) and a linewidth of 110 nm, matching the actual spectral width of the emission band. For the best simulation stability, the mesh area was set around the existing

structure in all three principal directions with a mesh step size of 1 nm and the auto-shutoff level was set to 10^{-7}.

Moiré interference measurements

To obtain Moiré interference pattern, the substrates need to be stacked with the structure side facing each other. The soft elastomeric substrate has to be pressed onto the glass substrate to ensure the close contact between the gratings. For the distance-dependent measurements, PMMA (A2 950 kDa, Microchemicals GmbH, Germany) was spin-coated at 1000 rpm for 60 s, followed by soft-baking at 180 °C for 60 s that resulted in a transparent polymeric film with the thickness of approximately 100 nm, determined by spectroscopic ellipsometry (RC2-DI, J.A. Woollam Co., Inc.). For larger film thicknesses, the latter was repeated up to maximum total thickness of approximately 4.4 µm. For the comparative contrast measurements, when two identical metal gratings are combined, index matching oil was applied between two glass substrates. In this case, the stacked structures were illuminated with a 640 nm laser and the reflected light was not filtered out.

Surface characterization

Produced line structures were imaged by AFM. The scanning was performed in the tapping mode with silicon nitride probes (typical resonant frequency in air: 296 kHz). Amplitude set-point was adjusted within the range of 100-200 mV at the scanning frequency 0.5-1 Hz.

7. Conclusion

The central point of this thesis is the realization of colloidal metasurfaces on a macroscopic scale and in a versatile, cost-efficient way for future advances in nanophotonics. To meet this challenge, the material properties of the colloidal building blocks had to be integrated into the optical design, self-assembly fabrication, and spectroscopic analysis of the emergent effects. Taking a closer look at individual optical properties of colloidal building blocks and connecting them to an intuitive visual perception, provides a starting point for the rational design of functional metasurfaces. The universal approach of spectral analysis and subsequent color conversion allows extending such an approach toward nanoparticles of arbitrary shapes and composition,[159,389,390] increasing not only the basic understanding of the optical

properties of colloids but also promoting the interest of a broad public towards nanotechnology.

The great potential of the colloidal approach is brought up by creating anisotropic functional metasurfaces via soft, template-assisted self-assembly that merges the principles of bottom-up wet chemical synthesis and self-assembly with top-down high-resolution photolithography. Such a combination provides an alternative to costly and non-scalable electron beam lithography, taking the advantage of monodispersity, monocrystalinity, and tunability of colloidal building blocks.[391] The novelty of this work lies in utilizing colloids with distinct optical functionalities and providing a comprehensive method to induce anisotropic and non-linear optical effects.

In such a way, metallic nanoparticles were assembled into 1D metallic photonic crystals on arbitrary substrates to demonstrate the hybrid polarization-dependent resonant behavior and induce photocurrent generation and facilitate photocatalysis. The suggested approach can be further extended to composite systems and hierarchical printing, where the light-absorbing and scattering components (metal nanoparticles) are combined with light-generating counterparts (semiconductor nanoparticles) to generate non-linear strong-coupling effects,[392,393] as well as utilize building blocks with functional surface coatings to achieve improved sensing, imaging or upconversion.[394]

Further on, the versatility of the suggested self-assembly method is transferred to semiconductor nanoparticles, where the main outcome is the amplification of the photoluminescence of the colloidal building blocks via the metasurface approach. By tuning the geometry of the 1D lattice, namely, its periodicity, we engineer the dispersive properties of the photonic crystal structure and control the directionality of the emitted light. Then, by including the thickness of a light-confining layer as an additional degree of freedom, we construct a purely colloidal nanolaser that, given a proper choice of the building blocks and ligands, can be also integrated within electrically driven, on-chip devices.[395] Finally, as a demonstration of the synergetic effect of combined metasurfaces, created, likewise, on flexible substrates, the Moiré configuration is established, exhibiting strongly anisotropic circularly polarized light that can be further employed for chiral sensing approaches, information processing, or labeling.

Moreover, this extended potential of producing periodic structures on a large scale with a simple printing technique, applicable for nanoparticles with different functionalities,

paves a path towards composite systems with parity-time symmetry, where the energy-amplifying and energy-dissipating building blocks are arranged in a balanced, alternating fashion.[396] Hence, such colloidal metasurfaces are of particular importance for novel photonic applications, i.e. cloaking or negative refractive index materials, showing a clear advantage to existing top-down manufacturing techniques.

8. Appendix

8.1. Optical properties of single nanocrystals via color perception of colloidal gold

To run the following code, a pre-installed Python 3 environment is needed. The optical properties of spherical AuNPs are calculated with the help of the Python package 'miepython' developed by Prahl following the procedure described by Wiscombe.[397,398] This package provides the functions to calculate scattering, absorption, and extinction efficiencies and needs to be installed beforehand. Besides that, the code requires NumPy and Maptplotlib packages.[399,400] The details of the algorithm are summarized in four steps, matching those that are shown in the flowchart of the main text:

1. The user is asked to set the initial parameters for the subsequent calculations: the diameter of the particles in nanometers and the surrounding environment (water, air, and some organic solvents are available as a choice). It has to be noted that the described procedure can be generalized to spheres of other non-absorbing, partially absorbing, or perfectly conducting materials by modifying the preset optical properties for gold in the code.

2. The absorption, scattering, and extinction spectra are calculated in a form of efficiency that is an amount of corresponding optical power for a given irradiance, normalized by the particle cross-section area, and displayed on the screen as a first output.[401]

3. Henceforth, the spectra have to be converted to single colors that can be displayed on the computer monitor. The human eye possesses three types of cone cells, having different sensitivities for the short (blue), middle (green), and long (red) wavelengths of the visible spectrum, that determine our color perception under the bright illumination.[170] This also means that any perceived color can be described by combining the light of three primary 'color-matching' spectra of colors, close to red (R), green (G), and blue (B). The reference CMFs are standardized by the Commission Internationale de l'Eclairage (CIE).[402] Each function gives the amount of primary needed to create the desired color when all three are mixed. Thus, by mapping any spectrum of the object under standard illumination to CMF one can get three 'stimulus'

values X, Y, Z that model a chromatic response of the observer, in analogy to the actual response of the human eye:

$$X = \sum_{380\ nm}^{740\ nm} D_{65}(\lambda)S(\lambda)r(\lambda)\Delta\lambda$$

$$Y = \sum_{380\ nm}^{740\ nm} D_{65}(\lambda)S(\lambda)g(\lambda)\Delta\lambda \qquad (5)$$

$$Z = \sum_{380\ nm}^{740\ nm} D_{65}(\lambda)S(\lambda)b(\lambda)\Delta\lambda$$

where $\Delta\lambda$ is the wavelength step, $D_{65}(\lambda)$ the spectrum of the daylight (CIE standard illuminant), $S(\lambda)$ – the corresponding spectrum and $r(\lambda)$, $g(\lambda)$, and $b(\lambda)$ are the wavelength-dependent CMF. The obtained X, Y, Z values are then normalized to achieve a uniform intensity of the perceived colors.[403]

4. For a more convenient visualization, these normalized chromaticity x, y, z coordinates on the color gamut are converted to standard RGB values that can be processed and displayed on the monitor. For this, the x, y, z-set is multiplied by the conversion matrix M_{RGB} that does not change the color itself, but 'moves' it from one color space to another:

$$\begin{pmatrix} R \\ G \\ B \end{pmatrix} = M_{RGB} \begin{pmatrix} x \\ y \\ z \end{pmatrix} \qquad (6)$$

Additionally, there are some corrections and assumptions to be made, to allocate the calculated R, G, B values on to the standard scale of 0-255. First, the response of the human eye to the colors of different brightness is not linear. To account for that, the so-called 'gamma-correction' stretches the 0-255 scale in a non-linear fashion. Secondly, the calculated values can appear outside the desired range since not all the colors from the CIE color gamut can be reproduced on the computer monitor. The simplest way to deal with that is to clip the values less than 0 and higher than 255 to 0 and 255, respectively. Such an excessive truncation has a side effect of not representing the hues with high accuracy but still is sufficient for color reproduction.[2] As a final output, the RGB coding for scattered, absorbed and transmitted colors are displayed.

```python
#!/usr/bin/env python3
# This program requires the installation of an additional package
# miepython from https://github.com/scottprahl/miepython
# By running the following code the user is asked to enter the diameter
of the nanoparticle
# and the surrounding medium. As an output, a graph with absorption,
scattering and
# extinction will be displayed on the screen and the respective colors
will be printed in the console.

import numpy as np
import matplotlib.pyplot as plt
import miepython

# Set the optical properties of Au (from
https://refractiveindex.info/?shelf=main&book=Au&page=Johnson)
# Wavelength is given in nanometers
ref_index=np.loadtxt("n k.txt")
lam = ref_index[:,0]
n = ref_index[:,1]
k = ref_index[:,2]

# Set the refractive index of the environment (n=1 air, n=1.33 water)
# Diameter of the spheres is given in nanometers
print("Please enter the diameter of the particles in nm:")
diameter = int(input())

print("Please select surrounding medium (air, water, acetone, ethanol,
toluene, hexane, chloroform, or propanol):")
n_env=input()

if n_env=='air':
    n_env=1.000
elif n_env=='water':
    n_env=1.333
elif n_env=='acetone':
    n_env=1.359
elif n_env=='ethanol':
    n_env=1.36
elif n_env=='toluene':
    n_env=1.496
elif n_env=='hexane':
    n_env=1.375
elif n_env=='chloroform':
    n_env=1.445
elif n_env=='propanol':
    n_env=1.387
else:
    print("Invalid input")

# If the input parameters are correct, proceed further. Otherwise, the
program will be terminated.
if isinstance(n_env,float)==True:
    # Calculate the scattering (qqsca), absorption (qqabs) and
extinction (qqext) efficiencies
    num = len(lam)
    m = (n-1.0j*k)/n_env
    var = np.pi*diameter/lam*n_env

    qqabs = np.zeros(num)
    qqsca = np.zeros(num)
    qqext = np.zeros(num)
```

```python
    for i in range(num) :
     qext, qsca, qback, g = miepython.mie(m[i],var[i])
     qabs = qext - qsca
     qqabs[i]=qabs
     qqsca[i]=qsca
     qqext[i]=qext

    # Plot the absorption, scattering and extinction efficiencies
    fig, ax = plt.subplots()
    ax.plot(lam, qqabs, linewidth = '3')
    ax.plot(lam, qqsca, linewidth = '3')
    ax.plot(lam, qqext, linewidth = '3')
    ax.set(xlabel='Wavelength [nm]', xlim = (380, 740),
ylabel='Efficiency [a.u.]', title='{}'.format(diameter)+' nm Au
nanosphere')
    ax.legend(['Absorption', 'Scattering', 'Extinction'])
    plt.show()

    # Spectrum to color conversion
    # Load CIE 1931 2-deg color matching functions
http://cvrl.ioo.ucl.ac.uk/ CIE
    CMF=np.loadtxt("x y z D65.txt")
    x = CMF[:,1]
    y = CMF[:,2]
    z = CMF[:,3]
    # Load relative spectral power of a standard illuminant D65
    D65 = CMF[:,4]
    # Load conversion matrix from XYZ coordinates to sRGB
    M_sRGB=np.array([[3.2404542, -1.5371385, -0.4985314],[-0.9692660,
1.8760108, 0.0415560], [0.0556434, -0.2040259, 1.0572252]])

    spectra = np.column_stack((qqabs, qqsca, qqext))
    rgb = np.zeros((3,3))
    for i in range(3):
        spectrum = spectra[:,i]
        # Convert the spectrum to CIE chromaticity values (X,Y,Z) by
integrating the spectrum over the color matching functions
        D65_x_r_sum=np.sum(x*D65*spectrum)
        D65_y_r_sum=np.sum(y*D65*spectrum)
        D65_z_r_sum=np.sum(z*D65*spectrum)

        D65_x_sum=np.sum(x*D65)
        D65_y_sum=np.sum(y*D65)
        D65_z_sum=np.sum(z*D65)

        # Remove the intensity dependence of the calculated color
        X = D65_x_r_sum/D65_y_sum
        Y = D65_y_r_sum/D65_y_sum
        Z = D65_z_r_sum/D65_y_sum

        # Calculate normalized chromaticities
        xx = X/(X+Y+Z)
        yy = Y/(X+Y+Z)
        zz = Z/(X+Y+Z)

        # Convert to standard linear RGB
        rgb[i,:]=np.dot(M_sRGB,[xx,yy,zz])
```

8.2. Directional amplified photoluminescence in large-area perovskite-based metasurfaces

8.2.1. Detailed working principle of a light-emitting metasurface

Figure 32 provides a visual representation of a working principle of a light emitting metasurface. This particular example is considered for TM polarization and can be similarly applied for TE polarization. Upon the broadband illumination, a portion of the spectrum is absorbed by perovskite nanocrystals, forming excited states (Figure 32a). Upon relaxation, photons of the corresponding energies are expected to partially preserve the orientation of the polarization. The latter follows from the preferential excitation of perovskites, where the absorption dipole moments are oriented along the electric vector.[404] As there is no rotational diffusion in a solid film of emitters, we assume preservation of polarization direction in the emitted light (Figure 32b). Whereas the transmittance spectrum of a flat film of perovskites reveals only the absorption by the perovskite material and uniform scattering, the transmittance of a structured metasurface demonstrates the sharp dip in the spectrum that can be attributed to the diffraction on the grating (Figure 32c). Correspondingly, the emitted light from a metasurface features the enhancement (an increased number of emitted photons) at a particular wavelength and in particular directions, defined by the diffraction (Figure 32d).
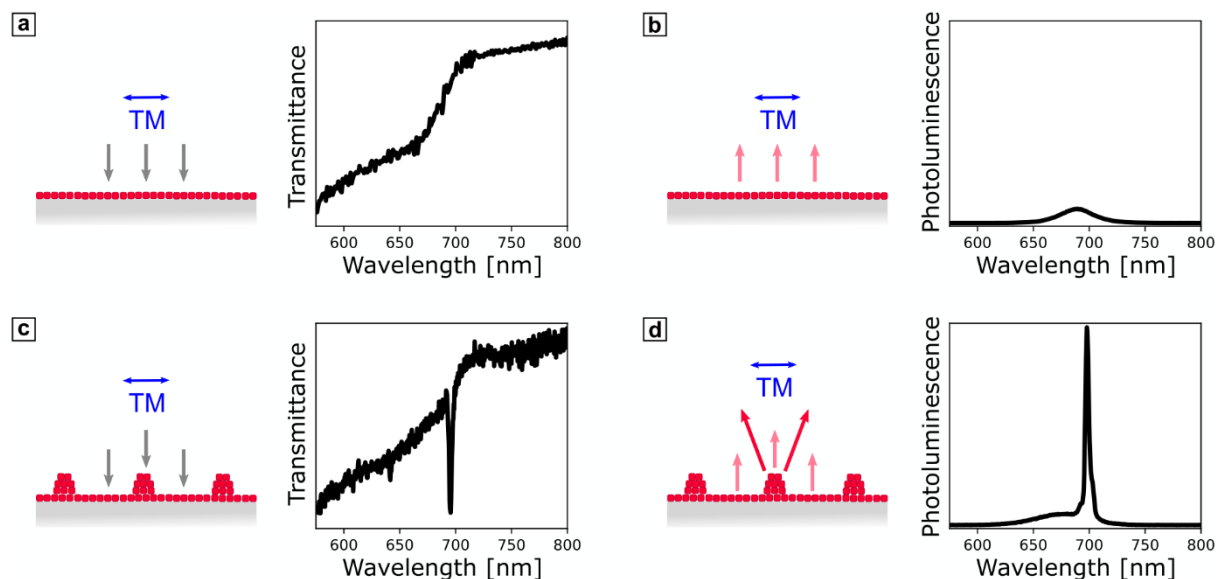

Figure 32: Schematic representation of (a) a flat film of perovskites and (c) structured metasurface under the broadband TM-polarized illumination and the corresponding experimentally measured transmittance spectra. Schematic representation of photoluminescence (PL) from (b) a flat film of perovskites and (d) structured metasurface together with the corresponding detected PL spectra.

8.2.2. Optical properties of bulk perovskite material

To determine the refractive index of $CsPbI_3$, spectroscopic ellipsometry measurements were performed. For this, a thin layer of perovskites was prepared on the Si substrate by the spin-coating technique. A ~50 mg/mL solution was drop-casted in a dynamic coating mode at 3000 rpm. The thickness and roughness of the thin film were determined with the help of AFM measurements (41 ± 7 nm) and were then utilized as the starting parameters for the fitting procedure of the ellipsometric data. The initial fitting range was set to a transparent region of 700 – 1300 nm, where the experimental data was approximated with the B-spline model. After expanding to a full wavelength range, the B-spline model was parameterized by a set of oscillators, matching the characteristic peaks in the absorption spectrum.[405]
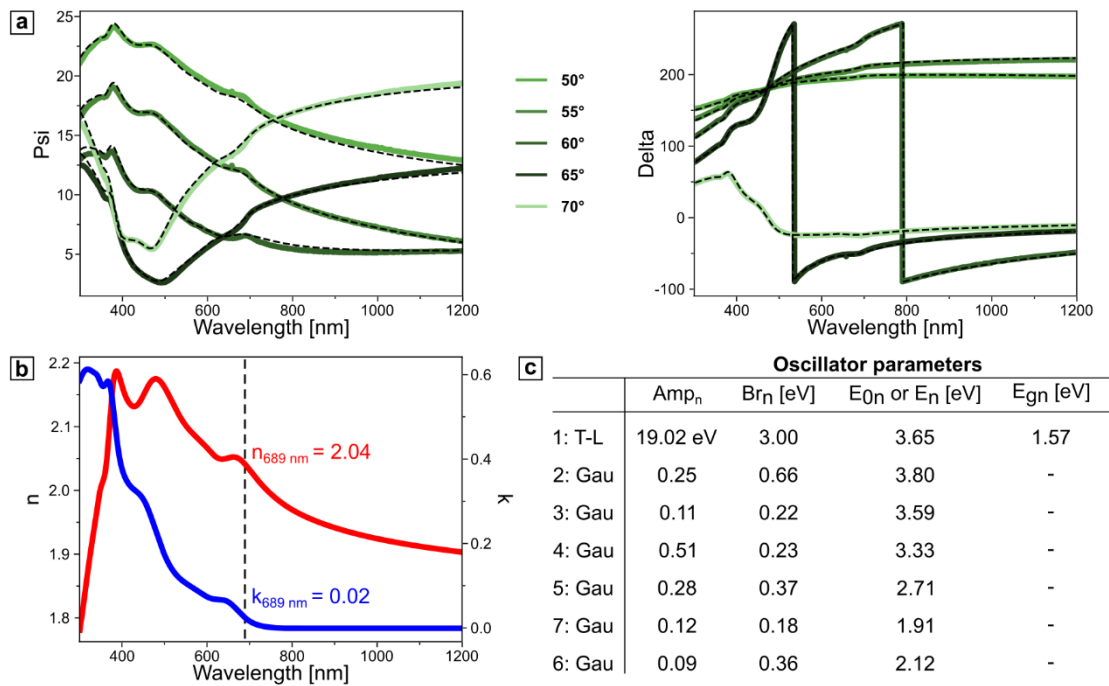

	Oscillator parameters			
	Amp_n	Br_n [eV]	E_{0n} or E_n [eV]	E_{gn} [eV]
1: T-L	19.02 eV	3.00	3.65	1.57
2: Gau	0.25	0.66	3.80	-
3: Gau	0.11	0.22	3.59	-
4: Gau	0.51	0.23	3.33	-
5: Gau	0.28	0.37	2.71	-
7: Gau	0.12	0.18	1.91	-
6: Gau	0.09	0.36	2.12	-

Figure 33: Ellipsometry characterization of the thin-film $CsPbI_3$: (a) psi and delta ellipsometric parameters for angles in the range of 50° - 70° together with an appropriate model fit with the MSE<3.5. (b) Wavelength-resolved optical (real n and complex k) constants. (c) Oscillator parameters of the model fitted to the psi and delta parameters.

8.2.3. Effect of the concentration of the colloidal solution on the assembly

The concentration of the colloidal nanocrystals plays a crucial role in the assembly process. By adjusting the concentration, one can achieve different thicknesses of the flat layer assembled upon drying under the periodic pattern (Figure 34a). The unavoidable initial drying of the solvent during the time gap between the drop-casting

of the colloidal solution and stamp placement results in a thin film formation. The thickness of this pre-assembled layer is governed by the concentration and the spreading of the colloidal solution, and, thus, varies on the millimeter-scale over the structured area. Nevertheless, such variations appear within certain concentration ranges and can be visually estimated through the color appearance of the produced structured pattern; the darker color indicates the higher layer thickness, as demonstrated in Figure 34b-d.
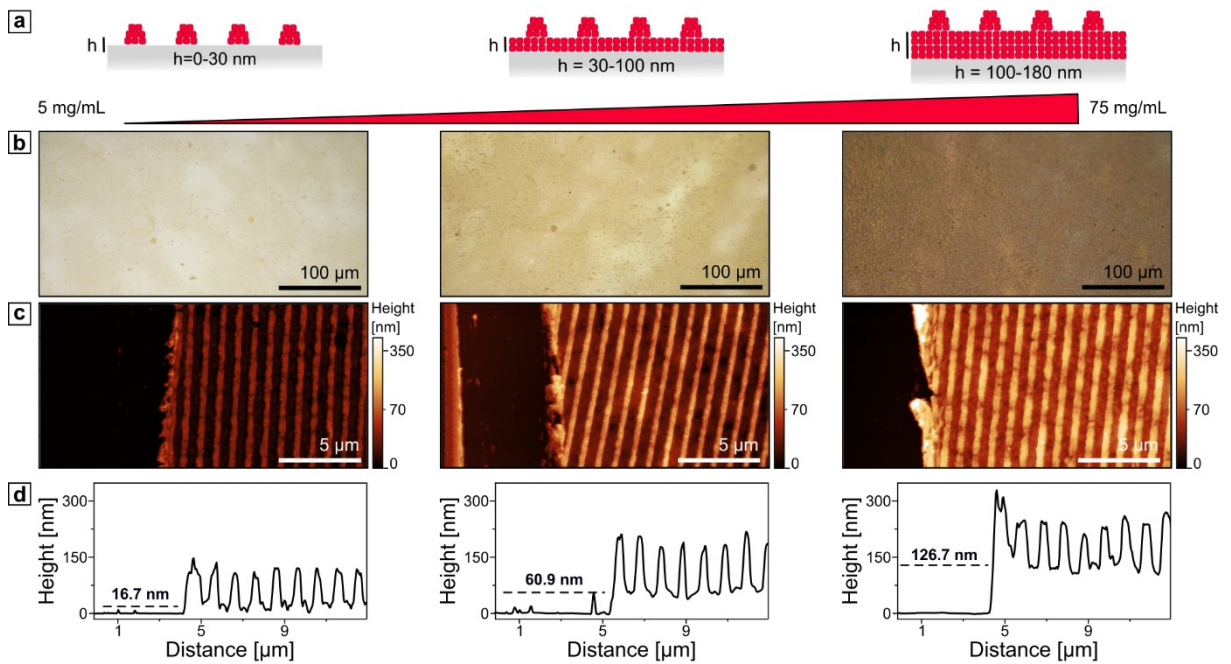

Figure 34: (a) Schematic representation of structured films with different thicknesses of the underlying layer depending on the concentration of the colloidal solution. (b) Bright-field microscopy images of three representative structured surfaces with the concentration increasing from left to right. (c) AFM micrographs and (d) corresponding height profiles were measured across the pattern perpendicular to the grating lines.

8.2.4. Peak fitting procedure

The fitting procedure was performed with the help of the python-based script using the *lmfit* package based on non-linear least-squares minimization.[406] The PL spectra of a flat film was fitted with a Gaussian model, whereas the PL spectrum from the metasurface were approximated with the help of Gaussian and Lorentzian models, the latter matching the right-shoulder peak of the amplified PL.
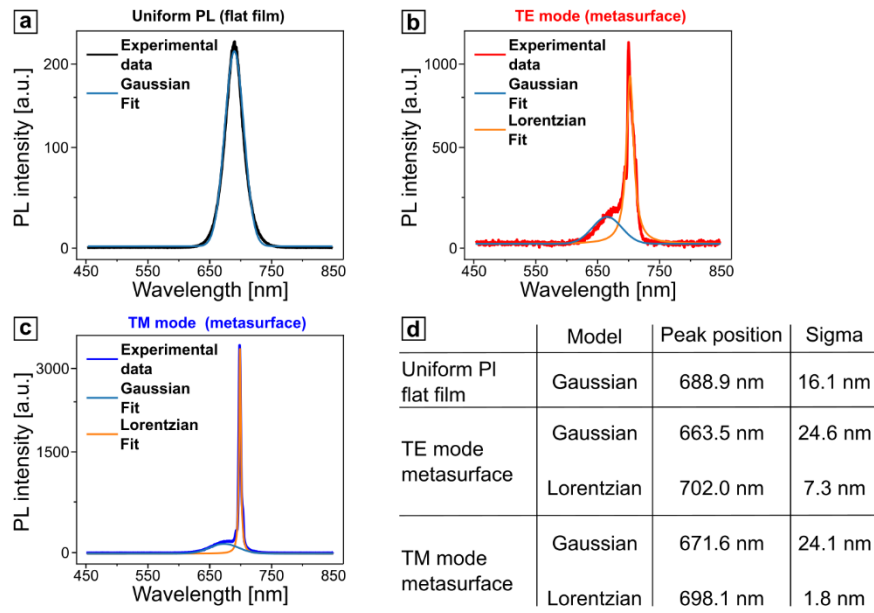
Figure 35: Detailed spectral analysis of the PL at 0° detection angle (Γ-point) for (a) uniform PL from a flat film; and a periodic 1D structured metasurface under (b) TE and (c) TM polarizations. (d) Summary of the fitted peak parameters.

8.2.5. Comparative study on PL amplification

Table 4: Comparison of the amplification factors in structured perovskite metasurfaces, depending on the manufacturing technique.

Amplification factor	Processes involved	Perovskites	Pattern geometry	Minimum size/periodicity	Reference
70	Hard NIL & annealing	MAPbI$_3$-based composite	Lines and holes	300 nm	[261]
24	Reactive ion etching	CsPbBr$_{2.75}$I$_{0.25}$	Holes	280 nm	[407]
21	Infiltration to a photonic crystal	MAPbBr$_3$	3D opal	200 nm	[408]
13	Soft NIL	CsPbI$_3$	Lines	300 nm	This work
12	Combination with a plasmonic metasurface	MAPbI$_3$	Holes	200 nm	[409]
8	Hard NIL	MAPbI$_3$	Lines	350 nm	[410]

7	Template-confined epitaxial growth	$MAPbBr_3$	Lines	600 nm	[259]
5	Combination with a plasmonic metasurface	$MAPbBr_3$	Randomly distributed disks	-	[411]
5	Soft NIL & annealing	$CsPbBr_3$	Cylinders & Cones	400 nm	[412]
4	Combination with a plasmonic metasurface & reactive ion etching	$MAPbBr_3$	Randomly distributed disks	-	[413]
4	Thermal hard NIL	$MAPbI_3$	Triangles	400 nm	[414]
4	Infiltration to a photonic crystal	$CsPbBr_3$	Kagome lattice	250 nm	[415]
3	Focused ion beam milling	$MAPbI_3$	Lines & holes	300 nm	[416]
3	Thermal hard NIL	$MAPbI_3$	Lines	600 nm	[258]
2	Soft NIL & annealing	$MAPbI_3$	Lines and holes	1000 nm	[145]
<2	Reactive ion etching	$CsPbBr_3$	Holes	157 nm	[417]
<2	Hard NIL & annealing	$MAPbI_3$	Lines	600 nm	[418]
<2	Focused ion beam milling	$MAPbBr_3$	Cylinders	400 nm	[419]

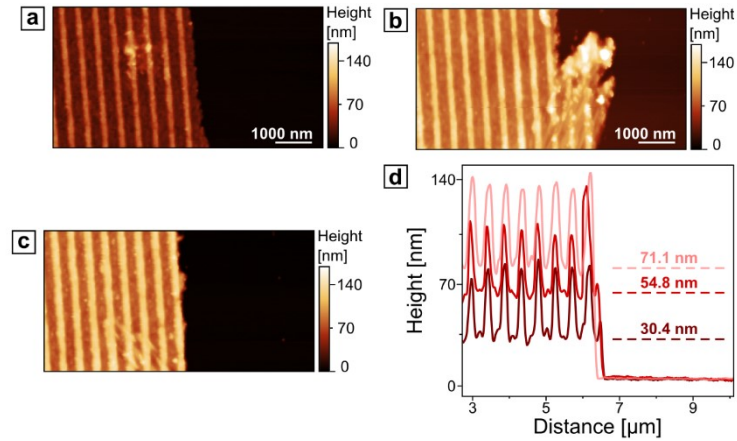### 8.2.6. Thickness variation of the waveguide-like layer

Figure 36: (a-c) AFM micrographs of three different measurement positions on the 450 nm periodic structured film, where the corresponding angle-resolved spectroscopic measurements were taken. (d) Thickness cross-section profiles were taken across the AFM micrographs, perpendicular to the grating lines.

8.3. Non-linear light amplification in quantum-dot-based metasurfaces

8.3.1. Optical properties of bulk CdSe/ZnCdS material

For the spectroscopic ellipsometry measurements, a monolayer layer of CdSe/ZnCdS QDs was transferred on a Si substrate by Langmuir-Blodgett deposition. The thickness and roughness of the thin film were determined with the help of AFM measurements and were then utilized as fixed parameters for the fitting procedure of the ellipsometric data. The initial fitting range was set to a transparent region of 750 – 1300 nm, where the experimental data was approximated with the B-spline model. After expanding to a full wavelength range, the B-spline model was parametrized by a set of oscillators, matching the characteristic peaks in the absorption spectrum.
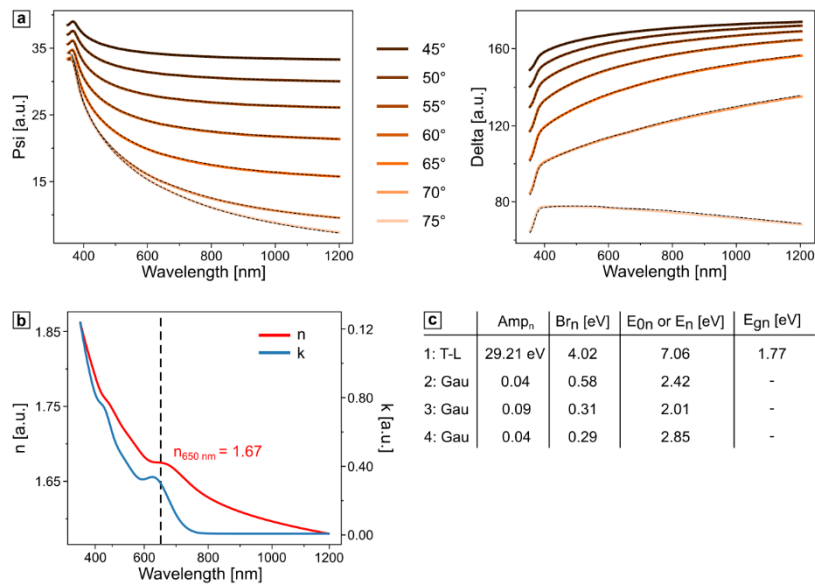
Figure 37: Ellipsometry characterization of the thin-film CdSe/ZnCdS: (a) psi and delta ellipsometric parameters for angles in the range of 45° - 75° together with an appropriate model fit with the MSE<3.5. (b) Wavelength-resolved optical (real n and complex k) constants. (c) Oscillator parameters of the model fitted to the psi and delta parameters.

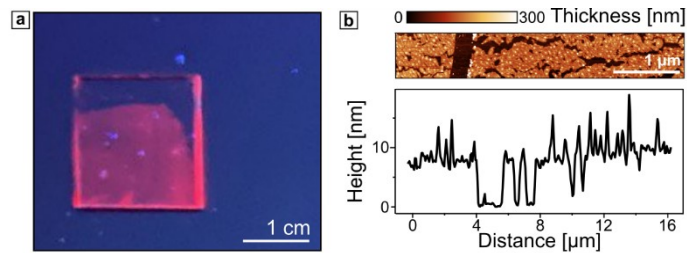| c	Amp$_n$	Br$_n$ [eV]	E$_{0n}$ or E$_n$ [eV]	E$_{gn}$ [eV]
1: T-L	29.21 eV	4.02	7.06	1.77
2: Gau	0.04	0.58	2.42	-
3: Gau	0.09	0.31	2.01	-
4: Gau	0.04	0.29	2.85	-

Figure 38: (a) Photograph of a monolayer of QDs deposited by Langmuir-Blodgett technique on a glass substrate under UV-lamp illumination. (b) AFM micrograph of a monolayer, with a vertical scratch to identify the height profile.
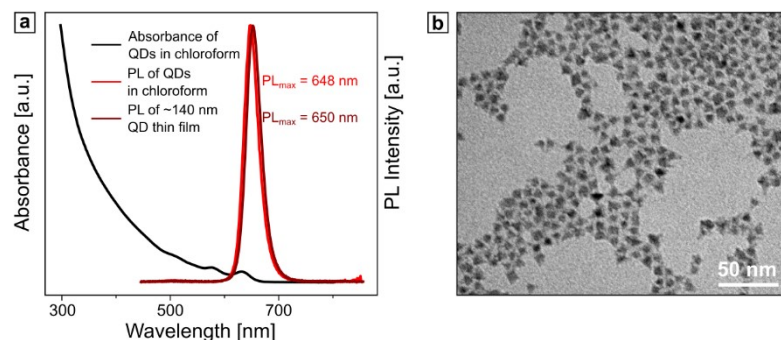

Figure 39: (a) Absorption and PL spectrum of QDs in solution and in a densely packed film. (b) TEM image of the CdSe/ZnCdS nanocrystals.

8.3.2. Peak fitting procedure

The fitting procedure was performed with the help of the python-based script using the *lmfit* package based on non-linear least-squares minimization.[406] The PL spectra of a

flat film was fitted with a Gaussian model, whereas the PL spectrum from the metasurface were approximated with the help of Gaussian and Lorentzian models, the latter matching the right-shoulder peak of the amplified PL.
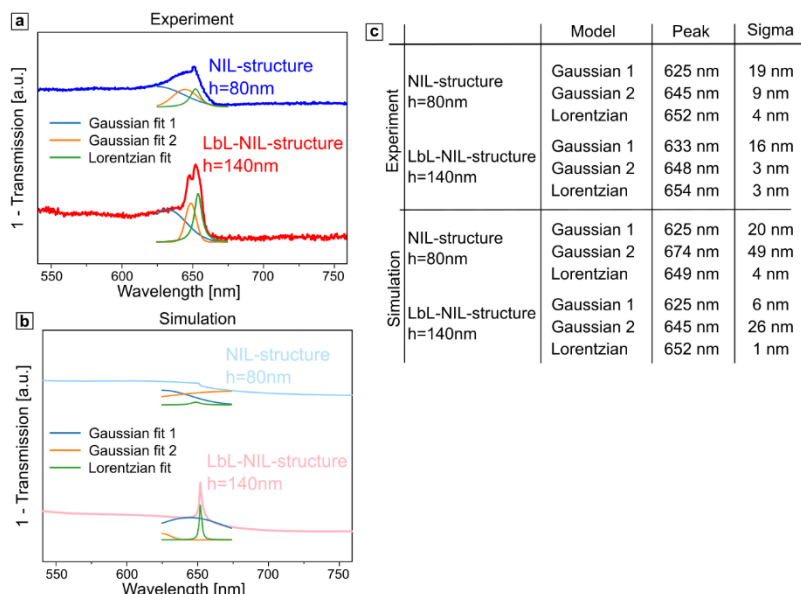

Figure 40: Detailed spectral analysis of the (a) experimental and (b) simulated transmission spectra of the structured metasurfaces, produced with NIL and Lbl-NIL techniques. (c) Summary of the fitted peak parameters. The fitting procedure was performed with the help of the python-based script using the *lmfit* package.[420]

8.3.3. Comparative characteristics of the Cd-based 2nd order DFB lasers

Table 5: Comparison of the lasing thresholds in structured colloidal core-shell Cd-based metasurfaces, depending on the manufacturing technique.

Lasing threshold [mJ/cm^2]	Processes involved	QDs	Reference
0.01	Spin-coating on a structured photonic crystal	CdS_xSe_{1-x}/ZnS	[422]
0.03	Spin-coating on a structured plasmonic crystal	CdSe/CdS	[323]
0.03	Spin-coating on a structured photonic crystal	CdSe/CdS	[333]
0.08	Spin-coating on a structured photonic crystal	CdSe/CdZnS/ZnS	[339]

0.12	Spin-coating on a structured photonic crystal	CdSe/ZnCdS	[421]
0.12	Template-stripping	CdSe/CdZnS	[87]
0.3	Spin-coating on a structured photonic crystal	CdSe/CdS/ZnS	[130]
0.5	Spin-coating on a structured plasmonic crystal	CdSe/ZnS	[340]
0.6	LbL-NIL	CdSe/ZnCdS	This work
0.95	NIL	Polymer-conjugated CdSe/ZnS	[423]
1	Spin-coating on a structured plasmonic crystal	CdSe/CdS	[240]

8.4. Tunable circular dichroism induced by self-assembled photoluminescent Moiré lattices

8.4.1. Moiré interference

After superimposing two gratings, the resulting Moiré periodicity P_m can be calculated by the following equation:

$$(2P_m)^2 = (2P_1P_2)\frac{1 + cos\,(\alpha)}{sin^2(\alpha)}$$

(7)

where P_1 and P_2 are with the periodicities of the two superimposed gratings respectively. As an example of Moiré interference, the combination of metal and emitter grating was considered. The wide-field and zoomed-in confocal fluorescence microscopy (CFM) images of supra-periodic pattern, shown in Figure 41, reveal the presence of the Moiré interference effect over a large area.
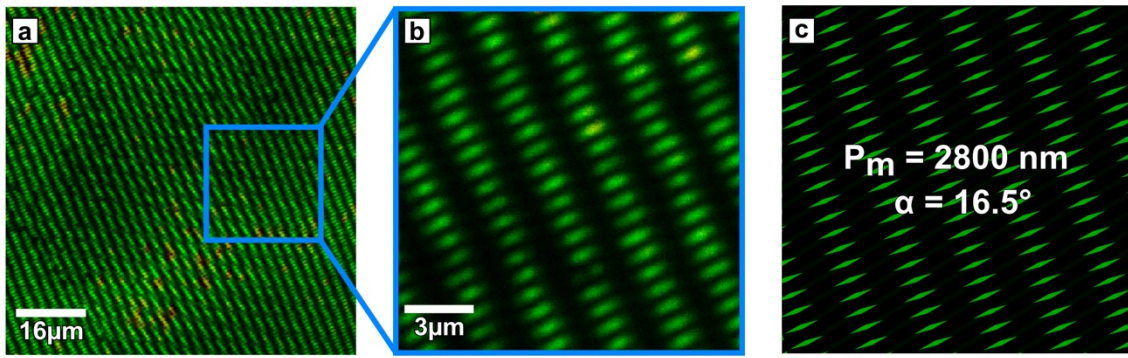
Figure 41: (a) A 80x80μm and (b) zoomed-in 15x15μm CFM image of the stacked metal and emitter lines. (c) graphical representation of the analytically calculated Moiré pattern.

The experimentally obtained Moiré patterns, shown in Figure 41b match the graphically produced ones, obtained through the analytical calculations according to Equation 7 (Figure 41c).

8.4.2. The Moiré contrast amplitudes for various grid combinations

To estimate the contrast amplitude for various combinations of superimposed gratings, the $C_{M,R}$ values were calculated with the respect to an emitter grating, where the contrast amplitude created only by the QDs emission was considered as 100% with a background noise error of 11% measured along the emitter lines:

Table 6: The contrast amplitude values, multiplied by 100%, of stacked metal and metal (M&M), emitter and emitter (E&E), metal and emitter (M&E) gratings.

	M&M	E&E	M&E
C_R	103%	99%	95%
C_M	69%	72%	107%

8.4.3. Tunable circular dichroism

The chiroptical effect of the superimposed M&E and E&E stacked gratings was detected by the spectroscopic measurements of the circularly polarized photoluminescence and summarized in Figure 42. It is worth noting that due to the limited focal length of the microscope objective, the stacked sample has to be positioned with a thin glass substrate facing the incoming excitation light. Thus, to switch between the left and right chiral configurations, the stacked gratings were

rotated clockwise and counterclockwise to induce left and right circularly polarized light. To calibrate the emission, all spectra were normalized with regard to a blank glass substrate superimposed with a blank PDMS. A single emitter grating was used as a reference and, as expected, no spectral difference was observed for all the orientations, as shown in Figure 42a). On the contrary, strong asymmetry in LCP and RCP photoluminescence of the stacked structures indicates the presence of chiroptical effect that was characterized by the degree of polarization (see the main text).
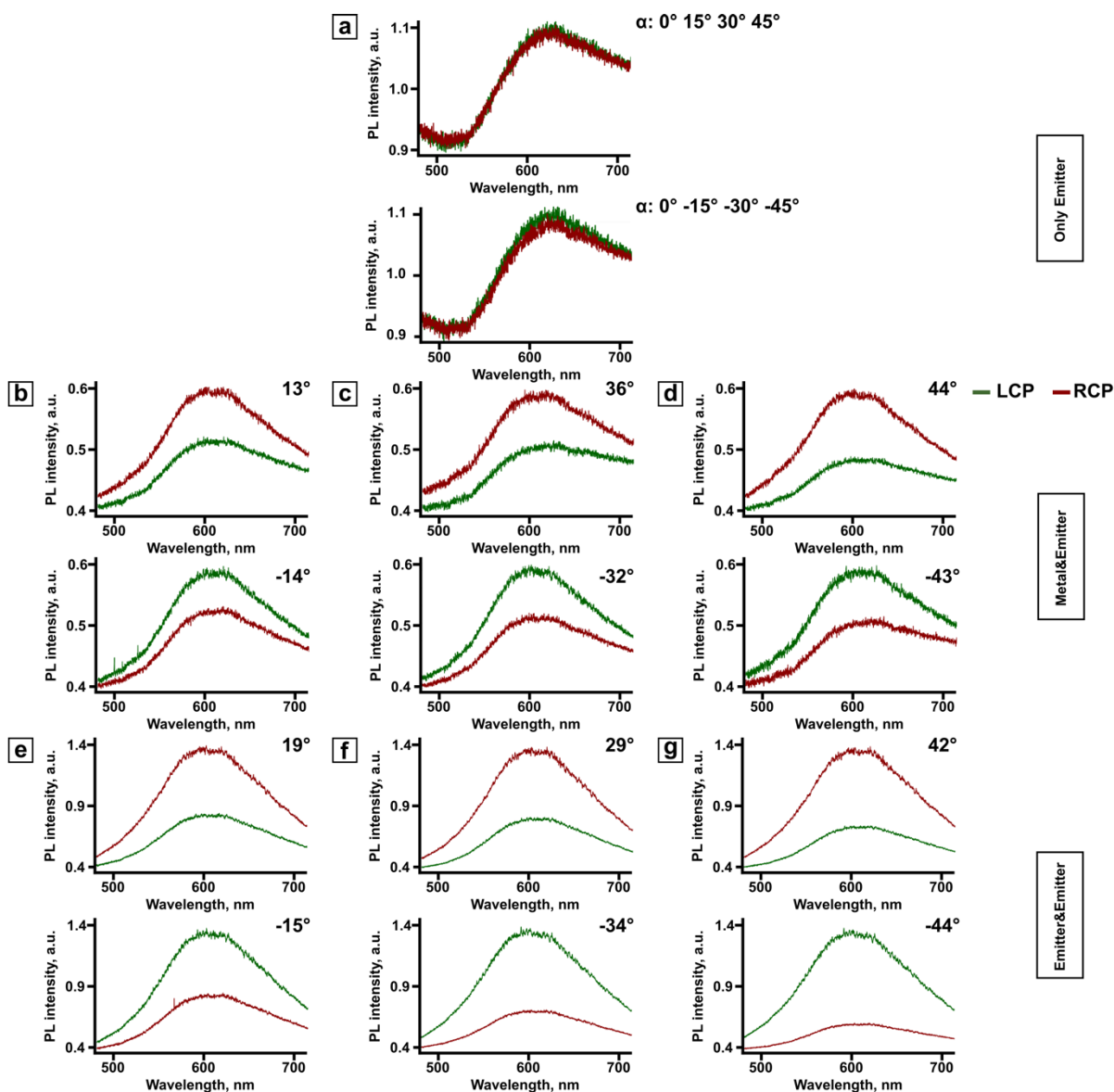

Figure 42: The spectral data of RCP (red) and LCP (green) photoluminescence of (a) rotated single emitter grating, (b-d) stacked metal and emitter, (e-g) emitter and emitter gratings at several complementary angles α between 0° and 45°.

8.4.4. Numerical simulations

To give an additional insight into the chiroptical effect of the superimposed M&E and E&E gratings, the field distribution as well as the polarization conversion efficiency were calculated for 45°/-45° crossing angle in the E&E configuration (see Figure 43). The far-field output was calculated by projecting the near-field response and calibrating it to the incident beam. Both near- and far-field results demonstrate mirror symmetry, which supports the chiral nature of the electric fields. The polarization conversion ratio (PCR) was calculated according to the following equations:[424]

$$PCR_{right} = \frac{T_{left}^{2}}{T_{left}^{2} + R_{right}^{2}} \tag{8}$$

$$PCR_{left} = \frac{T_{right}^{2}}{T_{right}^{2} + R_{left}^{2}} \tag{9}$$

where T and R correspond to the transmission and reflection coefficients of the respective circular polarization. Near the emission wavelength, the PCR value for both polarizations is 99.5%, reaching even higher values at a longer wavelength, which corresponds to almost ideal polarization conversion of the electromagnetic wave. Overall, such a configuration of emitter lines crossing at 45° or -45° demonstrates strong polarization conversion throughout the visible wavelength range.
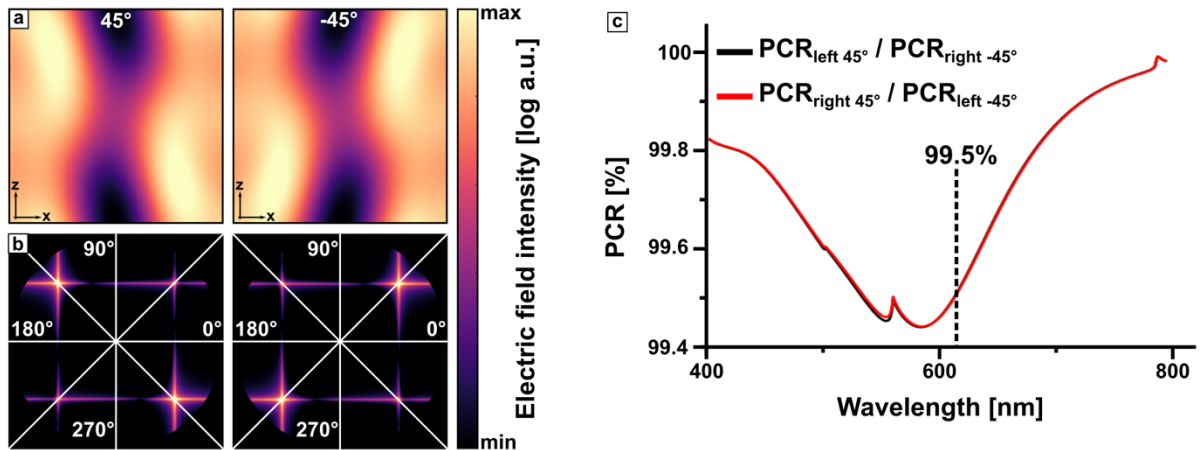

Figure 43: (a) Near-field and (b) corresponding polar plot of the projection in the far-field. (c) Calculated PCR for left- and right-circular polarizations. The PCR at 608 nm is marked with the dotted line.

8.4.5. Optical properties of AgInS/ZnS core/shell QDs

Colloidal AgInS/ZnS core/shell QDs, being dispersed in aqueous solution, exhibit PLQY of 47%.[374] To estimate, how the PLQY is affected by simple drying of the colloidal solution and by a direct assembly of the nanocrystals into closely packed

structures, one can take the advantage of the lifetime evaluation with the TCSPC measurements. This gives a semi-quantitative comparison of the PLQY. Three instances were considered: a diluted water-based solution of AgInS/ZnS core-shell QDs; an aggregate, formed after drop-casting the solution on the substrate, followed by drying at room temperature; and the structured QD-based film, manufactured by confinement self-assembly. The average lifetime was calculated by fitting the intensity decay with the 3-exponential tailfit by using the calculated instrument response function (IRF). The lifetime values are summarized in Table 7.

Table 7: The calculated lifetime τ values, together with the goodness of fit χ^2, and the estimated PLQY for QDs in solution, in the dried aggregated state and in the assembled grating.

Sample	τ	χ^2	PLQY
Liquid	120.00 ± 0.80 ns	1.030	47%
Aggregate	82.00 ± 0.37 ns	1.098	32%
Structure	65.00 ± 1.90 ns	1.195	25%

Overall, upon drying and assembling into closely packed structures, QDs demonstrate a stronger exponential decay rate with the shortening of the lifetime, as shown in Figure 44a). By definition, $PLQY = k_r\tau$, where k_r is the radiative decay rate and τ is the average lifetime. In the case of classical fluorescence, one can assume the k_r being constant, and, thus, infer the decrease in PLQY down to 25%.[388] The latter can be explained by close packing of the emitters upon drying, and even further spatial confinement as a result of the assembly process, which causes the minimal core-to-core distance and, thus, quenching effects. Nevertheless, it did not hinder observing the optical effects, such as strong contrast and chiral emission. At the same time, no spectral shift was observed in the emission spectrum for all three cases (see Figure 44b), although the intensity, together with the signal-to-noise ratio, for the QD-based grating was significantly lower than for the dried aggregate or the diluted solution. This is due to a much lower actual number of the excited QDs and possible quenching.
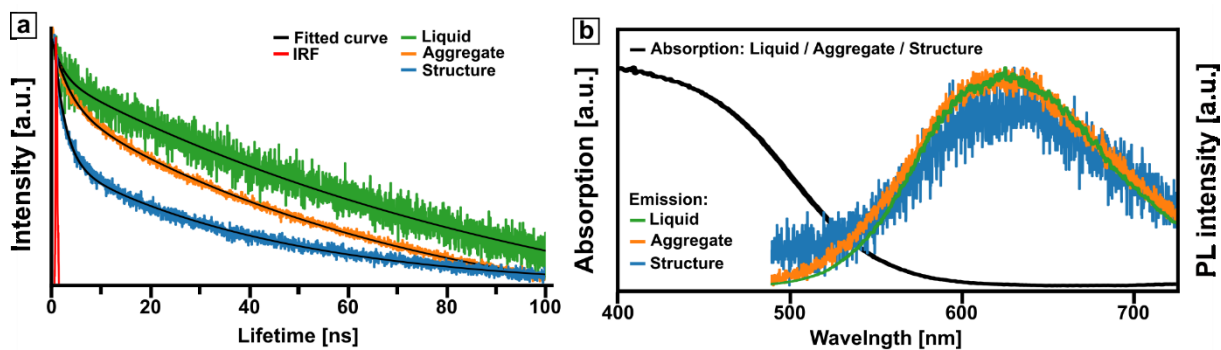
Figure 44: (a) TCSPC of the QDs in aqueous solution (shown in green), in a dried state on the substrate (shown in orange) and of the QDs, assembled in a grating (shown in blue). The 3-exponential reconvolution fitting is marked by black curves, with the instrument response function (IRF) shown in red. (b) Absorption and emission spectra of the QDs, normalized to the maximum value.

8.5. Contribution to other joint publications

Complex Metal Nanostructures with Programmable Shapes from Simple DNA Building Blocks

Jingjing Ye[1,4], Olha Aftenieva[2], Türkan Bayrak[3,4], Archa Jain[3], Tobias A. F. König[2,4], Artur Erbe[3,4], Ralf Seidel[1,4*]

1. Molecular Biophysics group, Peter Debye Institute for Soft Matter Physics, Universität Leipzig, 04103 Leipzig, Germany

2. Leibniz-Institut für Polymerforschung Dresden e. V., Hohe Straße 6, 01069 Dresden, Germany

3. Institute of Ion Beam Physics and Materials Research, Helmholtz-Zentrum Dresden-Rossendorf, 01328 Dresden, Germany

4. Center for Advancing Electronics Dresden (cfaed), Technische Universität Dresden, Helmholtzstraße 18, 01069 Dresden, Germany

* Corresponding author: ralf.seidel@physik.uni-leipzig.de

J.Y. performed DNA-origami design and seeded-growth of metallic anisotropic nanoparticles. **O.A.** contributed by performing the dark-field spectroscopy

measurements, alongside with the finite-difference time domain simulations of the optical response of single T- and L-shaped nanoparticles. T.B. and A.J. provided integration and electrical measurements of the structures. T.A.F.K., A.E. and R.S. developed the concept, assisted in the manuscript writing process and were involved in the scientific discussions. R.S. supervised the project.

Exploring Plasmonic Resonances Toward "Large-Scale" Flexible Optical Sensors with Deformation Stability

Anik Kumar Ghosh[1], Swagato Sarkar[1], Lisa Julia Nebel[2], Olha Aftenieva[1], Vaibhav Gupta[1], Oliver Sander[2], Amit Das[1], Joby Joseph[3], Sven Wießner[1,4], Tobias A. F. König[1,5,*], Andreas Fery[1,6,*]

1. Leibniz-Institut für Polymerforschung Dresden e.V., Institute of Physical Chemistry and Polymer Physics, Hohe Str. 6, D-01069 Dresden, Germany

2. Institut für Numerische Mathematik, Technische Universität Dresden, Zellescher Weg 12–14, 01069 Dresden, Germany

3. Photonics Research Laboratory, Department of Physics, Indian Institute of Technology Delhi, New Delhi, 110016, India

4. Chair for Elastomeric Materials, Institute of Materials Science, Technische Universität Dresden, 01069 Dresden, Germany

5. Center for Advancing Electronics Dresden (cfaed), Technische Universität Dresden, Helmholtzstraße 18, 01069 Dresden, Germany

6. Chair for Physical Chemistry of Polymeric Materials, Technical University Dresden, Mommsenstr. 4, D-01062 Dresden, Germany

* Corresponding author: koenig@ipfdd.de, fery@ipfdd.de

T.A.F.K., and A.F. developed the concept, assisted in the manuscript writing process and were involved in the scientific discussions. A.D. and A.F. co-supervised the project.

Plasmonic Charge Transfers in Large-Scale Metallic and Colloidal Photonic Crystal Slabs

Swagato Sarkar[1,2], Vaibhav Gupta[1], Takuya Tsuda[1], Jeetendra Gour[1,2], Arvind Singh[2], Olha Aftenieva[1], Anja M. Steiner[1], Marisa Hoffmann[1], Sunil Kumar[2], Andreas Fery[1,3], Joby Joseph[2], Tobias A.F. König[1,3,*]

1. Leibniz-Institut für Polymerforschung Dresden e.V. (IPF), Institute for Physical Chemistry and Polymer Physics, Hohe Str. 6, 01069 Dresden, Germany

2. Department of Physics, Indian Institute of Technology Delhi, New Delhi, 110016, India

3. Cluster of Excellence Center for Advancing Electronics Dresden (cfaed), Technische Universität Dresden, 01062 Dresden, Germany

* Corresponding author: koenig@ipfdd.de

High Yield Synthesis of Water-Processable Donor: Acceptor Janus Nanoparticles with Tuned Internal Morphology and Highly Efficient Charge Separation/Transfer

Yixuan Du[1,2], Yue Li[1], Olha Aftenieva[1], Takuya Tsuda[1], Petr Formanek[1], Tobias A. F. König[1,3], and Alla Synytska[1,2,4,*]

1. Leibniz-Institut für Polymerforschung Dresden e.V. Hohe Str. 6, 01069 Dresden, Germany

2. Fakultat Mathematik und Naturwissenschaften, Technische Universität Dresden Mommsenstrasse 4, 01064 Dresden, Germany

3. Center for Advancing Electronics Dresden (cfaed), Technische Universität Dresden 01062 Dresden, Germany

4. Bayerisches Polymerinstitut – BPI Universität Bayreuth Universitätsstraße 30, 95440 Bayreuth, Germany

* Corresponding author: Alla.Synytska@uni-bayreuth.de

List of publications

1. Gupta, V., Sarkar, S., **Aftenieva, O.**, Tsuda, T., Kumar, L., Schletz, D., Schultz, J., Kiriy, A., Fery, A., Vogel, N., König, T. A. F., Nanoimprint Lithography Facilitated Plasmonic-Photonic Coupling for Enhanced Photoconductivity and Photocatalysis. *Adv. Funct. Mater.* 2021, 31, 2105054.

2. **Aftenieva, O.,** Schletz, D., Meyer, A., Kühne, T., Schmalzriedt, S., Niethammer, M. and König, T.A.F., Development of a Teaching Platform about Plasmonics Based on the Color Perception of Colloidal Gold. *J. Chem. Educ.* 2021, 98, 8, 2566–2573

3. Ye, J., **Aftenieva, O.**, Bayrak, T., Jain, A., König, T. A. F., Erbe, A., Seidel, R., Complex Metal Nanostructures with Programmable Shapes from Simple DNA Building Blocks. *Adv. Mater.* 2021, 33, 2100381.

4. Ghosh, A. K., Sarkar, S., Nebel, L. J., **Aftenieva, O.**, Gupta, V., Sander, O., Das, A., Joseph, J., Wießner, S., König, T. A. F., Fery, A., Exploring Plasmonic Resonances Toward "Large-Scale" Flexible Optical Sensors with Deformation Stability. *Adv. Funct. Mater.* 2021, 31, 2101959.

5. Sarkar, S., Gupta, V., Tsuda, T., Gour, J., Singh, A., **Aftenieva, O.**, Steiner, A. M., Hoffmann, M., Kumar, S., Fery, A., Joseph, J., König, T. A. F., Plasmonic Charge Transfers in Large-Scale Metallic and Colloidal Photonic Crystal Slabs. *Adv. Funct. Mater.* 2021, 31, 2011099.

6. **Aftenieva, O.**, Schnepf, M., Mehlhorn, B., König, T. A. F., Tunable Circular Dichroism by Photoluminescent Moiré Gratings. *Adv. Optical Mater.* 2021, 9, 2001280.

7. Du, Y., Li, Y., **Aftenieva, O.**, Tsuda, T., Formanek, P., König, T. A. F., Synytska, A., High Yield Synthesis of Water-Processable Donor:Acceptor Janus Nanoparticles with Tuned Internal Morphology and Highly Efficient Charge Separation/Transfer. *Adv. Optical Mater.* 2022, 10, 2101922.

Acknowledgment

In this last part of the thesis, but not the least important one, I would like to thank everyone, who accompanied and helped in achieving this milestone. Even though the one or two pages here do not allow me to mention everyone personally, I am very grateful to all, who directly or partially took part in my doctoral studies. Thanks to you, these years of PhD became an extremely valuable part of my life, full of new knowledge, experiences, and friendship.

My first and foremost goes to my Doktorvater PD Dr. Tobias A. F. König for taking me as a PhD student and being the best supervisor I could imagine. You always gave me freedom in making decisions and, at the same time, carefully guided me through all pitfalls that a PhD student could encounter. Thank you for always finding time for scientific discussions, sharing motivation and passing your knowledge to me, and teaching me how to pass it to someone else. I am immensely grateful for you being patient, kind, and very supportive in times when the morale was low. Thank you for reminding me about work-life balance and inspiring me to transfer the lab skills into daily life, sharing the art of soap making and soar-dough baking.

I also want to express my cordial gratitude to Prof. Dr. Andreas Fery for providing thoughtful guidance throughout my scientific career and showing trust in me. I appreciate very much the friendly and respectful working atmosphere you created at IPF, uniting such various research directions and people's characters. Thank you for underlining the importance of cooperation and always supporting the team spirit. I am also very much thankful for the immense support you provided when it was so important to feel that I do not stand alone.

Further, I would like to thank all my current and former colleagues, who accompanied me along with my PhD: without you, none of the projects would work, as they did! My special thanks go to Vaibhav and Swagato for great teamwork and discussions: scientific and beyond. Thank you, Patrick and Martin - for sharing your great practical experience in self-assembly and plasmonics and always finding time for my questions; Yannick, Max, and Fabi – for standing at the very beginning of my PhD and helping on the way. Big thanks go to Marisa, Daniel, Labeesh, Anik, Ruosong, Dr. Petr Formanek, Dr. Soosang Chae, and Dr. Andriy Horechiy for fruitful cooperative work, and Dr. Günter K. Auernhammer for extremely valuable presentation tips. Thank you, Anja,

Bernhard, Inga, and Max for keeping the spirit of good old PhD traditions and transmitting them further; Ye and Charlene for your scientific and career advice. Thank you, Shayan - for bringing some festival mood, Christian - for all the nice coffee and lunch breaks together, and Quinn - for being a great part of our running, self-assembled team.

Many thanks to Janett Forkel and Ulrike Pratourius for always helping me with the organizational work and encouraging me in speaking German. I am also very grateful to Ben, my keeping me company in our office on the 4th floor and providing valuable linguistic proofreading support.

Thanks to all my dear friends, especially Andrii, Ksenia, Sasha, Jean, Till, Peter, Ksusha and Valya, I had an irreplaceable moral support, no matter what came in the way. I am also very grateful to my family, who inspired me to take this path and never judged my decisions, and, in particular, to my uncle, who always was an exemplar scientist to me. Ebenso danke ich die Familie Rotth für die Unterstützung und das Gefühl von Zuhause und Gemütlichkeit, und zu guter Letzt – meinem Partner Christian – für deine Liebe, Mitdenken, und dafür, dass wir es alles gemeinsam durchgestanden haben.

References

[1]   S. Mohan Bhagyaraj, O. S. Oluwafemi, in *Nanotechnology: The Science of the Invisible* (Eds.: S. Mohan Bhagyaraj, O.S. Oluwafemi, N. Kalarikkal, S. Thomas), Woodhead Publishing, **2018**.

[2]   J. L. Paris, M. Vallet-Regí, in *Fundamentals of Nanoparticles: Nanostructures for Imaging, Medical Diagnostics and Therapy* (Eds.: A. Barhoum, A.S. Hamdy Makhlouf), Elsevier, **2018**.

[3]   M. Volokh, T. Mokari, *Nanoscale Adv.* **2020**, *2*, 930.

[4]   M. Loos, in *Carbon Nanotube Reinforced Composites* (Ed.: M. Loos), William Andrew Publishing, Oxford, **2015**, pp. 1–36.

[5]   P. Mulvaney, *Langmuir* **1996**, *12*, 788.

[6]   X. Huang, S. Neretina, M. A. El-Sayed, *Adv. Mater.* **2009**, *21*, 4880.

[7]   P. Scherrer, in *Kolloidchemie Ein Lehrbuch: Bestimmung der inneren Struktur und der Größe von Kolloidteilchen mittels Röntgenstrahlen* (Ed.: R. Zsigmondy), Springer, Berlin, Heidelberg, **1912**.

[8]   C. Sönnichsen, W. Fritzsche, in *100 Years of Nanoscience with the Ultramicroscope: The Work of Richard Zsigmondy Introduced by Carsten Sönnichsen and Wolfgang Fritzsche*, Shaker, Aachen, **2007**.

[9]   M. N. Muniz, M. T. Oliver-Hoyo, *Chem. Educ. Res. Pract.* **2014**, *15*, 807.

[10]   G. Habibullah, J. Viktorova, T. Ruml, *Nanoscale Res. Lett.* **2021**, *16*, 47.

[11]   J. A. Jenkins, T. J. Wax, J. Zhao, *J. Chem. Educ.* **2017**, *94*, 1090.

[12]   A. M. Steiner, M. Mayer, D. Schletz, D. Wolf, P. Formanek, R. Hübner, M. Dulle, S. Förster, T. A. F. König, A. Fery, *Chem. Mater.* **2019**, *31*, 2822.

[13]   J. E. Millstone, W. Wei, M. R. Jones, H. Yoo, C. A. Mirkin, *Nano Lett.* **2008**, *8*, 2526.

[14]   Q. Yao, X. Yuan, V. Fung, Y. Yu, D. T. Leong, D. Jiang, J. Xie, *Nat Commun* **2017**, *8*, 927.

[15]   M. Mayer, A. M. Steiner, F. Röder, P. Formanek, T. A. F. König, A. Fery, *Angew. Chem. Int. Ed.* **2017**, *56*, 15866.

[16]   A. M. Steiner, F. Lissel, A. Fery, J. Lauth, M. Scheele, *Angewandte Chemie International Edition* **2021**, *60*, 1152.

[17]   C. J. Murphy, T. K. Sau, A. M. Gole, C. J. Orendorff, J. Gao, L. Gou, S. E. Hunyadi, T. Li, *J. Phys. Chem. B* **2005**, *109*, 13857.

[18]   T. K. Sau, A. L. Rogach, F. Jäckel, T. A. Klar, J. Feldmann, *Adv. Mater.* **2010**, *22*, 1805.

[19]   M. Tréguer-Delapierre, J. Majimel, S. Mornet, E. Duguet, S. Ravaine, *Gold Bull* **2008**, *41*, 195.

[20]   M. A. Reed, R. T. Bate, K. Bradshaw, W. M. Duncan, W. R. Frensley, J. W. Lee, H. D. Shih, *J. Vac. Sci. Technol.* **1986**, *4*, 358.

[21]   A. I. Ekimov, Al. L. Efros, A. A. Onushchenko, *Solid State Commun.* **1985**, *56*, 921.

[22]   L. Brus, *J. Phys. Chem.* **1986**, *90*, 2555.

[23]   T. Kippeny, L. A. Swafford, S. J. Rosenthal, *J. Chem. Educ.* **2002**, *79*, 1094.

[24]   A. Jabłoński, *Z. Physik* **1935**, *94*, 38.

[25]   D. C. Agrawal, in *Introduction to Nanoscience and Nanomaterials: Semiconductor Quantum Dots*, WORLD SCIENTIFIC, **2012**.

[26]   Al. L. Efros, A. V. Rodina, *Phys. Rev. B* **1993**, *47*, 10005.

[27]   A. Valizadeh, H. Mikaeili, M. Samiei, S. M. Farkhani, N. Zarghami, M. kouhi, A. Akbarzadeh, S. Davaran, *Nanoscale Res. Lett.* **2012**, *7*, 480.

[28]   P. L. Saldanha, V. Lesnyak, L. Manna, *Nano Today* **2017**, *12*, 46.

[29]   Global Quantum Dots (QD) Market Size & Industry Analysis, https://www.alliedmarketresearch.com/quantum-dots-market, accessed: May, 2022.

[30]   F. Zhang, D. Yi, H. Sun, H. Zhang, *J. Nanosci. Nanotechnol.* **2014**, *14*, 1409.

[31]   D. Mo, L. Hu, G. Zeng, G. Chen, J. Wan, Z. Yu, Z. Huang, K. He, C. Zhang, M. Cheng, *Appl Microbiol Biotechnol* **2017**, *101*, 2713.

[32]   P. L. Saldanha, R. Brescia, M. Prato, H. Li, M. Povia, L. Manna, V. Lesnyak, *Chem. Mater.* **2014**, *26*, 1442.

[33]   Q. A. Akkerman, A. Genovese, C. George, M. Prato, I. Moreels, A. Casu, S. Marras, A. Curcio, A. Scarpellini, T. Pellegrino, L. Manna, V. Lesnyak, *ACS Nano* **2015**, *9*, 521.

[34]   A. Dey, J. Ye, A. De, E. Debroye, S. K. Ha, E. Bladt, A. S. Kshirsagar, Z. Wang, J. Yin, Y. Wang, L. N. Quan, F. Yan, M. Gao, X. Li, J. Shamsi, T. Debnath, M. Cao, M. A. Scheel, S. Kumar, J. A. Steele, M. Gerhard, L. Chouhan, K. Xu, X. Wu, Y. Li, Y. Zhang, A. Dutta, C. Han, I. Vincon, A. L. Rogach, A. Nag, A. Samanta, B. A. Korgel, C.-J. Shih, D. R. Gamelin, D. H. Son, H. Zeng, H. Zhong, H. Sun, H. V. Demir, I. G. Scheblykin, I. Mora-Seró, J. K. Stolarczyk, J. Z. Zhang, J. Feldmann, J. Hofkens, J. M. Luther, J. Pérez-Prieto, L. Li, L. Manna, M. I.

Bodnarchuk, M. V. Kovalenko, M. B. J. Roeffaers, N. Pradhan, O. F. Mohammed, O. M. Bakr, P. Yang, P. Müller-Buschbaum, P. V. Kamat, Q. Bao, Q. Zhang, R. Krahne, R. E. Galian, S. D. Stranks, S. Bals, V. Biju, W. A. Tisdale, Y. Yan, R. L. Z. Hoye, L. Polavarapu, *ACS Nano* **2021**, *15*, 10775.

[35]   H. Ebe, Y.-K. Wang, N. Shinotsuka, Y.-H. Cheng, M. Uwano, R. Suzuki, Y. Dong, D. Ma, S. Lee, T. Chiba, E. H. Sargent, J. Kido, *ACS Appl. Mater. Interfaces* **2022**, *14*, 17691.

[36]   H. Li, H.-J. Xiao, T.-S. Zhu, H.-C. Xuan, M. Li, *J. Phys. Chem. C* **2015**, *119*, 12002.

[37]   B. Terlan, A. A. Levin, F. Börrnert, F. Simon, M. Oschatz, M. Schmidt, R. Cardoso-Gil, T. Lorenz, I. A. Baburin, J.-O. Joswig, A. Eychmüller, *Chem. Mater.* **2015**, *27*, 5106.

[38]   M. Morán-Pedroso, A. Rubino, M. E. Calvo, J. P. Espinós, J. F. Galisteo-López, H. Míguez, *Adv. Opt. Mater.* **2021**, *9*, 2100605.

[39]   S. K. Panda, S. G. Hickey, C. Waurisch, A. Eychmüller, *J. Mater. Chem.* **2011**, *21*, 11550.

[40]   T. Otto, M. Müller, P. Mundra, V. Lesnyak, H. V. Demir, N. Gaponik, A. Eychmüller, *Nano Lett.* **2012**, *12*, 5348.

[41]   F. Corsini, G. Griffini, *J. Phys. Energy* **2020**, *2*, 031002.

[42]   H. Y. Kim, D.-E. Yoon, J. Jang, D. Lee, G.-M. Choi, J. H. Chang, J. Y. Lee, D. C. Lee, B.-S. Bae, *J. Am. Chem. Soc.* **2016**, *138*, 16478.

[43]   K. L. Kelly, E. Coronado, L. L. Zhao, G. C. Schatz, *J. Phys. Chem. B* **2003**, *107*, 668.

[44]   V. G. Kravets, A. V. Kabashin, W. L. Barnes, A. N. Grigorenko, *Chem. Rev.* **2018**, *118*, 5912.

[45]   S. Song, X. Ma, M. Pu, X. Li, K. Liu, P. Gao, Z. Zhao, Y. Wang, C. Wang, X. Luo, *Adv. Opt. Mater.* **2017**, *5*, 1600829.

[46]   L. Liu, R. Aleisa, Y. Zhang, J. Feng, Y. Zheng, Y. Yin, W. Wang, *Angew. Chem. Int. Ed.* **2019**, *58*, 16307.

[47]   J. M. Romo-Herrera, R. A. Alvarez-Puebla, L. M. Liz-Marzán, *Nanoscale* **2011**, *3*, 1304.

[48]   P. Nordlander, C. Oubre, E. Prodan, K. Li, M. I. Stockman, *Nano Lett.* **2004**, *4*, 899.

[49]   M. J. Rozin, D. A. Rosen, T. J. Dill, A. R. Tao, *Nat Commun* **2015**, *6*, 7325.

[50] M. Mayer, M. J. Schnepf, T. A. F. König, A. Fery, *Adv. Opt. Mater.* **2019**, *7*, 1800564.

[51] A. V. Kildishev, A. Boltasseva, V. M. Shalaev, *Science* **2013**, *339*, 1232009.

[52] P. K. Jain, W. Huang, M. A. El-Sayed, *Nano Lett.* **2007**, *7*, 2080.

[53] A. L. Koh, K. Bao, I. Khan, W. E. Smith, G. Kothleitner, P. Nordlander, S. A. Maier, D. W. McComb, *ACS Nano* **2009**, *3*, 3015.

[54] N. J. Halas, S. Lal, W.-S. Chang, S. Link, P. Nordlander, *Chem. Rev.* **2011**, *111*, 3913.

[55] E. Prodan, C. Radloff, N. J. Halas, P. Nordlander, *Science* **2003**, *302*, 419.

[56] N. Meinzer, W. L. Barnes, I. R. Hooper, *Nat. Photon.* **2014**, *8*, 889.

[57] S. K. Ghosh, T. Pal, *Chem. Rev.* **2007**, *107*, 4797.

[58] C. Cherqui, M. R. Bourgeois, D. Wang, G. C. Schatz, *Acc. Chem. Res.* **2019**, *52*, 2548.

[59] W. Zhou, M. Dridi, J. Y. Suh, C. H. Kim, D. T. Co, M. R. Wasielewski, G. C. Schatz, T. W. Odom, *Nat. Nanotechnol.* **2013**, *8*, 506.

[60] S. R. K. Rodriguez, A. Abass, B. Maes, O. T. A. Janssen, G. Vecchi, J. Gómez Rivas, *Phys. Rev. X* **2011**, *1*, 021019.

[61] K. Volk, J. P. S. Fitzgerald, P. Ruckdeschel, M. Retsch, T. A. F. König, M. Karg, *Adv. Opt. Mater.* **2017**, *5*, 1600971.

[62] F. Wang, Y. R. Shen, *Phys. Rev. Lett.* **2006**, *97*, 206806.

[63] B. Auguié, W. L. Barnes, *Phys. Rev. Lett.* **2008**, *101*, 143902.

[64] V. G. Kravets, F. Schedin, A. N. Grigorenko, *Phys. Rev. Lett.* **2008**, *101*, 087403.

[65] M. F. Limonov, M. V. Rybin, A. N. Poddubny, Y. S. Kivshar, *Nat. Photon.* **2017**, *11*, 543.

[66] V. Gupta, P. T. Probst, F. R. Goßler, A. M. Steiner, J. Schubert, Y. Brasse, T. A. F. König, A. Fery, *ACS Appl. Mater. Interfaces* **2019**, *11*, 28189.

[67] E. Ponomareva, K. Volk, P. Mulvaney, M. Karg, *Langmuir* **2020**, *36*, 13601.

[68] K. Volk, J. P. S. Fitzgerald, M. Retsch, M. Karg, *Adv. Mater.* **2015**, *27*, 7332.

[69] K. Volk, F. Deißenbeck, S. Mandal, H. Löwen, M. Karg, *Phys. Chem. Chem. Phys.* **2019**, *21*, 19153.

[70] W. Gao, H. M. Leung, Y. Li, H. Chen, W. Y. Tam, *J. Opt.* **2011**, *13*, 115101.

[71] J.-G. Yun, S.-J. Kim, H. Yun, K. Lee, J. Sung, J. Kim, Y. Lee, B. Lee, *Opt. Express* **2017**, *25*, 14260.

[72] P. T. Probst, M. Mayer, V. Gupta, A. M. Steiner, Z. Zhou, G. K. Auernhammer, T. A. F. König, A. Fery, *Nat. Mater.* **2021**, *20*, 1024.

[73] S. Sarkar, V. Gupta, M. Kumar, J. Schubert, P. T. Probst, J. Joseph, T. A. F. König, *ACS Appl. Mater. Interfaces* **2019**, *11*, 13752.

[74] J. Hu, C. R. Menyuk, *Adv. Opt. Photon., AOP* **2009**, *1*, 58.

[75] M. W. Klein, T. Tritschler, M. Wegener, S. Linden, *Phys. Rev. B* **2005**, *72*, 115113.

[76] A. Christ, S. G. Tikhodeev, N. A. Gippius, J. Kuhl, H. Giessen, *Phys. Rev. Lett.* **2003**, *91*, 183901.

[77] F. Laux, N. Bonod, D. Gérard, *J. Phys. Chem. C* **2017**, *121*, 13280.

[78] S. R. K. Rodriguez, S. Murai, M. A. Verschuuren, J. G. Rivas, *Phys. Rev. Lett.* **2012**, *109*, 166803.

[79] E. Sakat, G. Vincent, P. Ghenuche, N. Bardou, S. Collin, F. Pardo, J.-L. Pelouard, R. Haïdar, *Opt. Lett., OL* **2011**, *36*, 3054.

[80] T.-H. Kim, K.-S. Cho, E. K. Lee, S. J. Lee, J. Chae, J. W. Kim, D. H. Kim, J.-Y. Kwon, G. Amaratunga, S. Y. Lee, B. L. Choi, Y. Kuk, J. M. Kim, K. Kim, *Nat. Photon.* **2011**, *5*, 176.

[81] E. Jang, S. Jun, H. Jang, J. Lim, B. Kim, Y. Kim, *Adv. Mater.* **2010**, *22*, 3076.

[82] P. O. Anikeeva, J. E. Halpert, M. G. Bawendi, V. Bulović, *Nano Lett.* **2009**, *9*, 2532.

[83] Y. Shirasaki, G. J. Supran, M. G. Bawendi, V. Bulović, *Nat. Photon.* **2013**, *7*, 13.

[84] V. L. Colvin, M. C. Schlamp, A. P. Alivisatos, *Nature* **1994**, *370*, 354.

[85] F. Liu, Y. Zhang, C. Ding, S. Kobayashi, T. Izuishi, N. Nakazawa, T. Toyoda, T. Ohta, S. Hayase, T. Minemoto, K. Yoshino, S. Dai, Q. Shen, *ACS Nano* **2017**, *11*, 10373.

[86] M. Nasilowski, P. Spinicelli, G. Patriarche, B. Dubertret, *Nano Lett.* **2015**, *15*, 3953.

[87] F. Prins, D. K. Kim, J. Cui, E. De Leo, L. L. Spiegel, K. M. McPeak, D. J. Norris, *Nano Lett.* **2017**, *17*, 1319.

[88] E.-P. Jang, J.-H. Jo, M.-S. Kim, S.-Y. Yoon, S.-W. Lim, J. Kim, H. Yang, *RSC Adv.* **2018**, *8*, 10057.

[89] R. Yalla, F. Le Kien, M. Morinaga, K. Hakuta, *Phys. Rev. Lett.* **2012**, *109*, 063602.

[90] A. Kress, F. Hofbauer, N. Reinelt, M. Kaniber, H. J. Krenner, R. Meyer, G. Böhm, J. J. Finley, *Phys. Rev. B* **2005**, *71*, 241304.

[91] N. Ganesh, W. Zhang, P. C. Mathias, E. Chow, J. a. N. T. Soares, V. Malyarchuk, A. D. Smith, B. T. Cunningham, *Nat. Nanotechnol.* **2007**, *2*, 515.

[92]   G. Popescu, *Principles of Biophotonics, Volume 2*, IOP Publishing, **2020**.

[93]   L. D. Landau, E. M. Lifshitz, *Quantum Electrodynamics*, Pergamon Press, Oxford, **1983**.

[94]   P. W. Milonni, J. H. Eberly, *Laser Physics*, Wiley, Hoboken, NJ, **2010**.

[95]   I. D. W. Samuel, E. B. Namdas, G. A. Turnbull, *Nat. Photon.* **2009**, *3*, 546.

[96]   V. Bonal, J. A. Quintana, J. M. Villalvilla, P. G. Boj, M. A. Díaz-García, *Sci Rep* **2019**, *9*, 11159.

[97]   Y.-S. Park, J. Roh, B. T. Diroll, R. D. Schaller, V. I. Klimov, *Nat Rev Mater* **2021**, *6*, 382.

[98]   S. Reineke, M. A. Baldo, *Sci Rep* **2014**, *4*, 3797.

[99]   C. Qin, A. S. D. Sandanayaka, C. Zhao, T. Matsushima, D. Zhang, T. Fujihara, C. Adachi, *Nature* **2020**, *585*, 53.

[100] J. S. Bendall, M. Paderi, F. Ghigliotti, N. Li Pira, V. Lambertini, V. Lesnyak, N. Gaponik, G. Visimberga, A. Eychmüller, C. M. S. Torres, M. E. Welland, C. Gieck, L. Marchese, *Adv. Funct. Mater.* **2010**, *20*, 3298.

[101] M. a Wood, *J R Soc Interface* **2007**, *4*, 1.

[102] S. Zhang, C. I. Pelligra, X. Feng, C. O. Osuji, *Adv. Mater.* **2018**, *30*, 1705794.

[103] N. Vogel, M. Retsch, C.-A. Fustin, A. del Campo, U. Jonas, *Chem. Rev.* **2015**, *115*, 6265.

[104] S. Julin, S. Nummelin, M. A. Kostiainen, V. Linko, *J Nanopart Res* **2018**, *20*, 119.

[105] M. Grzelczak, J. Vermant, E. M. Furst, L. M. Liz-Marzán, *ACS Nano* **2010**, *4*, 3591.

[106] Y. Brasse, V. Gupta, H. C. T. Schollbach, M. Karg, T. A. F. König, A. Fery, *Adv. Mater. Interfaces* **2020**, *7*, 1901678.

[107] M. E. J. Hummel, C. Stelling, B. A. F. Kopera, F. A. Nutz, M. Karg, M. Retsch, S. Förster, *Langmuir* **2019**, *35*, 973.

[108] K. M. Gattás-Asfura, C. A. Constantine, M. J. Lynn, D. A. Thimann, X. Ji, R. M. Leblanc, *J. Am. Chem. Soc.* **2005**, *127*, 14640.

[109] S. Oh, M. Yang, S. Kang, S.-H. Chung, J. Bouffard, S. Hong, S.-J. Park, *ACS Appl. Mater. Interfaces* **2019**, *11*, 28538.

[110] O. Erdem, S. Foroutan, N. Gheshlaghi, B. Guzelturk, Y. Altintas, H. V. Demir, *Nano Lett.* **2020**, *20*, 6459.

[111] M. Zorn, S. Meuer, M. N. Tahir, Y. Khalavka, C. Sönnichsen, W. Tremel, R. Zentel, *J. Mater. Chem.* **2008**, *18*, 3050.

[112] Y. Aniskevich, A. Radchanka, A. Antanovich, A. Prudnikau, M. T. Quick, A. W. Achtstein, J. H. Jo, G. Ragoisha, M. Artemyev, E. Streltsov, *ACS Appl. Nano Mater.* **2021**, *4*, 6974.

[113] M. T. Byrne, Y. K. Gun'ko, *Adv. Mater.* **2010**, *22*, 1672.

[114] C. Preger, M. Josefsson, R. Westerström, M. E. Messing, *Nanotechnology* **2021**, *32*, 195603.

[115] B. B. Patel, Y. Diao, *Nanotechnology* **2017**, *29*, 044004.

[116] S. Zhang, P. W. Majewski, G. Keskar, L. D. Pfefferle, C. O. Osuji, *Langmuir* **2011**, *27*, 11616.

[117] C. Zheng, X. Xu, F. He, L. Li, B. Wu, G. Yu, Y. Liu, *Langmuir* **2010**, *26*, 16730.

[118] H. Uchiyama, D. Shimaoka, H. Kozuka, *Soft Matter* **2012**, *8*, 11318.

[119] L. Hu, M. Chen, X. Fang, L. Wu, *Chem. Soc. Rev.* **2012**, *41*, 1350.

[120] V. Flauraud, M. Mastrangeli, G. D. Bernasconi, J. Butet, D. T. L. Alexander, E. Shahrabi, O. J. F. Martin, J. Brugger, *Nat. Nanotechnol.* **2017**, *12*, 73.

[121] X. Shen, C.-M. Ho, T.-S. Wong, *J. Phys. Chem. B* **2010**, *114*, 5269.

[122] Y. Wu, N. Dong, S. Fu, J. D. Fowlkes, L. Kondic, M. A. Vincenti, D. de Ceglia, P. D. Rack, *ACS Appl. Mater. Interfaces* **2014**, *6*, 5835.

[123] Y. Li, W. Zhang, J. Hu, Y. Wang, X. Feng, W. Du, M. Guo, B.-F. Liu, *Adv. Funct. Mater.* **2017**, *27*, 1606045.

[124] Y. Yin, Y. Lu, B. Gates, Y. Xia, *J. Am. Chem. Soc.* **2001**, *123*, 8718.

[125] R. van Dommelen, P. Fanzio, L. Sasso, *Adv. Colloid Interface Sci.* **2018**, *251*, 97.

[126] M. K. Chaudhury, G. M. Whitesides, *Science* **1992**, *256*, 1539.

[127] F. Zhang, H. Zhong, C. Chen, X. Wu, X. Hu, H. Huang, J. Han, B. Zou, Y. Dong, *ACS Nano* **2015**, *9*, 4533.

[128] H.-J. Butt, in *Physics and Chemistry of Interfaces: Surface Forces*, John Wiley & Sons, Ltd, **2003**.

[129] C. Hanske, M. Tebbe, C. Kuttner, V. Bieber, V. V. Tsukruk, M. Chanana, T. A. F. König, A. Fery, *Nano Lett.* **2014**, *14*, 6863.

[130] H. Chang, K. Min, M. Lee, M. Kang, Y. Park, K.-S. Cho, Y.-G. Roh, S. W. Hwang, H. Jeon, *Nanoscale* **2016**, *8*, 6571.

[131] C. Dang, J. Lee, K. Roh, H. Kim, S. Ahn, H. Jeon, C. Breen, J. S. Steckel, S. Coe-Sullivan, A. Nurmikko, *Appl. Phys. Lett.* **2013**, *103*, 171104.

[132] G. L. Whitworth, M. Dalmases, N. Taghipour, G. Konstantatos, *Nat. Photon.* **2021**, *15*, 738.

[133] S. Ni, J. Leemann, I. Buttinoni, L. Isa, H. Wolf, *Sci. Adv.* **2016**, *2*, e1501779.

[134] N. J. Greybush, I. Liberal, L. Malassis, J. M. Kikkawa, N. Engheta, C. B. Murray, C. R. Kagan, *ACS Nano* **2017**, *11*, 2917.

[135] T. Kraus, L. Malaquin, H. Schmid, W. Riess, N. D. Spencer, H. Wolf, *Nat. Nanotechnol.* **2007**, *2*, 570.

[136] L. Malaquin, T. Kraus, H. Schmid, E. Delamarche, H. Wolf, *Langmuir* **2007**, *23*, 11513.

[137] A. Rey, G. Billardon, E. Lörtscher, K. Moth-Poulsen, N. Stuhr-Hansen, H. Wolf, T. Bjørnholm, A. Stemmer, H. Riel, *Nanoscale* **2013**, *5*, 8680.

[138] Y. Zhou, X. Zhou, D. J. Park, K. Torabi, K. A. Brown, M. R. Jones, C. Zhang, G. C. Schatz, C. A. Mirkin, *Nano Lett.* **2014**, *14*, 2157.

[139] M. Juodėnas, T. Tamulevičius, J. Henzie, D. Erts, S. Tamulevičius, *ACS Nano* **2019**, *13*, 9038.

[140] R. Pioli, M. A. Fernandez-Rodriguez, F. Grillo, L. Alvarez, R. Stocker, L. Isa, E. Secchi, *Lab Chip* **2021**, *21*, 888.

[141] F. Timpu, N. R. Hendricks, M. Petrov, S. Ni, C. Renaut, H. Wolf, L. Isa, Y. Kivshar, R. Grange, *Nano Lett.* **2017**, *17*, 5381.

[142] S. Ni, H. Wolf, L. Isa, *Langmuir* **2018**, *34*, 2481.

[143] H. J. Shulevitz, T.-Y. Huang, J. Xu, S. J. Neuhaus, R. N. Patel, Y. C. Choi, L. C. Bassett, C. R. Kagan, *ACS Nano* **2022**.

[144] I. Mesquita, L. Andrade, A. Mendes, *Sol Energy* **2020**, *199*, 474.

[145] A. Kessel, C. Frydendahl, S. R. K. C. Indukuri, N. Mazurski, P. Arora, U. Levy, *Adv. Opt. Mater.* **2020**, *8*, 2001627.

[146] L. Scarabelli, D. Vila-Liarte, A. Mihi, L. M. Liz-Marzán, *Acc. Mater. Res.* **2021**, *2*, 816.

[147] C. Hanske, G. González-Rubio, C. Hamon, P. Formentín, E. Modin, A. Chuvilin, A. Guerrero-Martínez, L. F. Marsal, L. M. Liz-Marzán, *J. Phys. Chem. C* **2017**, *121*, 10899.

[148] A. Schweikart, A. Fortini, A. Wittemann, M. Schmidt, A. Fery, *Soft Matter* **2010**, *6*, 5860.

[149] M. Tebbe, S. Lentz, L. Guerrini, A. Fery, R. A. Alvarez-Puebla, N. Pazos-Perez, *Nanoscale* **2016**, *8*, 12702.

[150] H. Agrawal, E. C. Garnett, *ACS Nano* **2020**, *14*, 11009.

[151] Y. Wang, P. Wang, X. Zhou, C. Li, H. Li, X. Hu, F. Li, X. Liu, M. Li, Y. Song, *Adv. Energy Mater* **2018**, *8*, 1702960.

[152] Z. Zhang, Z. Wang, Z. Xu, Q. Gao, P. Liu, J. Ren, M. Li, C. Zhou, Q. Liao, H. Fu, *Adv. Opt. Mater.* **2018**, *6*, 1800219.

[153] M. Modaresialam, Z. Chehadi, T. Bottein, M. Abbarchi, D. Grosso, *Chem. Mater.* **2021**, *33*, 5464.

[154] D. Qin, Y. Xia, G. M. Whitesides, *Nat Protoc* **2010**, *5*, 491.

[155] G. Dibrov, in *Encyclopedia of Membranes: Polydimethylsiloxane Membrane* (Eds.: E. Drioli, L. Giorno), Springer, Berlin, Heidelberg, **2016**.

[156] E. Delamarche, H. Schmid, B. Michel, H. Biebuyck, *Adv. Mater.* **1997**, *9*, 741.

[157] J.-H. Seo, J. H. Park, S.-I. Kim, B. J. Park, Z. Ma, J. Choi, B.-K. Ju, *J. Nanosci. Nanotechnol.* **2014**, *14*, 1521.

[158] I. Freestone, N. Meeks, M. Sax, C. Higgitt, *Gold Bull* **2007**, *40*, 270.

[159] L. Scarabelli, *Pure Appl. Chem.* **2018**, *90*, 1393.

[160] E. Hutter, J. H. Fendler, *Adv. Mater.* **2004**, *16*, 1685.

[161] M. Karg, T. A. F. König, M. Retsch, C. Stelling, P. M. Reichstein, T. Honold, M. Thelakkat, A. Fery, *Mater. Today* **2015**, *18*, 185.

[162] A. V. Markin, N. E. Markina, *J. Chem. Educ.* **2019**, *96*, 1438.

[163] M. G. Lagorio, *J. Chem. Educ.* **2004**, *81*, 1607.

[164] J. Turkevich, P. C. Stevenson, J. Hillier, *Discuss. Faraday Soc.* **1951**, *11*, 55.

[165] C. Ziegler, A. Eychmüller, *J. Phys. Chem. C* **2011**, *115*, 4502.

[166] C. F. Bohren, D. R. Huffman, in *Absorption and Scattering of Light by Small Particles: Absorption and Scattering by a Sphere*, John Wiley & Sons, Ltd, **1998**, pp. 82–129.

[167] C. Sonnichsen, W. Fritzsche, Eds. , *100 Years of Nanoscience with the Ultramicroscope : The Work of Richard Zsigmondy Introduced by Carsten Sonnichsen and Wolfgang Fritzsche*, Shaker Verlag GmbH, Germany, Aachen, Germany, **2007**.

[168] G. Mie, *Annalen der Physik* **1908**, *330*, 377.

[169] M. R. Pointer, R. W. G. Hunt, in *Measuring Colour: The CIE Colour Appearance Model CIECAM02*, John Wiley & Sons, Ltd, **2011**.

[170] J. Kremers, R. C. Baraas, N. J. Marshall, Eds. , *Human Color Vision*, **2016**.

[171] T. Maurer, P.-M. Adam, G. Lévêque, *Nanophotonics* **2015**, *4*, 363.

[172] L. Novotny, B. Hecht, in *Principles of Nano-Optics: Theoretical Foundations*, Cambridge University Press, Cambridge, **2006**, pp. 12–44.

[173] G. A. Vinnacombe-Willson, N. Chiang, P. S. Weiss, S. H. Tolbert, L. Scarabelli, *J. Chem. Educ.* **2021**, *98*, 546.

[174] L. Mulfinger, S. D. Solomon, M. Bahadory, A. V. Jeyarajasingam, S. A. Rutkowsky, C. Boritz, *J. Chem. Educ.* **2007**, *84*, 322.

[175] N. E. Markina, M. V. Pozharov, A. V. Markin, *J. Chem. Educ.* **2016**, *93*, 704.

[176] C. Rossner, T. A. F. König, A. Fery, *Adv. Opt. Mater.* **2021**, *9*, 2001869.

[177] A. M. Weiner, *Rev. Sci. Instrum* **2000**, *71*, 1929.

[178] N. R. Jana, L. Gearheart, C. J. Murphy, *Langmuir* **2001**, *17*, 6782.

[179] Y. Zheng, X. Zhong, Z. Li, Y. Xia, *Part. Part. Syst. Charact.* **2014**, *31*, 266.

[180] M. L. Brongersma, N. J. Halas, P. Nordlander, *Nat. Nanotechnol.* **2015**, *10*, 25.

[181] R. Chikkaraddy, B. de Nijs, F. Benz, S. J. Barrow, O. A. Scherman, E. Rosta, A. Demetriadou, P. Fox, O. Hess, J. J. Baumberg, *Nature* **2016**, *535*, 127.

[182] A. Loiseau, L. Zhang, D. Hu, M. Salmain, Y. Mazouzi, R. Flack, B. Liedberg, S. Boujday, *ACS Appl. Mater. Interfaces* **2019**, *11*, 46462.

[183] A. A. Tabrizi, H. Saghaei, M. A. Mehranpour, M. Jahangiri, *Plasmonics* **2021**, *16*, 747.

[184] P. Qiao, L. Zhu, W. C. Chew, C. J. Chang-Hasnain, *Opt. Express, OE* **2015**, *23*, 24508.

[185] R. Jin, Y. Cao, C. A. Mirkin, K. L. Kelly, G. C. Schatz, J. G. Zheng, *Science* **2001**, *294*, 1901.

[186] M. R. Langille, J. Zhang, M. L. Personick, S. Li, C. A. Mirkin, *Science* **2012**, *337*, 954.

[187] L. M. Moreau, M. R. Jones, E. W. Roth, J. Wu, S. Kewalramani, M. N. O'Brien, B.-R. Chen, C. A. Mirkin, M. J. Bedzyk, *Nanoscale* **2019**, *11*, 11744.

[188] L. Huang, H. Lin, C. Y. Zheng, E. J. Kluender, R. Golnabi, B. Shen, C. A. Mirkin, *J. Am. Chem. Soc.* **2020**, *142*, 4570.

[189] W.-S. Chang, B. A. Willingham, L. S. Slaughter, B. P. Khanal, L. Vigderman, E. R. Zubarev, S. Link, *Proc. Natl. Acad. Sci.* **2011**, *108*, 19879.

[190] S. V. Boriskina, T. A. Cooper, L. Zeng, G. Ni, J. K. Tong, Y. Tsurimaki, Y. Huang, L. Meroueh, G. Mahan, G. Chen, *Adv. Opt. Photon., AOP* **2017**, *9*, 775.

[191] M. R. Jones, R. J. Macfarlane, B. Lee, J. Zhang, K. L. Young, A. J. Senesi, C. A. Mirkin, *Nat. Mater.* **2010**, *9*, 913.

[192] X. Liu, L. Fu, S. Hong, V. p. Dravid, C. a. Mirkin, *Adv. Mater.* **2002**, *14*, 231.

[193] D. Nepal, M. S. Onses, K. Park, M. Jespersen, C. J. Thode, P. F. Nealey, R. A. Vaia, *ACS Nano* **2012**, *6*, 5693.

[194] M. Mayer, P. L. Potapov, D. Pohl, A. M. Steiner, J. Schultz, B. Rellinghaus, A. Lubk, T. A. F. König, A. Fery, *Nano Lett.* **2019**, *19*, 3854.

[195] H. Zhang, Y. Liu, M. F. S. Shahidan, C. Kinnear, F. Maasoumi, J. Cadusch, E. M. Akinoglu, T. D. James, A. Widmer-Cooper, A. Roberts, P. Mulvaney, *Adv. Funct. Mater.* **2021**, *31*, 2006753.

[196] C. Matricardi, C. Hanske, J. L. Garcia-Pomar, J. Langer, A. Mihi, L. M. Liz-Marzán, *ACS Nano* **2018**, *12*, 8531.

[197] N. Pazos-Pérez, W. Ni, A. Schweikart, R. A. Alvarez-Puebla, A. Fery, L. M. Liz-Marzán, *Chem. Sci.* **2010**, *1*, 174.

[198] C. Hanske, E. H. Hill, D. Vila-Liarte, G. González-Rubio, C. Matricardi, A. Mihi, L. M. Liz-Marzán, *ACS Appl. Mater. Interfaces* **2019**, *11*, 11763.

[199] S. H. Ko, I. Park, H. Pan, C. P. Grigoropoulos, A. P. Pisano, C. K. Luscombe, J. M. J. Fréchet, *Nano Lett.* **2007**, *7*, 1869.

[200] C. Ng, J. J. Cadusch, S. Dligatch, A. Roberts, T. J. Davis, P. Mulvaney, D. E. Gómez, *ACS Nano* **2016**, *10*, 4704.

[201] Y. Gao, W. Nie, Q. Zhu, X. Wang, S. Wang, F. Fan, C. Li, *Angew. Chem. Int. Ed.* **2020**, *59*, 18218.

[202] M. M. Greve, B. Holst, *J. Vac. Sci. Technol. B* **2013**, *31*, 043202.

[203] H. Lan, *Soft UV Nanoimprint Lithography and Its Applications*, IntechOpen, **2013**.

[204] B. Kwon, J. H. Kim, *J. Nanosci. Nanotechnol.* **2016**, *2016*, e6571297.

[205] C. A. Schneider, W. S. Rasband, K. W. Eliceiri, *Nat. Methods* **2012**, *9*, 671.

[206] S. Sarkar, V. Gupta, T. Tsuda, J. Gour, A. Singh, O. Aftenieva, A. M. Steiner, M. Hoffmann, S. Kumar, A. Fery, J. Joseph, T. A. F. König, *Adv. Funct. Mater.* **2021**, *31*, 2011099.

[207] L. E. Kreilkamp, V. I. Belotelov, J. Y. Chin, S. Neutzner, D. Dregely, T. Wehlus, I. A. Akimov, M. Bayer, B. Stritzker, H. Giessen, *Phys. Rev. X* **2013**, *3*, 041019.

[208] N. Kooy, K. Mohamed, L. T. Pin, O. S. Guan, *Nanoscale Res. Lett.* **2014**, *9*, 320.

[209] S. Sarkar, K. Samanta, J. Joseph, *J. Opt.* **2020**, *22*, 085105.

[210] C. Lu, R. h. Lipson, *Laser Photonics Rev.* **2010**, *4*, 568.

[211] R. Mahmood, A. V. Ramirez, A. C. Hillier, *ACS Appl. Nano Mater.* **2021**, *4*, 8851.

[212] S. S. E. Collins, E. K. Searles, L. J. Tauzin, M. Lou, L. Bursi, Y. Liu, J. Song, C. Flatebo, R. Baiyasi, Y.-Y. Cai, B. Foerster, T. Lian, P. Nordlander, S. Link, C. F. Landes, *ACS Nano* **2021**, *15*, 9522.

[213] T. M. Brenner, D. A. Egger, L. Kronik, G. Hodes, D. Cahen, *Nat. Rev. Mater.* **2016**, *1*, 1.

[214] A. K. Jena, A. Kulkarni, T. Miyasaka, *Chem. Rev.* **2019**, *119*, 3036.

[215] S. A. Veldhuis, P. P. Boix, N. Yantara, M. Li, T. C. Sum, N. Mathews, S. G. Mhaisalkar, *Adv. Mater.* **2016**, *28*, 6804.

[216] M. V. Kovalenko, L. Protesescu, M. I. Bodnarchuk, *Science* **2017**, *358*, 745.

[217] S. D. Stranks, R. L. Z. Hoye, D. Di, R. H. Friend, F. Deschler, *Adv. Mater.* **2019**, *31*, 1803336.

[218] A. F. Gualdrón-Reyes, S. Masi, I. Mora-Seró, *Trends Analyt. Chem.* **2021**, *3*, 499.

[219] B. Conings, J. Drijkoningen, N. Gauquelin, A. Babayigit, J. D'Haen, L. D'Olieslaeger, A. Ethirajan, J. Verbeeck, J. Manca, E. Mosconi, F. D. Angelis, H.-G. Boyen, *Adv. Energy Mater* **2015**, *5*, 1500477.

[220] J. Liang, J. Liu, Z. Jin, *Solar RRL* **2017**, *1*, 1700086.

[221] M. Albaladejo-Siguan, E. C. Baird, D. Becker-Koch, Y. Li, A. L. Rogach, Y. Vaynzof, *Adv. Energy Mater* **2021**, *11*, 2003457.

[222] L. Protesescu, S. Yakunin, M. I. Bodnarchuk, F. Krieg, R. Caputo, C. H. Hendon, R. X. Yang, A. Walsh, M. V. Kovalenko, *Nano Lett.* **2015**, *15*, 3692.

[223] A. J. Ramadan, L. A. Rochford, S. Fearn, H. J. Snaith, *J. Phys. Chem. Lett.* **2017**, *8*, 4172.

[224] Q. A. Akkerman, V. D'Innocenzo, S. Accornero, A. Scarpellini, A. Petrozza, M. Prato, L. Manna, *J. Am. Chem. Soc.* **2015**, *137*, 10276.

[225] A. Swarnkar, A. R. Marshall, E. M. Sanehira, B. D. Chernomordik, D. T. Moore, J. A. Christians, T. Chakrabarti, J. M. Luther, *Science* **2016**, *354*, 92.

[226] Y. Wang, Y. Chen, T. Zhang, X. Wang, Y. Zhao, *Adv. Mater.* **2020**, *32*, 2001025.

[227] H.-C. Wang, Z. Bao, H.-Y. Tsai, A.-C. Tang, R.-S. Liu, *Small* **2018**, *14*, 1702433.

[228] G. Li, F. W. R. Rivarola, N. J. L. K. Davis, S. Bai, T. C. Jellicoe, F. de la Peña, S. Hou, C. Ducati, F. Gao, R. H. Friend, N. C. Greenham, Z.-K. Tan, *Adv. Mater.* **2016**, *28*, 3528.

[229] R. K. Raman, S. A. Gurusamy Thangavelu, S. Venkataraj, A. Krishnamoorthy, *Renew. Sustain. Energy Rev.* **2021**, *151*, 111608.

[230] T. D. Visser, H. Blok, B. Demeulenaere, D. Lenstra, *IEEE J. Quantum Electron.* **1997**, *33*, 1763.

[231] A. Vaskin, R. Kolkowski, A. F. Koenderink, I. Staude, *Nanophotonics* **2019**, *8*, 1151.

[232] A. A. Darweesh, S. J. Bauman, D. T. Debu, J. B. Herzog, *Nanomaterials* **2018**, *8*, 809.

[233] U. Fano, *J. Opt. Soc. Am., JOSA* **1941**, *31*, 213.

[234] M. Pelton, *Nat. Photon.* **2015**, *9*, 427.

[235] S. Hamdad, A. T. Diallo, M. Chakaroun, A. Boudrioua, *Sci Rep* **2022**, *12*, 3218.

[236] E. Mendoza-Sandoval, G. Rodríguez-López, C. L. Ordóñez-Romero, D. Ley, N. Qureshi, M. Urbánek, D. Solis-Ibarra, C. Noguez, H. A. Lara-García, G. Pirruccio, *J. Mater. Chem. C* **2022**, *10*, 3704.

[237] Y. Hua, Y. Wei, B. Chen, Z. Liu, Z. He, Z. Xing, S. Liu, P. Huang, Y. Chen, Y. Gao, J. Liu, *Micromachines* **2021**, *12*, 422.

[238] Y. Jia, R. A. Kerner, A. J. Grede, B. P. Rand, N. C. Giebink, *Nat. Photon.* **2017**, *11*, 784.

[239] Z.-T. Huang, C.-W. Yin, Y.-H. Hong, H. Li, K.-B. Hong, T. S. Kao, M.-H. Shih, T.-C. Lu, *Adv. Opt. Mater.* **2021**, *9*, 2100299.

[240] J. Guan, L. K. Sagar, R. Li, D. Wang, G. Bappi, N. E. Watkins, M. R. Bourgeois, L. Levina, F. Fan, S. Hoogland, O. Voznyy, J. Martins de Pina, R. D. Schaller, G. C. Schatz, E. H. Sargent, T. W. Odom, *Nano Lett.* **2020**, *20*, 1468.

[241] G. L. Whitworth, J. R. Harwell, D. N. Miller, G. J. Hedley, W. Zhang, H. J. Snaith, G. A. Turnbull, I. D. W. Samuel, *Opt. Express, OE* **2016**, *24*, 23677.

[242] S. Chen, K. Roh, J. Lee, W. K. Chong, Y. Lu, N. Mathews, T. C. Sum, A. Nurmikko, *ACS Nano* **2016**, *10*, 3959.

[243] Y. Jia, R. A. Kerner, A. J. Grede, A. N. Brigeman, B. P. Rand, N. C. Giebink, *Nano Lett.* **2016**, *16*, 4624.

[244] H. Cha, S. Bae, M. Lee, H. Jeon, *Appl. Phys. Lett.* **2016**, *108*, 181104.

[245] N. Pourdavoud, A. Mayer, M. Buchmüller, K. Brinkmann, T. Häger, T. Hu, R. Heiderhoff, I. Shutsko, P. Görrn, Y. Chen, H.-C. Scheer, T. Riedl, *Adv. Mater. Technol.* **2018**, *3*, 1700253.

[246] M. Saliba, S. M. Wood, J. B. Patel, P. K. Nayak, J. Huang, J. A. Alexander-Webber, B. Wenger, S. D. Stranks, M. T. Hörantner, J. T.-W. Wang, R. J. Nicholas, L. M. Herz, M. B. Johnston, S. M. Morris, H. J. Snaith, M. K. Riede, *Adv. Mater.* **2016**, *28*, 923.

[247] A. Gharajeh, R. Haroldson, Z. Li, J. Moon, B. Balachandran, W. Hu, A. Zakhidov, Q. Gu, *Opt. Lett., OL* **2018**, *43*, 611.

[248] N. Li, W. Lan, Y. S. Lau, L. Cai, A. A. Syed, F. Zhu, *J. Mater. Chem. C* **2019**, *7*, 9573.

[249] C. Zhang, W. Li, D. Yu, Y. Wang, M. Yin, H. Wang, Y. Song, X. Zhu, P. Chang, X. Chen, D. Li, *Adv. Mater. Interfaces* **2017**, *4*, 1601116.

[250] S. Haque, M. Alexandre, M. J. Mendes, H. Águas, E. Fortunato, R. Martins, *Appl. Mater. Today* **2020**, *20*, 100720.

[251] B. Jeong, H. Han, C. Park, *Adv. Mater.* **2020**, *32*, 2000597.

[252] J. Yang, B. D. Siempelkamp, D. Liu, T. L. Kelly, *ACS Nano* **2015**, *9*, 1955.

[253] N. Yi, S. Wang, Z. Duan, K. Wang, Q. Song, S. Xiao, *Adv. Mater.* **2017**, *29*, 1701636.

[254] A. A. Melvin, V. D. Stoichkov, J. Kettle, D. Mogilyansky, E. A. Katz, I. Visoly-Fisher, *Sol. Energy* **2018**, *159*, 794.

[255] D. K. Oh, T. Lee, B. Ko, T. Badloe, J. G. Ok, J. Rho, *Front. Optoelectron.* **2021**, *14*, 229.

[256] A. Mayer, M. Buchmüller, S. Wang, C. Steinberg, M. Papenheim, H.-C. Scheer, N. Pourdavoud, T. Haeger, T. Riedl, *J. Vac. Sci. Technol. B* **2017**, *35*, 06G803.

[257] J. Moon, S. Kwon, M. Alahbakhshi, Y. Lee, K. Cho, A. Zakhidov, M. J. Kim, Q. Gu, *ACS Appl. Mater. Interfaces* **2021**, *13*, 5368.

[258] E. Y. Tiguntseva, Z. Sadrieva, B. V. Stroganov, Yu. V. Kapitonov, F. Komissarenko, R. Haroldson, B. Balachandran, W. Hu, Q. Gu, A. A. Zakhidov, A. Bogdanov, S. V. Makarov, *Appl. Surf. Sci.* **2019**, *473*, 419.

[259] J. Zhang, Q. Guo, X. Li, C. Li, K. Wu, I. Abrahams, H. Yan, M. M. Knight, C. J. Humphreys, L. Su, *ACS Nano* **2020**, *14*, 11029.

[260] N. Pourdavoud, S. Wang, A. Mayer, T. Hu, Y. Chen, A. Marianovich, W. Kowalsky, R. Heiderhoff, H.-C. Scheer, T. Riedl, *Adv. Mater.* **2017**, *29*, 1605003.

[261] S. V. Makarov, V. Milichko, E. V. Ushakova, M. Omelyanovich, A. Cerdan Pasaran, R. Haroldson, B. Balachandran, H. Wang, W. Hu, Y. S. Kivshar, A. A. Zakhidov, *ACS Photonics* **2017**, *4*, 728.

[262] H. Wang, R. Haroldson, B. Balachandran, A. Zakhidov, S. Sohal, J. Y. Chan, A. Zakhidov, W. Hu, *ACS Nano* **2016**, *10*, 10921.

[263] R. Schmager, I. M. Hossain, F. Schackmar, B. S. Richards, G. Gomard, U. W. Paetzold, *Sol. Energy Mater Sol. Cells* **2019**, *201*, 110080.

[264] U. W. Paetzold, W. Qiu, F. Finger, J. Poortmans, D. Cheyns, *Appl. Phys. Lett.* **2015**, *106*, 173101.

[265] S. Nanz, R. Schmager, M. G. Abebe, C. Willig, A. Wickberg, A. Abass, G. Gomard, M. Wegener, U. W. Paetzold, C. Rockstuhl, *APL Photonics* **2019**, *4*, 076104.

[266] Q. Song, Y. Wang, F. Vogelbacher, Y. Zhan, D. Zhu, Y. Lan, W. Fang, Z. Zhang, L. Jiang, Y. Song, M. Li, *Adv. Energy Mater* **n.d.**, *n/a*, 2100742.

[267] J. Mao, W. E. I. Sha, H. Zhang, X. Ren, J. Zhuang, V. A. L. Roy, K. S. Wong, W. C. H. Choy, *Adv. Funct. Mater.* **2017**, *27*, 1606525.

[268] V. I. Korolev, A. P. Pushkarev, P. A. Obraztsov, A. N. Tsypkin, A. A. Zakhidov, S. V. Makarov, *Nanophotonics* **2020**, *9*, 187.

[269] Y. Wang, Y. Lan, Q. Song, F. Vogelbacher, T. Xu, Y. Zhan, M. Li, W. E. I. Sha, Y. Song, *Advanced Materials* **2021**, *33*, 2008091.

[270] D. H. Chun, Y. J. Choi, Y. In, J. K. Nam, Y. J. Choi, S. Yun, W. Kim, D. Choi, D. Kim, H. Shin, J. H. Cho, J. H. Park, *ACS Nano* **2018**, *12*, 8564.

[271] Z. Li, J. Moon, A. Gharajeh, R. Haroldson, R. Hawkins, W. Hu, A. Zakhidov, Q. Gu, *ACS Nano* **2018**, *12*, 10968.

[272] C. Huang, C. Zhang, S. Xiao, Y. Wang, Y. Fan, Y. Liu, N. Zhang, G. Qu, H. Ji, J. Han, L. Ge, Y. Kivshar, Q. Song, *Science* **2020**, *367*, 1018.

[273] S. Brittman, S. Z. Oener, K. Guo, H. Āboliņš, A. F. Koenderink, E. C. Garnett, *J. Mater. Chem. C* **2017**, *5*, 8301.

[274] S. Guo, Y.-S. Liu, X.-L. Zhang, Y.-F. Liu, Y.-G. Bi, X.-M. Wen, J. Feng, H.-B. Sun, *Opt Lett* **2020**, *45*, 5156.

[275] D. Vila-Liarte, M. W. Feil, A. Manzi, J. L. Garcia-Pomar, H. Huang, M. Döblinger, L. M. Liz-Marzán, J. Feldmann, L. Polavarapu, A. Mihi, *Angew. Chem. Int. Ed.* **2020**, *59*, 17750.

[276] J. W. Strutt, *Proceedings of the Royal Society of London. Series A, Containing Papers of a Mathematical and Physical Character* **1907**, *79*, 399.

[277] Lord Rayleigh, *The London, Edinburgh, and Dublin Philosophical Magazine and Journal of Science* **1907**, *14*, 60.

[278] M. Wang, A. Löhle, B. Gompf, M. Dressel, A. Berrier, *Opt. Express, OE* **2017**, *25*, 6983.

[279] V. Gupta, S. Sarkar, O. Aftenieva, T. Tsuda, L. Kumar, D. Schletz, J. Schultz, A. Kiriy, A. Fery, N. Vogel, T. A. F. König, *Adv. Funct. Mater.* **2021**, *31*, 2105054.

[280] O. Aftenieva, M. Schnepf, B. Mehlhorn, T. A. F. König, *Adv. Opt. Mater.* **2021**, *9*, 2001280.

[281] T. Honda, M. Miyazaki, H. Nakamura, H. Maeda, *Lab Chip* **2005**, *5*, 812.

[282] J. E. Harvey, R. N. Pfisterer, *OE* **2019**, *58*, 087105.

[283] M. "Mike" Kim, Y. Huang, K. Choi, C. H. Hidrovo, *Microelectron. Eng.* **2014**, *124*, 66.

[284] PubChem, PubChem, https://pubchem.ncbi.nlm.nih.gov/, accessed: Jun., 2022.

[285] S. Makarov, A. Furasova, E. Tiguntseva, A. Hemmetter, A. Berestennikov, A. Pushkarev, A. Zakhidov, Y. Kivshar, *Adv. Opt. Mater.* **2019**, *7*, 1800784.

[286] V. Navarro-Fuster, P. G. Boj, J. M. Villalvilla, J. A. Quintana, M. A. Díaz-García, V. Trabadelo, A. Juarros, A. Retolaza, S. Merino, in *Organic Photonics IV*, SPIE, **2010**, pp. 174–182.

[287] D. Marcuse, in *Theory of Dielectric Optical Waveguides (Second Edition): Chapter 3 - COUPLED MODE THEORY* (Ed.: D. Marcuse), Academic Press, **1991**.

[288] A. Mitrofanov, A. Prudnikau, F. Di Stasio, N. Weiß, R. Hübner, A. M. Dominic, K. B. L. Borchert, V. Lesnyak, A. Eychmüller, *Chem. Mater.* **2021**, *33*, 7693.

[289] M. Leng, Z. Chen, Y. Yang, Z. Li, K. Zeng, K. Li, G. Niu, Y. He, Q. Zhou, J. Tang, *Angew. Chem. Int. Ed.* **2016**, *55*, 15012.

[290] D. Becker-Koch, M. Albaladejo-Siguan, J. Kress, R. Kumar, Y. J. Hofstetter, Q. An, A. A. Bakulin, F. Paulus, Y. Vaynzof, *Nanoscale* **2022**, *14*, 3020.

[291] One-Dimensional Roughness Parameters, http://gwyddion.net/documentation/user-guide-en/roughness-iso.html, accessed: Jun., 2022.

[292] Nanophotonic FDTD Simulation Software - Lumerical FDTD, https://www.lumerical.com/products/fdtd/, accessed: Jun., 2022.

[293] X. Zhuang, Y. Ouyang, X. Wang, A. Pan, *Adv. Opt. Mater.* **2019**, *7*, 1900071.

[294] S. Hepp, M. Jetter, S. L. Portalupi, P. Michler, *Adv. Quantum Technol.* **2019**, *2*, 1900020.

[295] C. Wang, B. Wang, K. H. Lee, C. S. Tan, S. F. Yoon, J. Michel, *Opt. Express, OE* **2016**, *24*, 23129.

[296] P. Geiregat, D. Van Thourhout, Z. Hens, *NPG Asia Mater* **2019**, *11*, 1.

[297] J. Chen, K. Rong, *Mater. Chem. Front.* **2021**, *5*, 4502.

[298] L. Qu, X. Peng, *J. Am. Chem. Soc.* **2002**, *124*, 2049.

[299] C. de M. Donegá, *Chem. Soc. Rev.* **2011**, *40*, 1512.

[300] S. Wei, Y. Liu, M. Ma, Y. Wu, L. Huang, D. Pan, *J. Mater. Chem. C* **2018**, *6*, 11104.

[301] F. Di Stasio, J. Q. Grim, V. Lesnyak, P. Rastogi, L. Manna, I. Moreels, R. Krahne, *Small* **2015**, *11*, 1328.

[302] X. Wang, J. Yu, R. Chen, *Sci Rep* **2018**, *8*, 17323.

[303] M. Li, M. Zhi, H. Zhu, W.-Y. Wu, Q.-H. Xu, M. H. Jhon, Y. Chan, *Nat Commun* **2015**, *6*, 8513.

[304] C. Dang, J. Lee, C. Breen, J. S. Steckel, S. Coe-Sullivan, A. Nurmikko, *Nat. Nanotechnol.* **2012**, *7*, 335.

[305] R. K. Patel, A. A. P. Trichet, D. M. Coles, P. R. Dolan, S. M. Fairclough, M. A. Leontiadou, S. C. E. Tsang, D. J. Binks, E. Jang, H. Jang, R. A. Taylor, J. M. Smith, *Adv. Opt. Mater.* **2016**, *4*, 285.

[306] B. le Feber, F. Prins, E. De Leo, F. T. Rabouw, D. J. Norris, *Nano Lett.* **2018**, *18*, 1028.

[307] K. Rong, H. Liu, K. Shi, J. Chen, *Nanoscale* **2019**, *11*, 13885.

[308] M. Zavelani-Rossi, M. G. Lupo, R. Krahne, L. Manna, G. Lanzani, *Nanoscale* **2010**, *2*, 931.

[309] C. Liao, R. Xu, Y. Xu, C. Zhang, M. Xiao, L. Zhang, C. Lu, Y. Cui, J. Zhang, *J. Phys. Chem. Lett.* **2016**, *7*, 4968.

[310] W. Xie, T. Stöferle, G. Rainò, T. Aubert, S. Bisschop, Y. Zhu, R. F. Mahrt, P. Geiregat, E. Brainis, Z. Hens, D. Van Thourhout, *Adv. Mater.* **2017**, *29*, 1604866.

[311] K. Rong, F. Gan, K. Shi, S. Chu, J. Chen, *Adv. Mater.* **2018**, *30*, 1706546.

[312] C. H. Lin, Q. Zeng, E. Lafalce, M. J. Smith, S. T. Malak, J. Jung, Y. J. Yoon, Z. Lin, Z. V. Vardeny, V. V. Tsukruk, *Adv. Opt. Mater.* **2017**, *5*, 1700011.

[313] F. Montanarella, D. Urbonas, L. Chadwick, P. G. Moerman, P. J. Baesjou, R. F. Mahrt, A. van Blaaderen, T. Stöferle, D. Vanmaekelbergh, *ACS Nano* **2018**, *12*, 12788.

[314] P. T. Snee, Y. Chan, D. G. Nocera, M. G. Bawendi, *Adv. Mater.* **2005**, *17*, 1131.

[315] C. Grivas, C. Li, P. Andreakou, P. Wang, M. Ding, G. Brambilla, L. Manna, P. Lagoudakis, *Nat Commun* **2013**, *4*, 2376.

[316] Y. Wang, V. D. Ta, K. S. Leck, B. H. I. Tan, Z. Wang, T. He, C.-D. Ohl, H. V. Demir, H. Sun, *Nano Lett.* **2017**, *17*, 2640.

[317] N. Taghipour, S. Delikanli, S. Shendre, M. Sak, M. Li, F. Isik, I. Tanriover, B. Guzelturk, T. C. Sum, H. V. Demir, *Nat Commun* **2020**, *11*, 3305.

[318] G. Shan, X. Zhao, M. Hu, C.-H. Shek, W. Huang, *Front. Optoelectron.* **2012**, *5*, 157.

[319] Y. Wang, S. Chen, Y. Yu, L. Zhou, L. Liu, C. Yang, M. Liao, M. Tang, Z. Liu, J. Wu, W. Li, I. Ross, A. J. Seeds, H. Liu, S. Yu, *Optica, OPTICA* **2018**, *5*, 528.

[320] H. Jung, M. Lee, C. Han, Y. Park, K.-S. Cho, H. Jeon, *Opt. Express, OE* **2017**, *25*, 32919.

[321] P.-J. Cheng, Z.-T. Huang, J.-H. Li, B.-T. Chou, Y.-H. Chou, W.-C. Lo, K.-P. Chen, T.-C. Lu, T.-R. Lin, *ACS Photonics* **2018**, *5*, 2638.

[322] C.-Z. Ning, *AP* **2019**, *1*, 014002.

[323] J. Guan, L. K. Sagar, R. Li, D. Wang, G. Bappi, W. Wang, N. Watkins, M. R. Bourgeois, L. Levina, F. Fan, S. Hoogland, O. Voznyy, J. M. de Pina, R. D. Schaller, G. C. Schatz, E. H. Sargent, T. W. Odom, *ACS Nano* **2020**, *14*, 3426.

[324] D. Mampallil, H. B. Eral, *Adv. Colloid Interface Sci.* **2018**, *252*, 38.

[325] S. Chénais, S. Forget, *Polym. Int.* **2012**, *61*, 390.

[326] S. Basak, O. Bar-On, O. Bar-On, J. Scheuer, J. Scheuer, J. Scheuer, *Opt. Mater. Express, OME* **2022**, *12*, 375.

[327] S. Riechel, C. Kallinger, U. Lemmer, J. Feldmann, A. Gombert, V. Wittwer, U. Scherf, *Appl. Phys. Lett.* **2000**, *77*, 2310.

[328] A. E. Vasdekis, G. A. Turnbull, I. D. W. Samuel, P. Andrew, W. L. Barnes, *Appl. Phys. Lett.* **2005**, *86*, 161102.

[329] P. Zhou, L. Niu, A. Hayat, F. Cao, T. Zhai, X. Zhang, *Polymers* **2019**, *11*, 258.

[330] D. Schneider, S. Hartmann, T. Dobbertin, T. Benstem, D. Metzdorf, E. Becker, A. Kammoun, C. Schildknecht, H. Krautwald, H.-H. Johannes, T. Riedl, W. Kowalsky, in *Organic Light-Emitting Materials and Devices VII*, International Society For Optics And Photonics, **2004**, pp. 310–317.

[331] F. Fan, O. Voznyy, R. P. Sabatini, K. T. Bicanic, M. M. Adachi, J. R. McBride, K. R. Reid, Y.-S. Park, X. Li, A. Jain, R. Quintero-Bermudez, M. Saravanapavanantham, M. Liu, M. Korkusinski, P. Hawrylak, V. I. Klimov, S. J. Rosenthal, S. Hoogland, E. H. Sargent, *Nature* **2017**, *544*, 75.

[332] M. M. Adachi, F. Fan, D. P. Sellan, S. Hoogland, O. Voznyy, A. J. Houtepen, K. D. Parrish, P. Kanjanaboos, J. A. Malen, E. H. Sargent, *Nat Commun* **2015**, *6*, 8694.

[333] Y. Zhu, W. Xie, S. Bisschop, T. Aubert, E. Brainis, P. Geiregat, Z. Hens, D. Van Thourhout, *ACS Photonics* **2017**, *4*, 2446.

[334] O. V. Kozlov, Y.-S. Park, J. Roh, I. Fedin, T. Nakotte, V. I. Klimov, *Science* **2019**, *365*, 672.

[335] C. Han, H. Jung, J. Lee, M. Lee, Y. Park, K.-S. Cho, H. Jeon, *Adv. Mater. Technol.* **2018**, *3*, 1700291.

[336] H. Kim, K. Roh, J. P. Murphy, L. Zhao, W. B. Gunnarsson, E. Longhi, S. Barlow, S. R. Marder, B. P. Rand, N. C. Giebink, *Adv. Opt. Mater.* **2020**, *8*, 1901297.

[337] S. Zhang, L.-B. Cui, X. Zhang, J.-H. Tong, T. Zhai, *Opt. Express, OE* **2020**, *28*, 2809.

[338] H. Jung, C. Han, H. Kim, K.-S. Cho, Y.-G. Roh, Y. Park, H. Jeon, *Nanoscale* **2018**, *10*, 22745.

[339] F. Todescato, I. Fortunati, S. Gardin, E. Garbin, E. Collini, R. Bozio, J. J. Jasieniak, G. Della Giustina, G. Brusatin, S. Toffanin, R. Signorini, *Adv. Funct. Mater.* **2012**, *22*, 337.

[340] B. Guilhabert, C. Foucher, A.-M. Haughey, E. Mutlugun, Y. Gao, J. Herrnsdorf, H. D. Sun, H. V. Demir, M. D. Dawson, N. Laurand, *Opt. Express, OE* **2014**, *22*, 7308.

[341] R. Signorini, I. Fortunati, F. Todescato, S. Gardin, R. Bozio, J. J. Jasieniak, A. Martucci, G. D. Giustina, G. Brusatin, M. Guglielmi, *Nanoscale* **2011**, *3*, 4109.

[342] Y. Gao, L. Y. M. Tobing, A. Kiffer, D. H. Zhang, C. Dang, H. V. Demir, *ACS Photonics* **2016**, *3*, 2255.

[343] T. Zhai, L. Han, X. Ma, X. Wang, *Nanomaterials* **2021**, *11*, 1530.

[344] N. Gheshlaghi, S. Foroutan-Barenji, O. Erdem, Y. Altintas, F. Shabani, M. H. Humayun, H. V. Demir, *Nano Lett.* **2021**, *21*, 4598.

[345] T. S. Mentzel, D. D. Wanger, N. Ray, B. J. Walker, D. Strasfeld, M. G. Bawendi, M. A. Kastner, *Nano Lett.* **2012**, *12*, 4404.

[346] Y. Wang, J.-A. Pan, H. Wu, D. V. Talapin, *ACS Nano* **2019**, *13*, 13917.

[347] K. Miszta, F. Greullet, S. Marras, M. Prato, A. Toma, M. Arciniegas, L. Manna, R. Krahne, *Nano Lett.* **2014**, *14*, 2116.

[348] L. Zhang, C. Liao, B. Lv, X. Wang, M. Xiao, R. Xu, Y. Yuan, C. Lu, Y. Cui, J. Zhang, *ACS Appl. Mater. Interfaces* **2017**, *9*, 13293.

[349] S. Myeong, B. Chon, S. Kumar, H.-J. Son, S. O. Kang, S. Seo, *Nanoscale Adv.* **2022**, *4*, 1080.

[350] M. J. Smith, C. H. Lin, S. Yu, V. V. Tsukruk, *Adv. Opt. Mater.* **2019**, *7*, 1801072.

[351] C. Pina-Hernandez, A. Koshelev, S. Dhuey, S. Sassolini, M. Sainato, S. Cabrini, K. Munechika, *Sci Rep* **2017**, *7*, 17645.

[352] S. Klinkhammer, X. Liu, K. Huska, Y. Shen, S. Vanderheiden, S. Valouch, C. Vannahme, S. Bräse, T. Mappes, U. Lemmer, *Opt. Express, OE* **2012**, *20*, 6357.

[353] V. Navarro-Fuster, I. Vragovic, E. M. Calzado, P. G. Boj, J. A. Quintana, J. M. Villalvilla, A. Retolaza, A. Juarros, D. Otaduy, S. Merino, M. A. Díaz-García, *J. Appl. Phys.* **2012**, *112*, 043104.

[354] Y. Justo, I. Moreels, K. Lambert, Z. Hens, *Nanotechnology* **2010**, *21*, 295606.

[355] C. Wang, M. Shim, P. Guyot-Sionnest, *Appl. Phys. Lett.* **2002**, *80*, 4.

[356] Y. Yang, Y. Zheng, W. Cao, A. Titov, J. Hyvonen, J. R. Manders, J. Xue, P. H. Holloway, L. Qian, *Nat. Photon.* **2015**, *9*, 259.

[357] T. C. Nguyen, T. T. T. Can, W.-S. Choi, *Sci Rep* **2019**, *9*, 13885.

[358] C. Z. Ning, *IEEE J. Sel. Top. Quantum Electron.* **2013**, *19*, 1503604.

[359] Y. Shimizu, *Nanomanuf Metrol* **2021**, *4*, 3.

[360] I. Amidror, *The Theory of the Moiré Phenomenon*, Springer, London, **2009**.

[361] S. Kishimoto, M. Egashira, N. Shinya, *Opt.Eng.* **1993**, *32*, 522.

[362] J. K. Drinkwater, B. W. Holmes, K. A. Jones, *Proc. SPIE* **2000**, *3973*, 66.

[363] Z. Wu, G. Kelp, M. N. Yogeesh, W. Li, K. M. McNicholas, A. Briggs, B. B. Rajeeva, D. Akinwande, S. R. Bank, G. Shvets, Y. Zheng, *Nanoscale* **2016**, *8*, 18461.

[364] S. Balci, A. Kocabas, C. Kocabas, A. Aydinli, *Appl. Phys. Lett.* **2011**, *98*, 031101.

[365] S. M. Lubin, W. Zhou, A. J. Hryn, M. D. Huntington, T. W. Odom, *Nano Lett.* **2012**, *12*, 4948.

[366] C. Jin, B. C. Olsen, E. J. Luber, J. M. Buriak, *ACS Nano* **2017**, *11*, 3237.

[367] K. Chen, B. B. Rajeeva, Z. Wu, M. Rukavina, T. D. Dao, S. Ishii, M. Aono, T. Nagao, Y. Zheng, *ACS Nano* **2015**, *9*, 6031.

[368] L. A. Ibbotson, A. Demetriadou, S. Croxall, O. Hess, J. J. Baumberg, *Sci. Rep.* **2015**, *5*, 8313.

[369] V. Lesnyak, N. Gaponik, A. Eychmüller, *Chem. Soc. Rev.* **2013**, *42*, 2905.

[370] X. Gao, B. Han, X. Yang, Z. Tang, *J. Am. Chem. Soc.* **2019**, *141*, 13700.

[371] Z. Wang, Y. Wang, G. Adamo, J. Teng, H. Sun, *Laser Photonics Rev.* **2019**, *13*, 1800276.

[372] S. P. Rodrigues, Y. Cui, S. Lan, L. Kang, W. Cai, *Adv. Mater.* **2015**, *27*, 1124.

[373] M. Noh, T. Kim, H. Lee, C.-K. Kim, S.-W. Joo, K. Lee, *Colloids Surf. A Physicochem. Eng. Asp.* **2010**, *359*, 39.

[374] A. Raevskaya, V. Lesnyak, D. Haubold, V. Dzhagan, O. Stroyuk, N. Gaponik, D. R. T. Zahn, A. Eychmüller, *J. Phys. Chem. C* **2017**, *121*, 9032.

[375] V. Reboud, P. Lovera, N. Kehagias, M. Zelsmann, C. Schuster, F. Reuther, G. Gruetzner, G. Redmond, C. M. Sotomayor Torres, *Appl. Phys. Lett.* **2007**, *91*, 151101.

[376] M. Tagliazucchi, V. A. Amin, S. T. Schneebeli, J. F. Stoddart, E. A. Weiss, *Adv. Mater.* **2012**, *24*, 3617.

[377] S. T. Malak, G. Liang, R. Thevamaran, Y. J. Yoon, M. J. Smith, J. Jung, C. H. Lin, Z. Lin, E. L. Thomas, V. V. Tsukruk, *J. Phys. Chem. C* **2017**, *121*, 13370.

[378] J. Yang, M. K. Choi, D.-H. Kim, T. Hyeon, *Adv. Mater.* **2016**, *28*, 1176.

[379] Z. Dai, Q. Ou, C. Wang, G. Si, B. Shabbir, C. Zheng, Z. Wang, Y. Zhang, Y. Huang, Y. Dong, J. J. Jasieniak, B. Su, Q. Bao, *J. Mater. Chem. C* **2019**, *7*, 5954.

[380] B. Jeong, H. Han, H. H. Kim, W. K. Choi, Y. J. Park, C. Park, *ACS Nano* **2020**, *14*, 1645.

[381] L. Kim, P. O. Anikeeva, S. A. Coe-Sullivan, J. S. Steckel, M. G. Bawendi, V. Bulović, *Nano Lett.* **2008**, *8*, 4513.

[382] O. Stroyuk, A. Raevskaya, F. Spranger, O. Selyshchev, V. Dzhagan, S. Schulze, D. R. T. Zahn, A. Eychmüller, *J. Phys. Chem. C* **2018**, *122*, 13648.

[383] H. H. Kim, J. W. Shim, Y.-J. You, Y. J. Lee, C. Park, D. K. Hwang, W. K. Choi, *J. Mater. Chem. C* **2017**, *5*, 1596.

[384] Y. Liu, F. Han, F. Li, Y. Zhao, M. Chen, Z. Xu, X. Zheng, H. Hu, J. Yao, T. Guo, W. Lin, Y. Zheng, B. You, P. Liu, Y. Li, L. Qian, *Nat. Commun.* **2019**, *10*, 1.

[385] J. Jelken, S. Santer, *RSC Adv.* **2019**, *9*, 20295.

[386] G. Scordo, V. Bertana, L. Scaltrito, S. Ferrero, M. Cocuzza, S. L. Marasso, S. Romano, R. Sesana, F. Catania, C. F. Pirri, *Mater. Today Commun.* **2019**, *19*, 12.

[387] M. Mayer, M. J. Schnepf, T. A. F. König, A. Fery, *Adv. Opt. Mater.* **2019**, *7*, 1800564.

[388] F. R. Goßler, A. M. Steiner, O. Stroyuk, A. Raevskaya, T. A. F. König, *J. Phys. Chem. C* **2019**, *123*, 6745.

[389] S. C. Thickett, G. H. Teo, *Polym. Chem.* **2019**, *10*, 2906.

[390] M. A. Boles, M. Engel, D. V. Talapin, *Chem. Rev.* **2016**, *116*, 11220.

[391] A. I. Rogach, D. v. Talapin, E. v. Shevchenko, A. Kornowski, M. Haase, H. Weller, *Adv. Funct. Mater.* **2002**, *12*, 653.

[392] A. I. Väkeväinen, R. J. Moerland, H. T. Rekola, A.-P. Eskelinen, J.-P. Martikainen, D.-H. Kim, P. Törmä, *Nano Lett.* **2014**, *14*, 1721.

[393] X. Xiong, J.-B. You, P. Bai, C. E. Png, Z.-K. Zhou, L. Wu, *Nanophotonics* **2020**, *9*, 257.

[394] J. Liu, H. He, D. Xiao, S. Yin, W. Ji, S. Jiang, D. Luo, B. Wang, Y. Liu, *Materials* **2018**, *11*, 1833.

[395] Q. Zhang, W. Tao, J. Huang, R. Xia, J. Cabanillas-Gonzalez, *Adv. Photonics Res.* **2021**, *2*, 2000155.

[396] Y. Choi, C. Hahn, J. W. Yoon, S. H. Song, *Nat Commun* **2018**, *9*, 2182.

[397] S. Prahl, scottprahl/miepython: Mie scattering of light off perfect spheres in python, https://github.com/scottprahl/miepython, accessed: Feb., 2021.

[398] W. Wiscombe, *NCAR Technical Notes* **1979**, *TN-140+STR*, 1.

[399] C. R. Harris, K. J. Millman, S. J. van der Walt, R. Gommers, P. Virtanen, D. Cournapeau, E. Wieser, J. Taylor, S. Berg, N. J. Smith, R. Kern, M. Picus, S. Hoyer, M. H. van Kerkwijk, M. Brett, A. Haldane, J. F. del Río, M. Wiebe, P. Peterson, P. Gérard-Marchant, K. Sheppard, T. Reddy, W. Weckesser, H. Abbasi, C. Gohlke, T. E. Oliphant, *Nature* **2020**, *585*, 357.

[400] J. D. Hunter, *Comput Sci Eng* **2007**, *9*, 90.

[401] T. Wriedt, in *The Mie Theory: Basics and Applications* (Eds.: W. Hergert, T. Wriedt), Springer-Verlag, Berlin, **2012**, pp. 53–71.

[402] A. D. Broadbent, *Color Res Appl* **2004**, *29*, 267.

[403] Chromaticity: Ocean Optics Web Book, https://www.oceanopticsbook.info/view/photometry-and-visibility/chromaticity, accessed: Feb., 2021.

[404] J. R. Lakowicz, *Principles of Fluorescence Spectroscopy*, Springer New York, NY, **2006**.

[405] W. Yan, Y. Guo, D. Beri, S. Dottermusch, H. Chen, B. S. Richards, *Phys Status Solidi Rapid Res Lett* **2020**, *14*, 2000070.

[406] Non-Linear Least-Squares Minimization and Curve-Fitting for Python — Non-Linear Least-Squares Minimization and Curve-Fitting for Python, https://lmfit.github.io/lmfit-py/, accessed: Jun., 2022.

[407] S. Hou, A. Xie, Z. Xie, L. Y. M. Tobing, J. Zhou, L. Tjahjana, J. Yu, C. Hettiarachchi, D. Zhang, C. Dang, E. H. T. Teo, M. D. Birowosuto, H. Wang, *ACS Photonics* **2019**, *6*, 1331.

[408] X. Zhou, M. Li, K. Wang, H. Li, Y. Li, C. Li, Y. Yan, Y. Zhao, Y. Song, *Chemphyschem* **2018**, *19*, 2101.

[409] G. Adamo, H. N. Swaha Krishnamoorthy, D. Cortecchia, B. Chaudhary, V. Nalla, N. I. Zheludev, C. Soci, *Nano Lett.* **2020**, *20*, 7906.

[410] H. Wang, S.-C. Liu, B. Balachandran, J. Moon, R. Haroldson, Z. Li, A. Ishteev, Q. Gu, W. Zhou, A. Zakhidov, W. Hu, *Opt. Express, OE* **2017**, *25*, A1162.

[411] W. Chen, J. Sha, K. Yan, J. Luo, R. Xu, D. Yao, X. Liu, S. Liao, J. Zhong, S. Yang, Y. Yu, Y. Tong, Z. Xu, Y.-S. Lin, T.-S. Kao, in *2018 International Conference on Optical MEMS and Nanophotonics (OMN)*, **2018**, pp. 1–5.

[412] S. Park, J. Cho, D. Jeong, J. Jo, M. Nam, H. Rhee, J. S. Han, Y. J. Cho, B.-K. Ju, D.-H. Ko, H. S. Jang, *Chem. Eng. J.* **2020**, *393*, 124767.

[413] R. Fang, Y.-S. Lin, *AIP Advances* **2020**, *10*, 065328.

[414] J. Tian, G. Adamo, H. Liu, M. Klein, S. Han, H. Liu, C. Soci, *Adv. Mater.* **2022**, *34*, 2109157.

[415] A. S. Berestennikov, A. Vakulenko, S. Kiriushechkina, M. Li, Y. Li, L. E. Zelenkov, A. P. Pushkarev, M. A. Gorlach, A. L. Rogach, S. V. Makarov, A. B. Khanikaev, *J. Phys. Chem. C* **2021**, *125*, 9884.

[416] B. Gholipour, G. Adamo, D. Cortecchia, H. N. S. Krishnamoorthy, Muhammad. D. Birowosuto, N. I. Zheludev, C. Soci, *Adv. Mater.* **2017**, *29*, 1604268.

[417] C. F. Fong, Y. Yin, Y. Chen, D. Rosser, J. Xing, A. Majumdar, Q. Xiong, *Opt. Express, OE* **2019**, *27*, 18673.

[418] E. Tiguntseva, A. Chebykin, A. Ishteev, R. Haroldson, B. Balachandran, E. Ushakova, F. Komissarenko, H. Wang, V. Milichko, A. Tsypkin, D. Zuev, W. Hu, S. Makarov, A. Zakhidov, *Nanoscale* **2017**, *9*, 12486.

[419] K. Baryshnikova, D. Gets, T. Liashenko, A. Pushkarev, I. Mukhin, Y. Kivshar, S. Makarov, *Laser Photonics Rev.* **2020**, *14*, 2000338.

[420] Peak fitting XRD data with Python - Chris Ostrouchov, https://chrisostrouchov.com/post/peak_fit_xrd_python/, accessed: Jun., 2022.

[421] J. Roh, Y.-S. Park, J. Lim, V. I. Klimov, *Nature Communications* **2020**, *11*, 271.

[422] L. J. McLellan, B. Guilhabert, N. Laurand, M. D. Dawson, *Opt. Express, OE* **2016**, *24*, A146.

[423] V. M. Lavchiev, A. Saeed, D. Pogany, W. Jantsch, *IOP Conf. Ser.: Mater. Sci. Eng.* **2009**, *6*, 012028.

[424] M. I. Khan, Z. Khalid, F. A. Tahir, *Sci. Rep.* **2019**, *9*, 4552.

Erklärung & Versicherung

Hiermit versichere ich, dass ich die vorliegende Arbeit ohne unzulässige Hilfe Dritter und ohne Benutzung anderer als der angegebenen Hilfsmittel angefertigt habe; die aus fremden Quellen direkt oder indirekt übernommenen Gedanken sind als solche kenntlich gemacht. Die Arbeit wurde bisher weder im Inland noch im Ausland in gleicher oder ähnlicher Form einer anderen Prüfungsbehörde vorgelegt. Die vorliegende Arbeit wurde von November 2018 bis Juni 2022 am Leibniz-Institut für Polymerforschung Dresden e.V. unter der Betreuung von PD Dr. Tobias AF König (TUD Young Investigator Status) durchgeführt.

Datum, Unterschrift